VRIJE UNIVERSITEIT BRUSSEL

ULB

Localized structures in surface-emitting lasers: vectorial character and delay-induced motion

A thesis submitted in fulfilment of the requirements for the award of the degrees of Doctor in Science and Doctor in Engineering by

Etienne Averlant

Promoters: Mustapha Tlidi
Krassimir Panajotov

Jury: Johan Stiens (president)
Roger Vounckx (vice president)
Wendy Meulebroeck (secretary)
Giovanna Tissoni
Marcel Clerc
Pascal Kockaert
Serge Massar

ACKNOWLEDGMENTS

Acknowledgments often seems to be the easiest part of the thesis to write. Et en fait il y a des aspects assez agréables dans le genre schrijven in veel talen om te montrer qu'on est vraiment à Brüssels. But one needs to have a defined structure, and how to choose? Let's try with some kind of chronological one: the people that deserve the first round of acknowledgments must then be the parents! La science (et la physique a fortiori), c'est d'abord de la curiosité, et mes parents m'ont bien aidé à pousser ce trait (que certains peuvent trouver assez embêtant parfois) qu'ils avaient eux-même mis dans mon génome. Big up donc pour Éric et Monique. Xavier, Claire et Alexis (rejoints plus tard par Élisabeth, Emmanuel et Marie) ont aussi permis à ce bonhomme un peu bizarre d'assumer sa bizarrerie.

En vrai ça prend pas mal de temps d'écrire ce truc, comme on repense à la construction de soi, et du rôle des gens dans cette construction. If we[1] keep on going in that direction, it might become a huge section. So let's now include the people that constructed me as a human (thank god I'm not only a baby scientist) ; I'm thinking of... well... mostly people I've met rather recently. Life begins after secondary school, right? Among the Baggio people, the honour seat goes to MaxiProut, even though this PSI* class showed its *class* when times were hard for me. Sur une idée de Maxiprout d'ailleurs. Big up.

Après je suis arrivé à Orsay, où j'ai entre autres rencontré Marius, qui m'a appris la différence entre un basque et un catalan. Ou plutôt qu'il y avait une différence. Toujours avec le magistère, il y avait l'Erasmus à Berlin, et là, il y a du monde à mentionner ! L'adorable Julie, l'incroyable organisatrice Chtéfny (qui est à mon avis souvent à plusieurs endroits en même temps), la grande écrivaine Constance, et bien évidemment Mimidouce. Je ne vais pas vraiment épiloguer sur Mimidouce, les gens qui me connaissent savent bien à quel point ma construction en tant qu'humain a dépendu d'Elle. Mais ça me fait un pont d'or vers les historiens et autres amis d'Orianne qui m'ont accueilli au sein d'un groupe d'amis proches. Même si ces derniers ne sont pas trop branchés soirées pyjamas (smiley clin d'oeil). Pour finir cette partie sur la construction en tant qu'humain, il convient d'ajouter le crew de la VUB, le crew ULB (Lionel, Gaëtan, Sanne, Mateusz, Jens, Carlos, Yassin...[2]).

[1] `https://www.youtube.com/watch?v=E09LU6XVyxs`

[2] and many others I'm *actually* ashamed not to mention, even though the lack of room kind of explains this kind of omission

Let's put a step between the human-being and the scientist parts for those who helped big time for everything that has to do with university business, but not with science. This is the place where the honour seats are occupied by Majorie, Fabienne, Marie-France, Bernadette, Delphine... Again, some names are missing (the faculty administration at ULB by example-too many names). The teaching staff/students has also been quite enjoyable to work with :).

Then comes the scientific part ; first of all, my gratefulness goes to the jury members that spent a lot of their time to dig into this work. But the heart of this section has to be devoted to Krassimir and Mustapha, who accepted me as a PhD student, some six-seven years ago. Just because this thesis would have just been nothing without their support, expertise, trust, kindness... And that's how a loop can be formed: the beginning of this section had to be devoted to the genetic parents, the end to the scientific parents. The analogy is quite relevant in that case : one can always define hisself in opposition to what the parents are. Still everybody comes from somewhere, and has to deal with it. The best one can do in my opinion, is to take all pride from this filiation, trying to become someone worth being a father.

PUBLICATIONS

- Peer-reviewed journal articles
  - Averlant, E., Tlidi, M., Thienpont, H., Ackemann, T., and Panajotov, K. (2014). Experimental observation of localized structures in medium size vcsels. *Opt. Express*, 22(1):762–772.
  - Averlant, E., Tlidi, M., Thienpont, H., Ackemann, T., and Panajotov, K. (2016). Vector cavity solitons in broad area vertical-cavity surface-emitting lasers. *Scientific Reports*, 6:20428.
  - Tlidi, M., Averlant, E., Vladimirov, A., and Panajotov, K. (2012). Delay feedback induces a spontaneous motion of two-dimensional cavity solitons in driven semiconductor microcavities. *Phys. Rev. A*, 86:033822.
  - Vladimirov, A., Pimenov, A., Gurevich, S., Panajotov, K., Averlant, E., and Tlidi, M. (2014). Cavity solitons in vertical-cavity surface-emitting lasers. *Philos. Trans. R. Soc. Lond. A*.
- Conference articles published in full-text
  - Averlant, E., Panajotov, K., Ackemann, T., and Tlidi, M. (2014). Cavity solitons in a medium-size vcsel. *Proceedings of the SPIE* volume 9134, pages 913418–913418–6.
  - Averlant, E., Tlidi, M., Ackemann, T., Thienpont, H., and Panajotov, K. (2016). Polarization properties of localized structures in vcsels. *Proceedings of the SPIE* volume 9892, pages 98921E–98921E–7.
  - Averlant, E., Tlidi, M., Vladimirov, A. G., Thienpont, H., and Panajotov, K. (2012). Delay induces motion of multipeak localized structures in cavity semiconductors. In *Semiconductor Lasers and Laser Dynamics V*, volume 8432, page 84321D.
  - Tlidi, M., Averlant, E., Vladimirov, A., Pimenov, A., Gurevich, S., and Panayotov, K. (2015). Localized structures in broad area vcsels: Experiments and delay-induced motion. In Belhaq, M., editor, *Structural Nonlinear Dynamics and Diagnosis*, volume 168 of *Springer Proceedings in Physics*, pages 417–437. Springer International Publishing.
- Publications not related to this thesis

  - International peer reviewed journal article: Tlidi, M., Gandica, Y., Sonino, G., Averlant, E., and Panajotov, K. (2016). Self-Replicating Spots in the Brusselator Model and Extreme Events in the One-Dimensional Case with Delay *Entropy*, 18:64.
  - Conference proceeding: Blaha, S., Averlant, E., Panajotov, K., and Tlidi, M. (2016). Self-organized light bullets in type-I intracavity second harmonic generation *Proceedings of the SPIE*, 9892:989227.

- In preparation
  - Averlant, E., Tlidi, M., Panajotov, K., and Weicker, L. Coexistence of localized structures with different polarization states in a vectorial Lugiato-Lefever model
  - Averlant, E., Tlidi, M., and Panajotov, K. Polarization properties of localized structures in the VCSEL spin-flip model
  - Bahloul, L., Cherbi, L., Hariz, A., Averlant, E. and Tlidi, M. Periodic and localized structures in a photonic crystal fiber resonator

ABSTRACT

In this PhD thesis, we carry out experimental and theoretical studies of localized structures in Vertical-Cavity Surface-Emitting Lasers (VCSELs), also called cavity solitons. Such structures consist of bright peaks of light, localized in space that can be switched on or off, in the plane transverse to the propagation of the beam. They have notably been proposed for two applications: all-optical information processing, and information storage. In the first part of this thesis, we report experimental evidence of spontaneous formation of localized structures in an 80 μm diameter VCSEL biased above its lasing threshold and under optical injection. Such localized structures are bistable with the injected beam power and the VCSEL current. We experimentally investigate their formation for different frequency detunings between the injected beam and the VCSEL. Then, we derive a modified-Swift-Hohenberg equation to describe this system. We characterize localized structures by constructing their snaking bifurcation diagram and by showing clustering behavior within the pinning region of parameters.

In the second part of this thesis, we focus on the vectorial character of localized structures generated in a broad-area VCSEL submitted to linearly polarized optical injection. We provide the first experimental evidence of the vectorial nature of localized structures generated in a broad area VCSEL: the polarization of the cavity soliton is not the one of the optical injection as it acquires a distinct ellipticity. We explain our experimental findings by considering the spin-flip carrier dynamics in the VCSEL quantum well active medium. In a third part, we add a delayed optical feedback to the modified Swift-Hohenberg equation derived in the first part. We show that the delayed feedback induces a spontaneous motion of two-dimensional localized structures in an arbitrary direction in the transverse plane. We characterize moving cavity solitons by estimating their threshold and calculating their velocity. This work is then extended to the more general well-accepted VCSEL-mean field model.

In the last part of this thesis, we consider temporal localized structures generated in nonlinear fiber cavities. We show that when birefringence of a fiber cavity is taken into account, several kinds of localized structures can be generated. These structures differ by their polarization properties. We also describe a photonic crystal fiber cavity by considering second, third and fourth order dispersion. We show that third order dispersion breaks the inversion symmetry and allows localized structures to drift with a constant speed. We have characterized their motion by estimating, analytically and numerically, their linear and nonlinear velocity.

RÉSUMÉ

Dans cette thèse de doctorat, nous menons des investigations théoriques et expérimentales relatives aux structures localisées dans des lasers à cavité verticale émettant par la surface (VCSELs), aussi appelées solitons de cavité. Elles consistent en des pics d'intensité lumineuse dans le plan transverse à la propagation du faisceau lumineux. Ils ont été notoirement proposés pour deux applications : stockage tout optique de l'information, et le traitement de l'information optique.

Dans la première partie de cette thèse, nous investigons les aspects théoriques des structures localisées dans un VCSEL à grande surface d'émission soumis à une injection optique et à un retour retardé. Nous dérivons une équation de Swift-Hohenberg généralisée à retard, d'application lorsque le système est proche du régime de bistabilité optique. En premier lieu, nous caractérisons les structures localisées stationnaires, en construisant leur diagramme de bifurcation en serpentage, typique de leur regroupement dans la zone d'accrochage des paramètres. Ensuite, nous montrons que le retour retardé peut induire un mouvement spontané de structures localisées à deux dimensions dans une direction arbitraire du plan transverse. Nous caractérisons ces structures mobiles en estimant le seuil de ce mouvement, ainsi que sa vitesse.

Dans la deuxième partie de cette thèse, nous rapportons la formation spontanée de structures localisées dans un VCSEL de 80 micromètres de diamètre, pompé au delà de son seuil d'émission laser, et soumis à une injection optique. Ces structures sont bistables en la puissance du faisceau d'injection, ainsi qu'en le courant électrique. Nous étudions expérimentalement leur formation pour différents décalages en fréquence avec le faisceau de pompe optique. Nous rapportons la première mesure expérimentale mettant en évidence le caractère vectoriel des structures localisées générées dans un laser à grande surface d'émission: la polarisation de la structure localisée n'est pas celle de l'injection optique, dans la mesure où cette dernière est elliptique. Nous apportons un éclairage théorique sur cette expérience, en prenant en compte la dynamique de retournement de spin propre aux VCSELs à puits quantique. Ces résultats laissent entrevoir la possibilité de multiplexer l'information transmise en utilisant les propriétés de polarisation des structures localisées, utilisées comme pixels à la surface du VCSEL.

SAMENVATTING

Dit doctoraatsonderzoek richt zich tot het experimenteel en theoretisch bestuderen van gelokaliseerde structuren in Vertical-Cavity Surface-Emitting Lasers (VCSELs), ook wel genaamd cavity solitons. Deze structuren bestaan uit pieken van licht, gelokaliseerd in ruimte die in- of uitgeschakeld kunnen worden, in het vlak transversaal op de propagatie van de lichtstraal. De mogelijke toepassingen van deze structuren bevinden zich voornamelijk in twee domeinen : all-optical image processing, en information storage.

In het eerste deel van deze thesis bestuderen we op theoretische wijze gelokaliseerde structuren in een broad area VCSEL, die voorzien worden van optische injectie en vertraagde optische terugkoppeling. We leiden een algemene vertraagde Swift-Hohenberg vergelijking af voor het VCSEL systeem, dewelke geldig is nabij ontluikende optische bistabiliteit. We karakteriseren eerst de stationaire gelokaliseerde structuren door hun bifurcatie diagram op te stellen en door het clusterend gedrag aan te tonen in de pinning regio van de parameters. Vervolgens tonen we aan dat de vetraagde terugkoppeling een spontane beweging teweegbrengt van tweedimensionele caviteit solitonen in een willekeurige richting in het transversaal vlak. We karakteriseren de bewegende gelokaliseerde structuren door hun treshold in te schatten en hun snelheid te berekenen.

In het tweede deel van deze thesis tonen we experimenteel de spontane vorming van gelokaliseerde structuren in een 80 mm diameter VCSEL met een instelstroom boven de lasing treshold en bij optische injectie. Zulke structuren zijn bistabiel met het geinjecteerde vermogen van de laserstraal en de VCSEL stroom. We onderzoeken experimenteel hun ontstaan bij verschillende frequentie verschuivingen tussen de geinjecteerde straal en de VCSEL, en bij verschillende diameters van de geinjecteerde straal. We leveren het eerste experimentele bewijs van de vectoriele aard van gelokaliseerde structuren in een broad area VCSEL: de polarisatie van de gelocaliserde structuur stemt niet overeen met die van de optische injectie, aangezien deze een andere ellipticiteit aanneemt. Onze experimentele resultaten verklaren we door het spin-flip carrier dynamics in acht te nemen in het VCSEL quantum well actieve medium. Deze resultaten tonen het potentieel aan voor polarisatie multiplexing door caviteit solitonen te gebruiken in broad-area lasers als pixels in informatie technologie.

CONTENTS

1 INTRODUCTION

In this thesis, we study spatially localized structures in Vertical-Cavity Surface-Emitting Lasers (VCSELs). These structures belong to the class of dissipative structures that can be found in systems far from thermodynamic equilibrium. A description of these objects, and their link to optics is the subject of Sec. 1.1. A special emphasis on localized structures generated in VCSELs is made in Sec. 1.2. In Sec. 1.3, we describe polarization studies in two different self-organized systems. Finally, in section 1.4, we present the plan of this thesis.

1.1 DISSIPATIVE STRUCTURES

In their seminal 1968 paper, Prigogine and Lefever derived a trimolecular model (the Brusselator model), to describe the formation of dissipative structures far from equilibrium. These periodic structures appear spontaneously in dissipative environements and are maintained thanks to a permanent exchange of matter and/or energy with their surroundings [1, 2]. A classical example of such dissipative structures has been first predicted by Turing [3]. Contrarly to the Rayleigh-Bénard instability in fluids [4], where the size of the rolls is determined by the geometry of the system, the Turing instability is characterized by an intrinsic wavelength which depends only on the dynamical parameters of the system, such as diffusion coefficients and/or the inverse characteristic times associated with chemical kinetics. The theoretical support of the thermodynamics theory of systems far from equilibrium, developed by Prigogine, made the work of Turing popular. For this reason, it is worth renaming such an instability a Turing-Prigogine instability.

More than several decades later, De Kepper and coworkers [5], as well as Ouyang and Swinney [6], have demonstrated experimental evidence of dissipative structures in Chlorite-Iodide-Malonic Acid reactions. An experimental evidence of pattern formation provided by the authors of [5] is shown in Fig. 1.1. This experiment shows that the pattern wavelength is roughly 0.2mm (as shown in Fig. 1.1c), which exceeds by several orders of magnitude the size of molecules involved in the chemical reaction set. The intrinsic character of the wavelength, predicted by Turing and Prigogine, has been proved experimentally. Indeed, in this experiment, the wavelength measured experimentally is much smaller than the characteristic size of the reactor (its

length is 100 times longer than the wavelength of the pattern). Note that the spatial profile of the dissipative structures shown in Fig. 1.1c) is only a cross section in the horizontal plane. The dissipative structures observed in this experiment are in fact stationary three-dimensional dissipative structures. This is a universal phenomenon leading to spontaneous appearence of a macroscopic order at an intrisic wavelength. This phenomenon has been discussed and observed in almost all fields of natural sciences, such as biology, chemistry, ecology, physics, fluid mechanics, and optics (see a recent overview on this issue [7]).

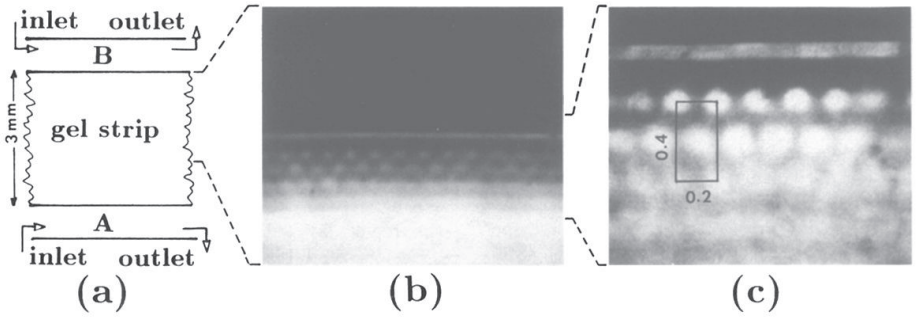

Fig. 1.1: Turing self-organization in a chemical gel reactor. a): schematic of the experimental setup. Both A and B are solutions that are kept at constant concentrations in their different reactants through constant flow. The reactants enter the gel strip through diffusion. The gel strip contains a color indicator for one of the products of the considered chemical reaction. (b) and (c) are photographs of the gel strip demonstrating the appearance of a pattern with an intrinsic wavelength. Reproduced from [5].

In the above described experiment, the time needed to generate a chemical pattern is of order of three hours and its wavelength is around 200μm. These time and space scales are extremely long when being compared to the ones of nonlinear optics and laser physics. By example, in a Vertical-Cavity Surface-Emitting Laser (VCSEL), the dynamics of the system occur in the nanosecond range (the carrier lifetime in a VCSEL cavity). As will be emphasized later in this work , the characteristic scale of a Turing-Prigogine pattern at the surface of a VCSEL lies in the *micrometer* range. This effect makes semiconductor microcavities very attractive systems for applications of dissipative structures.

A Turing pattern has been first numerically observed in an optical system in 1983 (see Fig. 1.2). In that communication, the authors studied a ring cavity with a saturable nonlinearity, submitted to optical injection. In Fig. 1.2, we reproduce their numerical results on the evolution of the operator G_n, which describes the relation

between the slowly varying electric field envelope after n roundtrips in the cavity E_n, and the slowly varying electric field envelope after $n+1$ roundtrips E_{n+1}, as $E_{n+1} = G_n E_n$. Later on, the authors have interpreted their results as a spatial equivalent of a modulation instability [8]: this pattern formation is due to the high transverse wavenumber instability, without any reference to the pattern formation in chemical reactors.

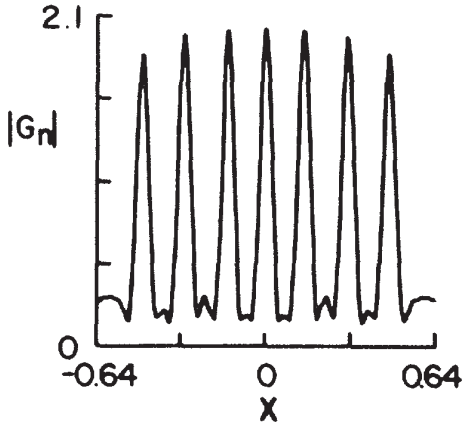

Fig. 1.2: Numerical results obtained by the authors of [9], that describes the evolution of the operator G_n (see text).Reproduced from [9].

The link between optical and chemical patterns has been first established in the paper by Lugiato and Lefever in 1987 [10]. In this article, the authors consider a coherently driven passive ring cavity filled with a Kerr medium. Light propagation inside this cavity is subject to dissipation, pumping, nonlinearity, and diffraction. The slowly varying envelope of the electric field has been averaged on the whole length of the cavity, which constitutes the mean field limit. The originality of the paper by Lugiato and Lefever, when compared to former numerical evidence such as the one described in Fig. 1.2, is that the Turing-Prigogine type of instability does not requires a bistable reponse curve. Indeed, it can happen in a monostable regime where a single homogeneous steady state exhibits a transition from a uniform solution to a self-organized structure that occupies the whole space available in the transverse plane of the cavity. In addition, the authors provide a generic and simple mean field model that has a broad range of applications, from passive cavities to Kerr optical frequency combs and fiber cavities.

Besides periodic patterns which occupy the whole space available in the chemical reactors or in the transverse plane of optical cavities, there exists another type

of structures, which are called localized structures. They consist of either isolated or randomly distributed spots in the spatial profile (of the chemical concentration of a component, or of the electric field intensity). So far, however, such localized structures have never been experimentally observed in a chemical system, even though numerical simulations showing presence of stable localized structures in chemical systems have been succesfully carried out (see e.g. [11]). In optical systems, they have been predicted [12] and numerically demonstrated [13] in 1994. Experimental demonstration has since then been performed in, for example, liquid crystals with optical valve [14], quadratic medium [15], or broad area VCSELs. The next section is devoted to the experimental achievements obtained in localized structure generation in broad area VCSELs, and we will come back to that point later.

Localized structures in optics do not necessarily form in the transverse plane of a propagating beam. They can indeed be generated in passive optical fibers, as has been experimentally evidenced in 2010 [16]. In that case, they consist of a train of pulses equally spaced in time. They will be described in section 1.3.2.

1.2 DISSIPATIVE LOCALIZED STRUCTURES IN VCSELS

Broad area VCSELs are choice materials for drawing localized structures, and they are widely used in that context (see recent reviews on that matter [17, 18, 19, 20]).

The first theoretical descriptions of localized structures formation in VCSELs were made in the late nineties [21, 22, 23]. In these works, the authors all consider mean field models, that will be investigated in chapters 2 and 3. Shortly afterwards, in 2000, localized structures were experimentally demonstrated in semiconductor microcavities [24]. In that communication, the authors used an extremely wide area resonator (10×20 mm^2), illuminated by rather small area (60μm diameter) optical injection beams. Two beams were used, so that one of them has been used to ensure bistability of the device (we refer to this beam as the *holding beam* or *optical injection* in the continuation of this work), and the second is used for localized structure generation (referred to as *writing beam*). The microresonator transverse size was actually too wide to be held at room temperature in a homogeneous manner. Even though this device was not electrically but optically pumped, it qualifies as a VCSEL because of its structure. The localized structures that have been generated in this configuration tend to place themselves at the maximum of the gaussian intensity optical injection. The measurements performed in this communication have been performed within an observation time of a few microseconds, to avoid thermal effects.

It was only in 2002 that localized structures in VCSELs could be stabilized over a macroscopic time (more than a minute) [25]. The authors also demonstrated in that communication that the phase of the writing beam could be changed in order to erase localized structures. Their experimental data is presented in Fig. 1.3. In that article, the authors claimed that the VCSEL was "operating at current values for which the center region is under threshold." Interestingly, that does not mean that the VCSEL was biased below its optical threshold. Indeed, as will be investigated in chapter 2, when broad area VCSELs are pumped close to their lasing threshold, their emission pattern is located at the boundaries of the surface emission. This effect is well-known, and is due to current crowding [26, 27]. That being said, their claim of using the laser under its lasing threshold is definitely justified, as the region in which localized structures are generated does not lase. These localized structures are created on the border between a nonlasing state (on the right side of Fig. 1.3(a)-(l)) and a patterned state. The fact that a region of the surface of the VCSEL presents a patterned state, and that the other presents a homogeneous emission is due to the thickness difference in the cavity. This difference induces a shift in the cavity resonance in the horizontal direction of the VCSEL chip surface of Fig. 1.3.

In 2006 [28] localized structures have been generated in a VCSEL biased above its lasing threshold for the first time. That is, the VCSEL was lasing over its whole emission surface. The authors also demonstrate the spontaneous appearance and disapearing of a localized structure when the optical injection power was swept up and down.

At the same time, a new scheme for generating localized structures in a more compact manner has been introduced: it consists of a VCSEL with incorporated saturable absorber [29, 30, 31]. The main interest of this new scheme is that the saturable absorber already provides multistability to the system, and there is hence no more need for a holding beam to ensure Turing instability. The first experimental realization has been achieved in 2009 [32].

In 2008, a team of the University of Strathclyde in Glasgow developped a *"cavity soliton laser"*, i.e. a laser that does not require a holding beam to generate localized structures. To this aim, they used optical feedback from a diffraction grating [33]. This feedback is filtered, so that only one frequency component is sent back to the VCSEL. The experimental setup is presented in Fig. 1.4a). This setup has been improved two years later, by changing the diffraction grating into a volume Bragg grating, that is much less sensitive to the polarization of light [34]. At the same time, and in a similar attempt to build a robust system for VCSEL-based localized structure generation, a team at the Institut Nonlinéaire de Nice developed a cavity soliton laser based on two mutually coupled VCSELs [35]. This device is depicted in Fig. 1.4b).

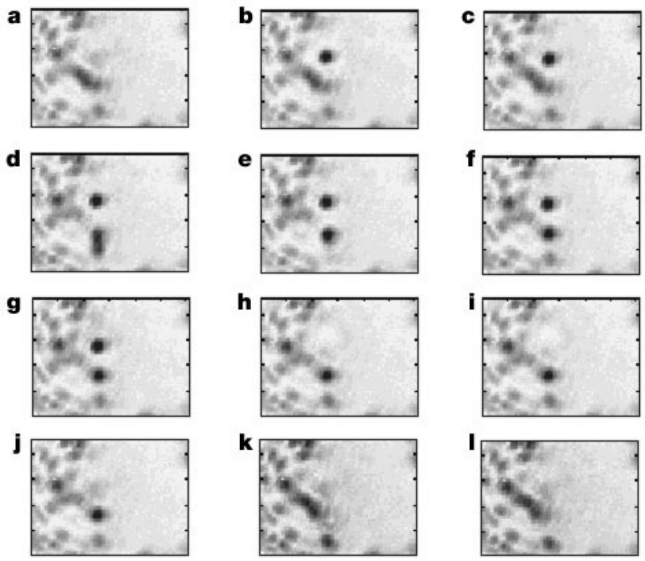

Fig. 1.3: Localized structures in an electrically pumped broad area VCSEL. In frame a), the VCSEL is submitted to the holding beam only. In frame b), the writing beam is turned on, and a localized structure appears. In frame c), the writing beam is turned off, and the localized structure stays in place. In frame d), the writing beam is moved to another position, and it ignites another localized structure. In frame e) and f), the writing beam is turned off, and the two localized structures coexist. In frame g), the writing beam is positioned on its first position, and its phase is shifted by 180°. It erases the localized structure, as seen in frame h). Frames i) to l) correspond to the repetition of this procedure for the lower spot.Reproduced from [25].

In this configuration, one VCSEL is used as a pump, and the other is used as a saturable absorber. Both configurations allow to generate localized structures.

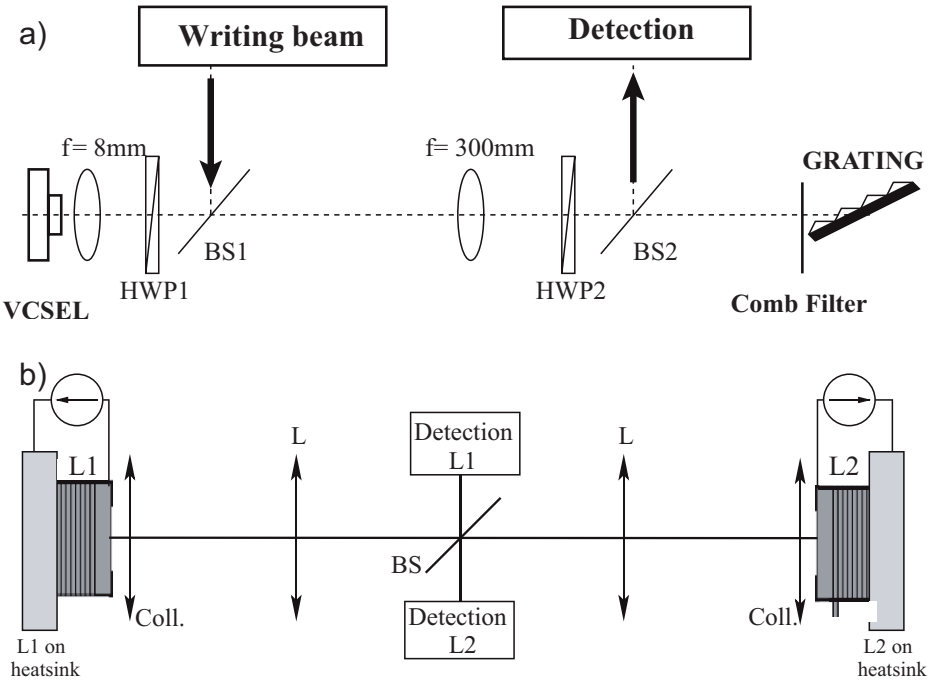

Fig. 1.4: a): Experimental setup described in [33]. The VCSEL is placed in an external cavity, where half-wave plates are used to enhance or reduce reflectivity on the diffraction grating, as well as to control the polarization state of the incoming light. b): two VCSELs in a face-to face configuration. The absence of a holding beam allows to drastically reduce the complexity of the system. Reproduced from [36]

It is well known that in most of these systems, a phase gradient can set the localized structures in motion [37]. In this publication, the authors suggest that this phenomenon can be used for utilizing localized structures as an all optical delay line. A drift of localized structures can also be induced by the diffraction grating frequency-selective feedback described in [33]. In that case, the finite spectrum of the localized structure induces an asymmetry in the feedbacked field, that overimposes a phase gradient over the surface of the localized structure.

A second use for the phase gradient induced drift has been proposed in [38]. It consists of mapping the defects at the surface of a semiconductor emission window. Indeed, as a localized structure is set in motion, it will be attracted by local defects. If

one places a phase gradient on the optical injection, the deviations from the direction of the gradient can be interpreted as defects, and a mapping of the surface can be realized.

1.3 VECTOR CHARACTER OF DISSIPATIVE STRUCTURES

As polarization is a fundamental characteristic of light, polarization studies in light dissipative structures have been carried out quite early, especially in dissipative structures generated in gas cells (see a review published in 1998 dedicated to that topic [39]). In particular, two theoretical studies are particularly relevant to that field: [40, 41]. Considering a generalization of the Lugiato-Lefever model adapted for polarization studies, the authors investigate the formation of patterns [40] and localized structures [41].

In this section, we will restrict ourselves on two other systems, in which polarization plays a crucial role: VCSEL-based systems, and optical fibers.

1.3.1 *Polarization studies of dissipative structures in VCSELs*

Dissipative structures generated in VCSELs submitted to optical injection are most often studied in the case when the VCSEL is polarization locked to optical injection. However, because of the spin-flip mechanism inherent to VCSELs described in [42], this is not necessarily the case, even if the VCSEL is frequency locked to optical injection. Moreover, even if the spin-flip mechanism is neglected, there is an interplay between the two linear polarization components in the VCSEL that is due to the carrier population [43]. In this article, the authors consider a medium area VCSEL (40μm diameter) submitted to an optical injection that has its linear polarization crossed to the one in which the VCSEL spontaneously lases in (the *principal polarization* of the VCSEL) when being electrically pumped close to threshold. When sweeping the pump current, they observe bistability of a bright dot located in the center of the VCSEL, polarized in the direction of the optical injection. Interestingly, the near field profile of the VCSEL stays unchanged in the VCSEL principal polarization direction, whether the orthogonal linear polarization component contains a localized structure or not.

Localized structures in VCSELs *not* submitted to optical injection have attracted considerable interest. In the first frequency selective feedback system [33], the reflectivity of the diffraction grating is polarization dependant, and it is hence not adapted, according to the authors, to polarization studies. The research team in the photonics

center of Strathclyde hence decided to replace the diffraction grating by a volume Bragg grating, that is much less sensitive to the polarization properties of the incoming light [34]. In this article, the authors measured the orientation of the principal axis of the polarization ellipse. A first step has been made, but, to fully characterize the polarization state of light, the ratio between the two linearly polarized components of this ellipse needs to be measured, as well as the direction followed by the polarization on its ellipse.

However, to this day and to our knowledge, there has not been any other experimental studies on the polarization state of localized structures in VCSELs, regardless of the technology used to generate them.

1.3.2 *Polarization studies of dissipative structures in fibers*

Optical fibers are quite adapted for polarization studies. In fact, two different kinds of vector dissipative localized structures can be generated in optical fibers: Polarization Locked Vector Soliton (PLVS), and Group Velocity Locked Vector Soliton (GVLVS). They differ in the sense that PLVS propagate inside a fiber cavity preserving their shape and polarization properties (even though the polarization state of the localized structure can vary between the beginning and the end of the pulse), while GVLVS constantly change their polarization state during their propagation. PLVS have been studied from 1994 onwards [44]. In this article, the authors theoretically consider a set of coupled nonlinear Schrödinger equations to describe a fiber ring cavity. They study the competition between polarization modulation instability, and scalar modulation instability. Please note that this article does not involve localized structures, but modulation instability (which is the temporal equivalent in optical fibers of a Turing pattern). However, the authors published the same year a theoretical study that describes GVLVS [45], still in the framework of modulation instability.

Both types of vector temporal localized structures have been demonstrated experimentally [46] in an erbium doped fiber laser in 2000. Note however, that the authors do not interpret their results in terms of dissipative structure [47]. Nevertheless, the very fact that these solitons are generated in a fiber laser, which is an out-of-equilibrium system, subject to losses and energy input, makes these structures dissipative structures, even when they are not described that way.

A lot of different systems have been used for generating temporal localized structures in fiber lasers since then, notably carbon nanotubes [48], or a semiconductor saturable absorber inside the fiber cavity [49]. The experimental realizations presented so far have been achieved in fiber lasers. In fact, experimental localized

structure polarization studies in optical fibers have been to our knowledge limited to fiber lasers.

1.4 STRUCTURE OF THIS THESIS

The most important part of this work is devoted to the study of localized structures in VCSELs.

In the second chapter, we provide experimental evidence of spontaneous formation of localized structures in a 80μm diameter VCSEL biased above its lasing threshold and under optical injection. We show that such localized structures are bistable with the injected beam power and the VCSEL current. Then, we derive a generalized delayed Swift-Hohenberg equation for the VCSEL system, which is valid close to the nascent optical bistability. We characterize the localized structures found in that system by constructing their snaking bifurcation diagram and by showing clustering behavior within the pinning region of parameters.

In the third chapter, we report the experimental observation of two-dimensional vector cavity solitons in a VCSEL under linearly polarized optical injection when varying optical injection linear polarization direction. The polarization of the cavity soliton is not the one of the optical injection as it acquires a distinct ellipticity. These experimental results are qualitatively reproduced by the spin-flip VCSEL model.

In the fourth chapter, we show that localized structures generated in a VCSEL submitted to a delayed optical feedback are set into motion by this delayed feedback, in an arbitrary direction. We characterize moving cavity solitons by estimating their threshold and calculating their velocity. In addition, we discuss the impact of the phase of the time-delayed optical feedback in the full model. Both analytically and numerically, we establish an expression for the velocity associated with the motion of localized structures.

In order to extend our results to temporal localized structures in fibers, we devoted Chapter 5 to their study. In the first part of this chapter, we study the polarization properties of localized structures in low birefringence coherently driven fibers. We show that two different kinds of localized structures can coexist in the same parameter set. These structures differ in their polarization properties. In the second part of this chapter, we show that temporal localized structures in low dispersion optical fibers can exhibit a motion due to high order dispersion.

2 SCALAR LOCALIZED STRUCTURES IN VCSELS

In this chapter, we first describe the experimental setup that has been used to study scalar localized structures in broad area VCSELs. Then we present the experimental results obtained with this setup. Next, we present a VCSEL model that takes into account interaction of light and carriers. Based on it, we derive a modified Swift-Hohenberg equation that describes the spatio-temporal dynamics of the electric field in the nascent bistability regime, before building a snaking bifurcation diagram. The last part of this chapter deals with the use of this model to characterize the formation of localized structures, by constructing their bifurcation diagram.

2.1 EXPERIMENTAL SETUP FOR LOCALIZED STRUCTURES IN A 80μM VCSEL

A photography and a scheme of the experimental setup dedicated to experimental investigation of light localized structures are displayed in Figs. 2.1 and 2.2, respectively. The scheme of Fig. 2.2 is divided in three parts:

- Injection preparation and monitoring
- VCSEL
- Analysis branch

In section 2.1.1, we will discuss the properties of the 80μm diameter VCSEL we use in the experiment. Section 2.1.2 is devoted to optical injection preparation and monitoring whereas Sec. 2.1.3 deals with analysis of the output beam.

2.1.1 *The standalone VCSEL*

The broad-area bottom emitting VCSEL we use in our experiments is obtained through a collaboration with Prof. Thorsten Ackemann, from University of Strathclyde, in Glasgow. It is described in Fig. 2.3. The top and bottom Distributed Bragg Reflectors (DBRs) consist of 30 and 20.5 $Al_{0.88}Ga_{0.12}As$–GaAs layer pairs, respectively. The active region consists of three $In_{0.2}Ga_{0.8}As$ quantum wells embedded in GaAs barriers and AlGaAs cladding layers [26]. The bottom-emitting configuration allows

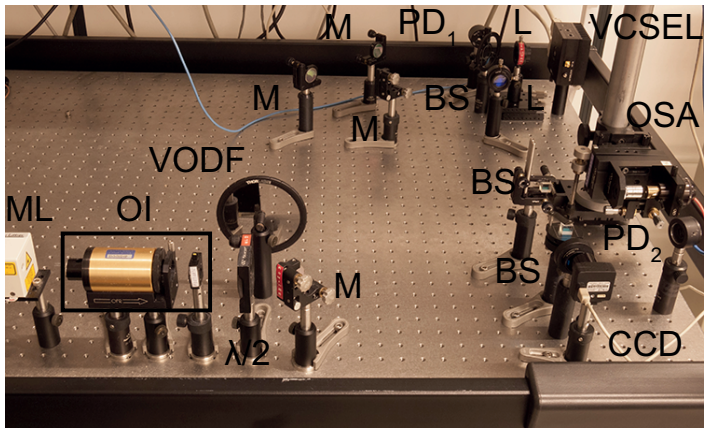

Fig. 2.1: Experimental setup photography. ML: master laser, OI: optical isolator, $\lambda/2$: half wave plate, M: mirror, VODF: variable optical density filter, PD: photodiode, OSA: optical spectrum analyser, L: lens, BS: beam splitter. CCD: CCD camera.

the stand-alone VCSEL to have a better (more homogeneous) current distribution in the transverse plane and, therefore, is more suitable for producing LSs. Moreover a heat sink can be directly mounted on top of the p-contact and the p-doped DBR, which is the main source of heat. The temperature distribution is hence more homogeneous as well.

To ensure a constant temperature of the VCSEL substrate, the VCSEL temperature is controlled and monitored using an integrated circuit temperature transducer (AD592AN) and a Peltier thermoelectric cooler (both built in a Thorlabs TCMLD9 cage) controlled by a Thorlabs PRO8-ITC8052 module. The same module allows to control the injection current. This configuration allows temperature and current stabilities of $\Delta T = 0.001°$C, and $\Delta I = 1\mu$A, respectively.

When kept at $25°$C, the lasing threshold of this VCSEL is $I_{th} = 42.0$mA. When the current is maintained slightly above I_{th}, the near field of this VCSEL displays circular standing-wave patterns along the perimeter that resembles of the one observed in smaller area VCSELs [43]. Such a pattern is sometimes referred to as flower-like, or daisy mode [27]. In broad-area VCSELs, this daisy mode has much more maxima, which indicates a much higher azimuthal order. A near field image for $I = 45.0mA$ is shown in Fig. 2.4(a). The corresponding optical spectrum is plotted in Fig. 2.4(b). This spectrum contains two relatively closely spaced wavelengths, which indicates that the flower mode of Fig. 2.4(a) is not a single transverse mode. Both of these measurements have been performed at a temperature of $T_{sub} = 25.0°$C.

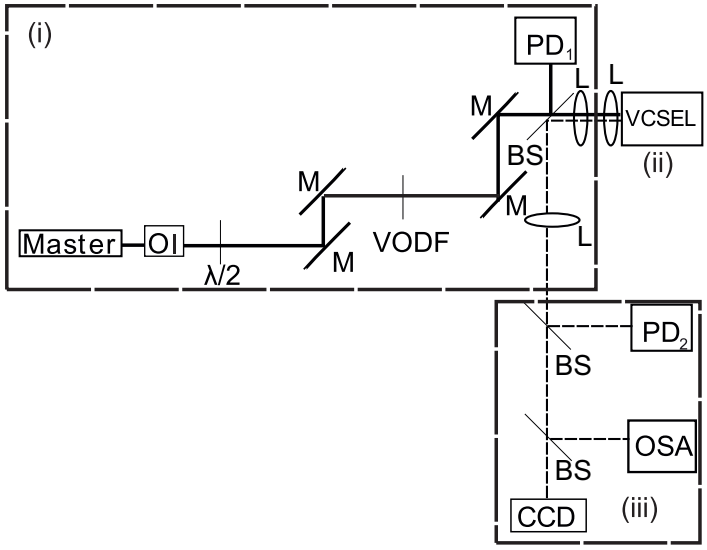

Fig. 2.2: Experimental setup schematic. The full line is the path of the light from the master laser, whereas the dashed line is the path followed by the light from the VCSEL. (i): injection preparation and monitoring; Master: master laser, OI: optical isolator, $\lambda/2$: half wave plate, M: mirror, VODF: variable optical density filter; (ii) : VCSEL; (iii): analysis branch; PD: photodiode, OSA: optical spectrum analyser, L: lens, BS: beam splitter.

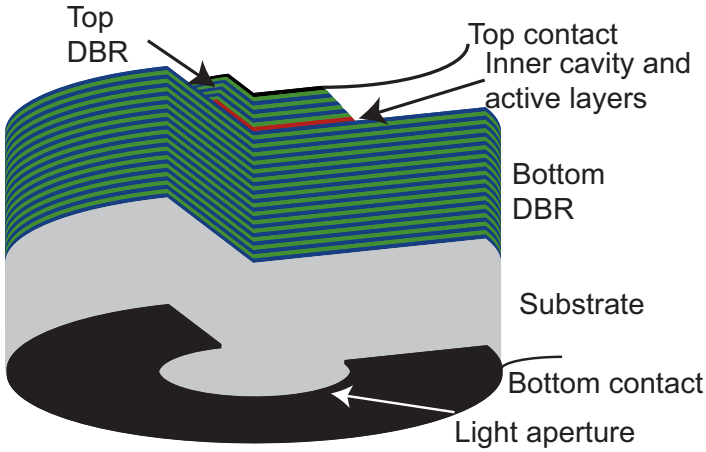

Fig. 2.3: 3D representation of a bottom-emitting InGaAs quantum well VCSEL, as used in the experiment.

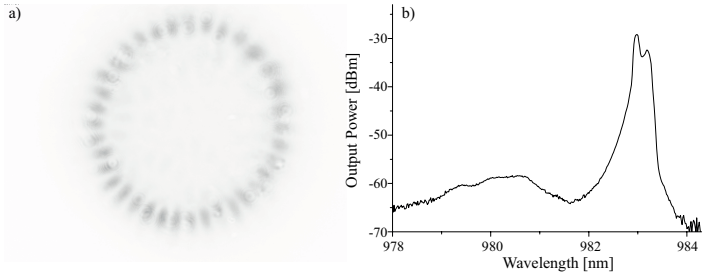

Fig. 2.4: Solitary VCSEL characteristics obtained for $I = 45.0$mA and $T_{sub} = 25.0°$C. (a): near field profile in the transverse plane. Black corresponds to high optical power whereas white corresponds to low optical power. (b): the corresponding optical spectrum.

2.1.2 *Injection branch: preparation and monitoring*

To provide the optical injection, we use a commercial external cavity diode laser from Sacher Lasertechnik TEC-100-0960-060 controlled by a Sacher Lasertechnik MLD-1000 laser driver. This device consists of a temperature-controlled anti-reflection coated laser diode and a diffraction grating set in a Littrow configuration. The external cavity Littrow configuration is described in Fig. 2.5. This system yields 60mW single mode linearly polarized output and a wavelength tunable between 910nm and 985nm, with a 24 hour drift of 300MHz. As the output from this device is linearly polarized, we can use an optical isolator for avoiding unwanted feedback to this laser. To this purpose, we use an Optics For Research IO-5-TIS2-HP optical isolator, that provides 10dB isolation at 983nm.

The output linear polarization is then tuned to match the one of the VCSEL, using a Thorlabs WPH05M-980 half-wave plate. The direction of the beam is then tuned using four Thorlabs BB1-E03 dielectric mirrors so that optical injection is easily achieved. Finally, just before encountering the VCSEL, a small part of the beam is taken into a photodiode (Newport 818-SL), for the sake of monitoring the input power. This is performed using a Thorlabs BP108 pellicle beamsampler.

Most lenses of the setup are at the boundary between the injection and analysis branches. They allow the light from the master laser to be collimated when it encounters the VCSEL, and the light in the direction of the analysis branch to be collimated as well. A scheme for the lens arrangement is described in Fig. 2.6

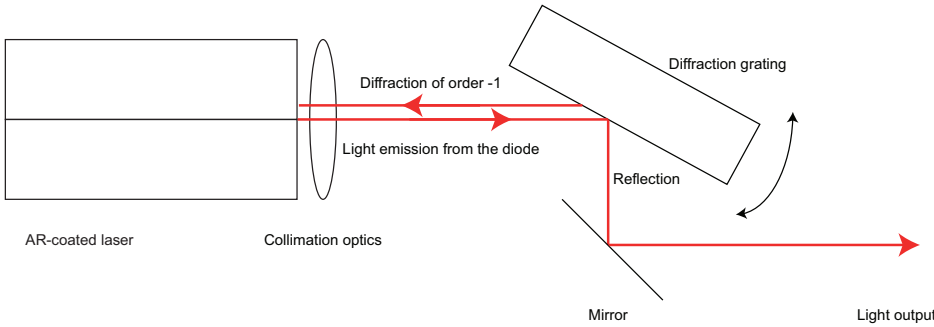

Fig. 2.5: Littrow configuration for external cavity laser diodes. The AR-coated laser diode light is collimated and encounters a reflective diffraction grating. Reflection on this grating is used as light output, whereas the order -1 of diffraction is sent back to the laser diode. The inclination of the diffraction grating determines which wavelength can be sent back to the diode, and can produce laser emission. This inclination can be tuned using a piezoelectric crystal connected to a voltage supply.

2.1.3 *Analysis branch*

The analysis branch consists of three elements:

1. A fiber coupling unit that is connected to an Optical Spectrum Analyzer (OSA) (Ando AQ6317B);
2. A photodiode, identical to the one used for injection monitoring;
3. A CCD camera (Point Grey Research CMLN-13S2M-CS).

For every measurement that has been performed, every measurable parameter has been acquired via MATLAB routines (namely temperature and current of the VCSEL, injection power, power on the second photodiode, near field profile of the VCSEL, and spectrum of the latter).

2.2 EXPERIMENTAL OBSERVATION OF LOCALIZED STRUCTURES IN A BROAD-AREA VCSEL

In this section, we will use the experimental setup described in Sec. 2.1. The first section will be devoted to a description of the optically injected VCSEL, whereas the latter will describe the localized structures generation *per se*.

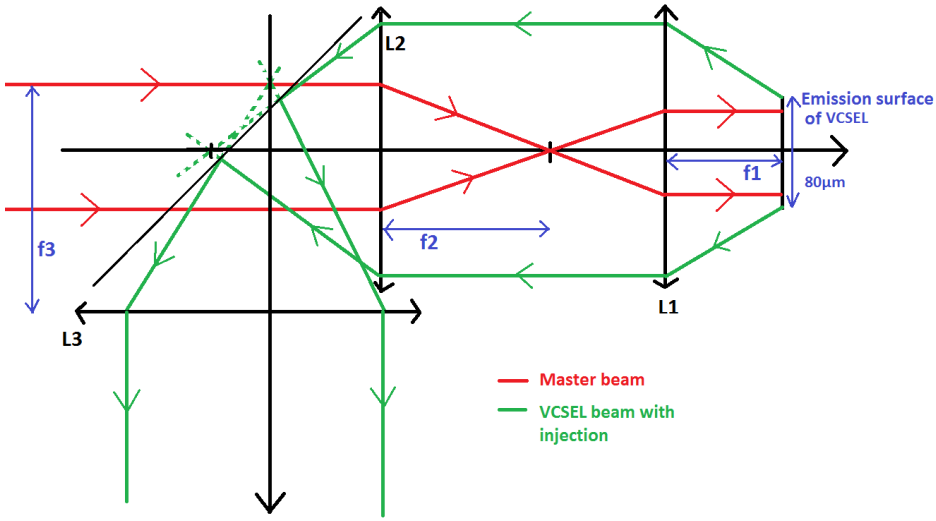

Fig. 2.6: Lenses arrangement at the boundary between injection and analysis branches. L1 and L2 play the role of a telescope for the injection beam (right travelling rays), whereas the light coming from the VCSEL is collimated by L1, before encountering L2 and L3, that play the role of a telescope towards the analysis branch (left travelling rays).. L_1 is a Thorlabs C330-TME-B aspheric lens with focal length f_1=3.1mm, L_2 is a Thorlabs LA1131-B, of focal length f_2=50.0mm. L_3 is a Thorlabs LA1986-B, with focal length f_3=125.0mm. All lenses are anti-reflection coated in the wavelength range 650-1050nm. Reprinted from [50]

2.2.1 *Optically injected VCSEL*

In this section, the VCSEL is kept at 25.0°C, while its current is set at 45.0mA. For the VCSEL to be locked to the master laser, three conditions need to be fulfilled [51]:

- The locking wavelength (of the master laser) needs to be longer than the free running one (of the slave VCSEL);
- The frequency difference needs to be small;
- The master laser power needs to be high enough: as a general rule, the larger the detuning, the higher the master laser power needs to be for locking to occur.

The two first conditions are most often expressed as follows, in terms of frequency: the frequency detuning $\theta = \nu_M - \nu_S$, where ν_M is the frequency of the master laser and ν_S the frequency of the slave laser, needs to be negative and small enough for locking to occur.

The fact that the VCSEL is injection-locked or not can be seen two ways: first, as the VCSEL is locked, the characteristic daisy mode that the VCSEL exhibits in its near field profile when being pumped close to its current threshold disappears. Second, it can also be seen in the optical spectrum. Indeed, when the VCSEL is locked, its lasing peaks disappear, to the advantage of a new peak, at the injection wavelength.

Measurements of optical spectra of the optically injected VCSEL are shown in Fig. 2.7, alongside with the corresponding near field profiles. In Fig. 2.7a), the optical power of the master laser is $P_{inj} = 850\mu$W. In that case, we can see that the VCSEL is not locked to the optical injection, for two reasons. First, even if the near field profile changes a lot, its boundary still exhibits a flower mode. Second, an examination of the spectrum shows that even it is is strongly modified by the optical injection, the peak corresponding to the optical injection is accompanied by a lower intensity one, at a shorter wavelength. In Fig. 2.7b), the optical power of the master laser is $P_{inj} = 2.04$mW. Here, the VCSEL is locked to the optical injection, as can be seen with the "flower-free" near field profile and the spectral peaks of the free running VCSEL that disappear completely.

2.2.2 *Experimental observation of localized structures in 80μm diameter VCSEL*

All the measurements described in this section are performed while the VCSEL is frequency locked to optical injection. The experimental setup is the one described in

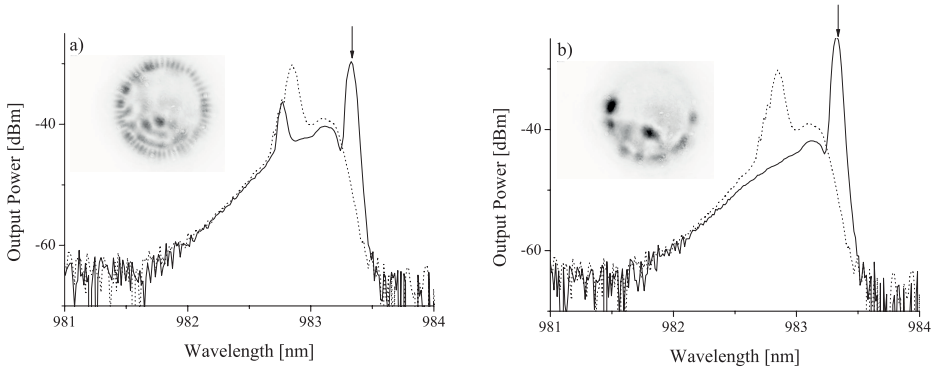

Fig. 2.7: Dashed lines: optical spectra of the free running VCSEL obtained for $I = 45.0$mA and $T = 25.0°$C. Solid lines: optically injected VCSEL with $\lambda_{inj} = 983.24$nm (indicated by a vertical arrow) and injection power of (a) $P_{inj} = 850\mu$W and (b) $P_{inj} = 2.04$ mW. The insets are near field images of the optically injected VCSEL.

Fig. 2.2. The experimental procedure reads as follows: first, the power of the master laser is set to a maximum. The second step is to perform the fine alignment, to allow the master laser to be injected in the VCSEL. Third, the wavelength of the master laser is set. Last, the power of the master laser is tuned up and down, using the variable optical density filter. At each measurement, a whole set of data is recorded from the instruments: injection current of the VCSEL, temperature of the VCSEL substrate, optical spectrum, power at both photodiodes PD_1 and PD_2, and near field profiles. A sudden change in the experimental conditions can indeed have several sources. By example, one needs to discriminate between the appearance of a localized structure and a change in the near field pattern induced by a slight change in the injection spectrum. Such a change in the injection spectrum can be due to mode hopping in the master laser.

Injected light-output power curves are displayed in Figs. 2.8, 2.10 and 2.11. Optical bistable regions are easily visible with a hysteresis region for increasing and decreasing optical power. On each of those light-output curves, there are insets displaying the near field profiles on the lower and higher branches of the bistable curve. While being recorded at different injection currents, optical injection wavelengths, and different VCSEL substrate temperatures, they all exhibit the same behavior: from a lower branch containing a pattern made of some bright spots, as one increases the input optical power, one can see the overall output power increase linearly, up to a certain power P_{up}. At this very point, the output power undergoes an abrupt increase, that is correlated with the appearance of a new bright spot. From

this point, if one then decreases the optical injection power, it will decrease linearly down to a certain power P_{down}. At this point, the formerly mentioned new bright spot disappears. The fact that $P_{up} > P_{down}$ is a display of hysteresis, that is a fundamental characteristic of localized structures. This is a manifestation of the nonlinear mechanisms responsible for their appearance.

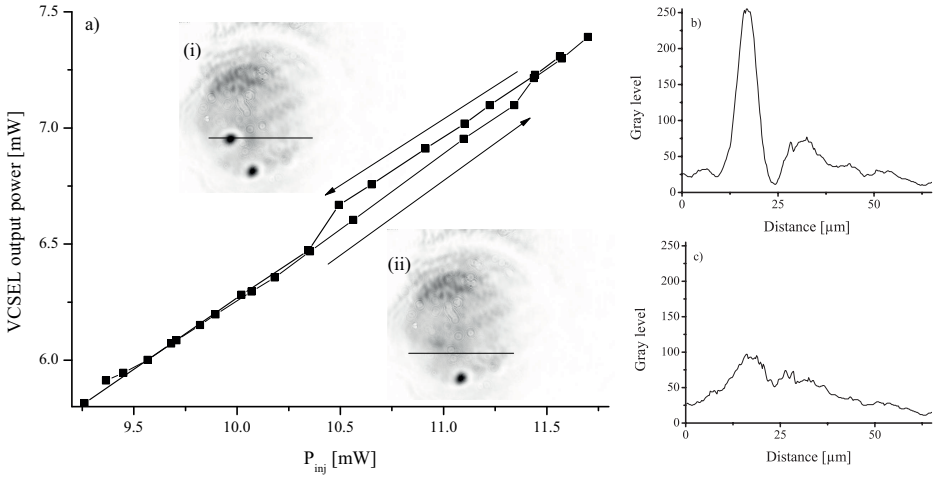

Fig. 2.8: Bistability between one and two-peaked LSs inside the near field of the VCSEL as a function of the optical injection power. (a): power emitted by the VCSEL as a function of the optical injection power for frequency detuning between the master laser and the VCSEL of $\theta = -174$GHz. The insets (i) and (ii) respectively represent near field profiles on the higher and lower branch of the hysteresis. (b) and (c): one dimensional profiles along the horizontal line drawn on the aforementioned insets.

In Fig. 2.8b), and c), cross sections of the different near field profiles are presented. Localized structures can be recognized as well defined peaks. Several accompanying peaks are also visible in their characteristic oscillating tails, whose amplitude decays with the distance to the center of the localized structure. To better apprehend them, one can draw a one dimensional plot on a defined line of the near field presented as insets in the bistability curves (see Fig. 2.9). This is, to our knowledge, the first experimental evidence of such oscillating tails in VCSELs, even though they have been demonstrated in other optical pattern forming systems [52, 53, 54].

This method can be used to draw and erase several localized structures. This manifestation of the multistability inherent to localized structures is shown in Fig. 2.12. Here, as the energy input is increased, the system switches to a 2-peaked structure to a 4-peaked one. When this quantity is decreased, instead of switching back

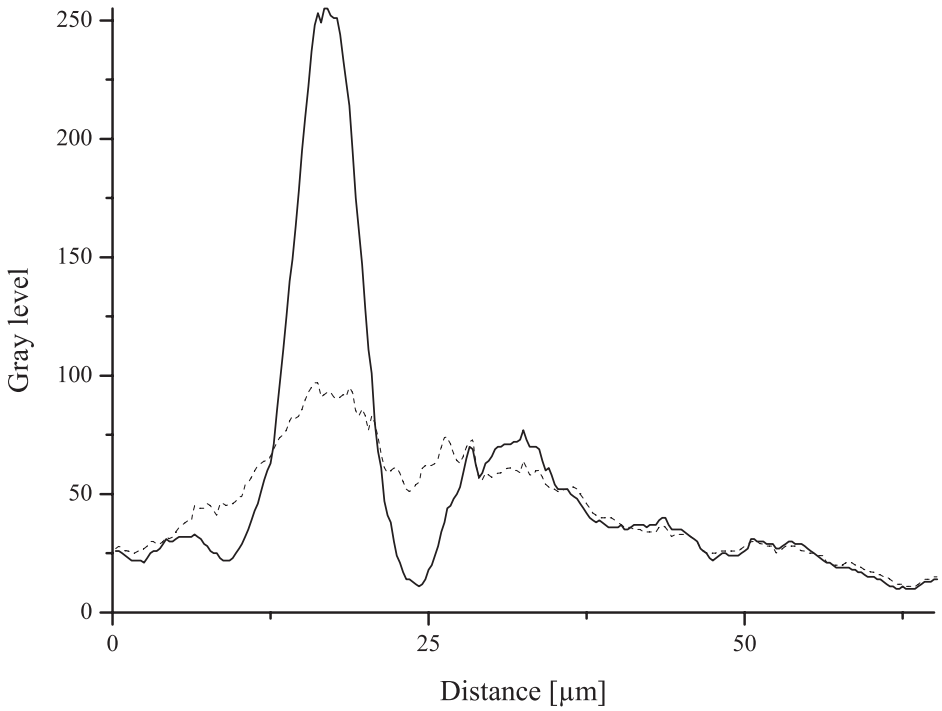

Fig. 2.9: One dimensional profiles of the localized structure depicted in Fig. 2.8b) (full line), and c)(dashed line). The full line is the state in which a localized structure is present, whereas the dashed one represents the lower branch of the hysteresis.

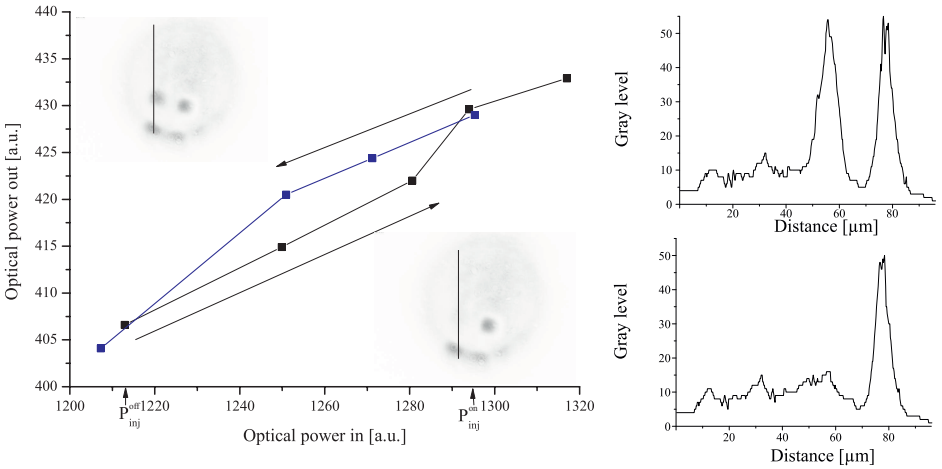

Fig. 2.10: Bistability between one and two-peaked LSs inside the near field of the VCSEL as a function of the optical injection power. Left: power emitted by the VCSEL as a function of the optical injection power for $\theta = -146$GHz. The insets represent near field profiles on the higher and lower branch of the hysteresis. Right: one dimensional profiles along the vertical lines drawn on the aforementioned insets.

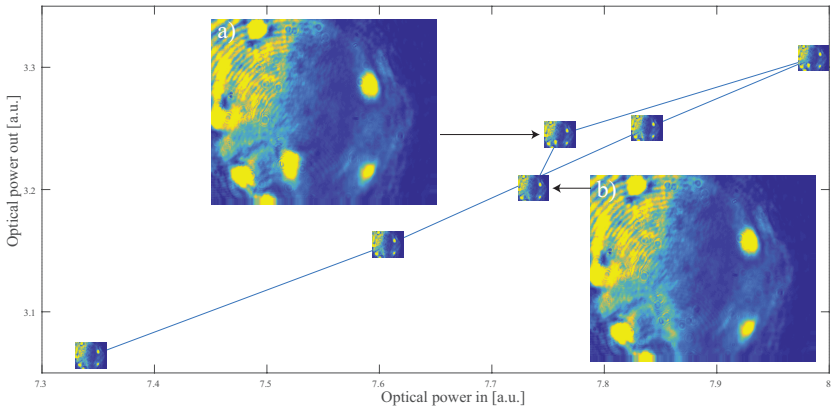

Fig. 2.11: Power emitted by the VCSEL as a function of the optical injection power. The insets represent near field profiles on the higher and lower branch of the hysteresis.

abruptly to the 2-peaked state, the system transits via a 3-peaked state, before switching effectiveley to a 2-peaked state.

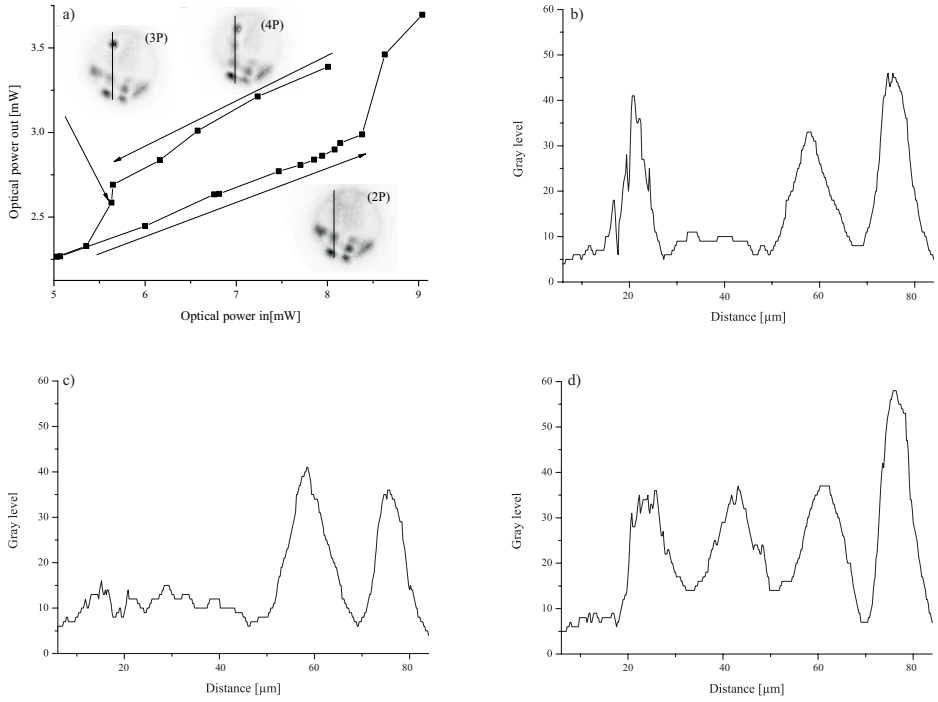

Fig. 2.12: Bistability between three states inside the near field of the VCSEL as a function of the optical injection power. (a): power emitted by the VCSEL as a function of the optical injection power for $\theta = -118$GHz. The insets (2P) and (3P) and (4P) represent near field profiles of the three possible states of the system. (b), (c) and (d): one dimensional profiles along the vertical line drawn on the aforementioned insets.

The bistable behavior of switching on and off of a localized structure in broad area VCSEL can also be observed while varying, instead of the optical injection power, the VCSEL current. An example thereof is presented in Fig. 2.13.

To sum up this experimental part, we investigated the formation of two dimensional localized structures in the transverse section of a 80μm diameter VCSEL. Bistability corresponding to spontaneous appearance and disappearance of a localized structure has been observed, as a function of optical injection power, and as a function of VCSEL current. Oscillating tails of the localized structures have been observed. Localized structures have also been shown to exhibit multistability.

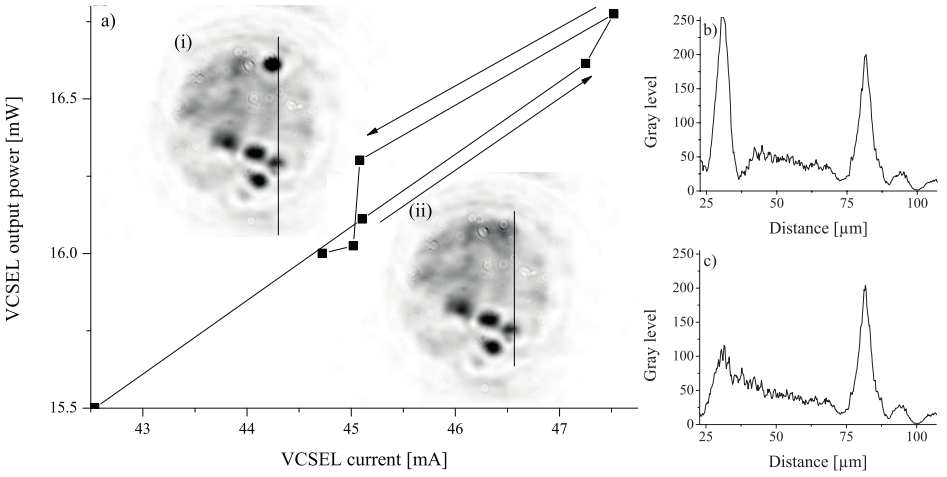

Fig. 2.13: Bistability between two states inside the near field of the VCSEL as a function of the VCSEL current. (a): power emitted by the VCSEL as a function of the VCSEL current. The bistable region of the curve has its detuning θ varying between -185GHz and -166 GHz due to the current induced thermal red shift. The insets (i) and (ii) represent near field profiles of the two possible states of the system. (b) and (c): one dimensional profiles along the vertical line drawn on the aforementioned insets.

All of these measurements have been performed while the linearly polarized optical injection has its direction matching the one in which the VCSEL spontaneously lases while being pumped close to its current threshold.

2.3 THEORETICAL DESCRIPTION OF BROAD AREA VCSELS

In this section, we first describe the validity range and formulation of the VCSEL mean field scalar model [23]. Then, we derive a single scalar equation, valid in the nascent bistability regime.

2.4 VCSEL MEAN-FIELD SCALAR MODEL

To describe the electric field emittted by a VCSEL, we consider the mean field model obtained in the slowly varying envelope (variations of the envelope of the electric field happen on a timescale much longer than the propagation oscillations) and paraxial approximations of the coupled Maxwell-Bloch equations described in [42]. In this section, we focus on the scalar case, where the polarization degrees of freedom are not taken into account (the vector model will be discussed in Chap. 3). In this approach, the electric field is coupled to only one excitonic line, in resonance in the cavity. This means that the continuous absorbtion band that alters the high frequency side of the excitonic line in the absorbtion spectrum of the semiconductor material is neglected.

We assume that the cavity has a large Fresnel number (that is, a larger aspect ratio). In addition, we assume that the cavity is much shorter than the diffraction, diffusion, and nonlinearity characteristic scales. We further simplify the problem by assuming a single longitudinal mode approximation. Under these approximations, the adimensional electric field envelope E and carrier density Z evolve in time according to the following partial differential equations [23]:

$$\frac{\partial E}{\partial t'} = -(1+\eta+i\theta)E + 2C(1-i\alpha)(Z-1)E + i\nabla_{\perp}'^2 E + E_I, \tag{2.1}$$

$$\frac{\partial Z}{\partial t'} = -\gamma\left[Z - I + |E|^2(Z-1) - d_f\nabla_{\perp}'^2 Z\right], \tag{2.2}$$

In these equations, η is a dissipation term for the electric field, θ is the cavity detuning parameter, E_I is the optical injection strength, C is the bistability parameter, and α is the linewidth enhancement factor. The transverse Laplacian acts in the plane transverse to the propagation of light, and its action accounts for diffraction in the

paraxial approximation (electric field equation), and for diffusion of the carriers (carriers equation). γ is the decay rate for carriers, and I is the current. All quantities have been renormalized, including space and time. Details of this renormalization can be found in Chap. 3.

2.4.1 *Modified Swift-Hohenberg equation*

Near the second order critical point associated with optical bistability, the Maxwell-Bloch equations describing a laser under optical injection can be described by a real parameter Swift-Hohenberg equation [55]:

$$\frac{\partial X}{\partial t} = 4y + X(\mathcal{C} - X^2) - 4a\Delta\nabla_\perp^2 X - \frac{4}{3}a^2\nabla_\perp^4 X. \tag{2.3}$$

In this equation, some parameters and variables denote deviations from the onset of optical bistability: X is the one from the electric field, y is the one from the optical injection strength and $\mathcal{C}$ is the one from the cooperativity parameter. a is proportional to the spacing between two adjacent modes, and Δ is the detuning between cavity and injection field.

This equation has an important property: it is linked with a Lyapunov functional $\mathcal{L}$, defined as

$$\frac{\partial X}{\partial t} = -\frac{\delta\mathcal{L}}{\delta X'}, \tag{2.4}$$

that can be minimized in order to find equilibrium states. An analysis of the functional $\mathcal{L}$, and of the corresponding solutions for a real parameter Swift-Hohenberg equation has been performed in [56].

In this section, we show that Eqs. 2.1-2.2 near the critical point associated with optical bistability leads to a nonvariational Swift-Hohenberg equation. To do so, we first reduce the number of parameters. We hence introduce $n \equiv C(Z-1) - 1/2$, $e \equiv E^*/\sqrt{2}$ and $Y \equiv E_I/(2\sqrt{2})$. Equations (2.1) and (2.2) now read

$$\frac{\partial e}{\partial t} = i\theta' e + (1+i\alpha)ne + Y - i\nabla_\perp^2 e, \tag{2.5}$$

$$\frac{\partial n}{\partial t} = \gamma(P - n - (1+2n)|e|^2 + D\nabla_\perp^2 n), \tag{2.6}$$

where $P \equiv C(I-1) - 1/2$, $\gamma \equiv \gamma'/2$, $D = 2d_f$, $\eta' \equiv \xi/2$ and $\theta' \equiv (\theta+\alpha)/2$. The time and space scales are now $(t,\tau) \equiv 2(t',\tau')$ and $\nabla_\perp^2 \equiv 2\nabla_\perp'^2$. We now place

ourselves in the limit of small cavity detuning $\theta' = 0$. The homogeneous steady state (e_s, n_s) is then described by

$$Y = -e_s(1 + i\alpha)\frac{P - |e_s|^2}{1 + 2|e_s|^2}$$

and

$$n_s = \frac{P - |e_s|^2}{1 + 2|e_s|^2}.$$

We restrict our analysis to the nascent bistability regime, close to the critical point where $\partial Y/\partial|e_s| = \partial^2 Y/\partial|e_s|^2 = 0$. The coordinates of this point read as

$$e_c = (1 - i\alpha)\sqrt{3\frac{1 + \alpha^2}{2}},$$

$$n_c = -\frac{3}{2},$$

$$P_c = -\frac{9}{2},$$

$$D_c = \frac{8\alpha}{3 + 3\alpha^2},$$

$$Y_c = \frac{3\sqrt{3 + 3\alpha^2}}{2}.$$

We look for perturbations of the homogeneous steady state that depend on space and time via the slow variables $t \to (1/\gamma + D_c/\alpha)t\epsilon^2$ and $(x, y) \to \sqrt{\epsilon/D_c}(x, y)$, where ϵ is a small parameter. We then expand the variables e, n and the parameters Y, D and P around their critical values as

$$e = e_c(1 + \epsilon f + \epsilon^2 e_2 + \dots),$$

$$n = n_c(1 + \epsilon n_1 + \epsilon^2 n_2 + \dots),$$

$$Y = Y_c(1 - \epsilon^2 p_2/2 + \epsilon^3 y + \dots),$$

$$P = P_c(1 + 3\epsilon^2 p_2 + \dots),$$

$$D = D_c(1 + \epsilon d + \dots).$$

Order ϵ leads to

$$0 = n_1 + f \tag{2.7}$$

$$0 = f + f^* + 2n_1 \tag{2.8}$$

These two conditions bring

$$f \in \mathbb{R} \tag{2.9}$$
$$f = -n_1 \tag{2.10}$$

Order ϵ^2 leads to

$$e_2 + n_2 = -\frac{p_2}{2} + f^2 - \frac{i+\alpha}{4\alpha}\nabla_\perp f, \tag{2.11}$$
$$e_2 + e_2^* + 2n_2 = -3p_2 + 2f^2 - \frac{\nabla_\perp f}{2}. \tag{2.12}$$

This leads to

$$e_2 = -i\frac{\nabla_\perp^2 f}{4\alpha}. \tag{2.13}$$

Further developing at order ϵ^3, we have

$$\begin{aligned} e_3 + n_3 = \frac{\alpha y}{4\alpha} + f\left(\frac{p_2}{2} + \frac{\alpha - i}{4\alpha}\nabla_\perp f\right) - f^3 \\ - \frac{1 - i\alpha}{16\alpha^2}\nabla_\perp^4 f - \frac{2\gamma(1-i\alpha)}{3 + 3\alpha^2 + 8\gamma}\frac{\partial f}{\partial t}, \end{aligned} \tag{2.14}$$

$$\begin{aligned} e_3 + e_3^* + 2n_3 = f\frac{6p_2 + 3\nabla_\perp^2 f}{4} + \frac{3 + 3\alpha^2}{6 + 6\alpha^2 + 16\gamma}\frac{\partial f}{\partial t} \\ - \frac{3f^3}{2} + \frac{\nabla_\perp^2 f^2}{2} - \frac{d\nabla_\perp^2 f}{2} - \frac{\nabla_\perp^4 f}{8}. \end{aligned} \tag{2.15}$$

The solvability condition at this order (this is, the sum of Eq. 2.14, its complex conjugate, and Eq. 2.15) brings the following sclar amplitude equation

$$\frac{\partial f}{\partial t} = y - f\left(p + f^2\right) + \left(d - \frac{5f}{2}\right)\nabla_\perp^2 f - a\nabla_\perp^4 f - 2(\nabla_\perp f)^2, \tag{2.16}$$

where the parameter a is defined as $a \equiv (1-\alpha^2)/(4\alpha^2)$. By using the relation

$$(\nabla_\perp f)^2 = \frac{\nabla_\perp^2 (f^2)}{2} - f\nabla_\perp^2 f, \tag{2.17}$$

one can reformulate Eq. 2.16 in the form

$$\frac{\partial f}{\partial t} = y - f\left(p + f^2\right) + \left(d - \frac{f}{2}\right)\nabla_\perp^2 f - a\nabla_\perp^4 f - \nabla_\perp^2 (f^2), \tag{2.18}$$

that is more suited to numerical simulations.

This equation is physically relevant only if $a > 0$, which implies a very small linewidth enhancement factor $\alpha < 1$. If this condition is not fulfilled, the development needs to be pursued at higher order to ensure a bounded solution to Eq. 2.16. Even though the linewidth enhancement factor of the lasers used in this work are typically around $\alpha \approx 3$-5, we will, for the sake of simplicity, restrict ourselves to this limit in this work. This equation corresponds to the modified Swift-Hohenberg equation used elsewhere [57, 58]. Note that this equation differs from the usual Swift-Hohenberg equation [59, 60]. Indeed, contrarly to the Swift-Hohenberg equation, this equation is nonvariational, because of the term $f\nabla_\perp f$. This term and the square gradient term also break the symmetry $(y, f) \to (-y, -f)$.

2.5 LINEAR STABILITY ANALYSIS OF THE MODIFIED SWIFT-HOHENBERG EQUATION

The homogeneous steady solutions f_s of Eq. 2.16 are given by

$$y = f_s(p + f_s^2). \tag{2.19}$$

If $p < 0$, the electric field f as a function of the input intensity y is bistable with limit points $f_{L\pm} = \pm\sqrt{-p/3}$.

We now consider a linear deviation from the homogeneous steady state of the form $e^{\lambda t + i\mathbf{k}\cdot\mathbf{x}}$, where $\mathbf{x} = (x, y)$ corresponds to the transverse coordinates, the transverse wavevector is $\mathbf{k}$ and the corresponding wavenumber is k. The characteristic equation reads

$$\lambda = -(p + 3f_s^2) - k^2\left(d - \frac{5f_s}{2}\right) - ak^4. \tag{2.20}$$

Turing instabilities occur when two conditions are fulfilled. The first one yields $\frac{\partial\lambda}{\partial k} = 0$. The wavenumber thresholds for a Turing instability hence read

$$k_\pm^2 = \frac{5f_{s\pm} - 2d}{4a}. \tag{2.21}$$

The positiveness of this quantity brings the condition

$$5f_{s\pm} > \frac{2d}{5}. \tag{2.22}$$

The second condition for the occurence of a Turing instability is $\lambda = 0$. When one combines the two conditions, this brings

$$f_{T\pm} = \frac{2}{25 - 48a}\left[5d \pm 2\sqrt{a[12d^2 + p(25 - 48a)]}\right]. \tag{2.23}$$

	$a - 25/48 < 0$	$a - 25/48 > 0$
$p > 0, d > 0$	$]-\infty, f_{T-}]$	$\mathbb{R} - [f_{T+}, f_{T-}]$
$p > 0, d < 0$	$\mathbb{R}$	$\mathbb{R} - [f_{T+}, f_{T-}]$
$p < -12d^2/25, d < 0$	$]-\infty, f_{L-}]$	$\mathbb{R} - [f_{L+}, f_{T-}]$
$-12d^2/25 < p < 0, d < 0$	$]-\infty, f_{T+}]$	$\mathbb{R} - [f_{T+}, f_{T-}]$
$p < -12d^2/25, d > 0$	$]-\infty, f_{L+}] \cup [f_{L-}, f_{T+}]$	$\mathbb{R} - [f_{L+}, f_{T-}]$
$-12d^2/25 < p < 0, d > 0$	$]-\infty, f_{L+}] \cup [f_{T-}, f_{T+}]$	$\mathbb{R} - [f_{T+}, f_{T-}]$

Tab. 2.1: Classification of various stability domains for the steady homogeneous state f_s as a function of dynamical parameters of the modified Swift-Hohenberg equation (2.16)

One can see from this equation that if f_s is sufficiently large, and $48a < 25$, then all homogeneous steady states are unstable.

A classification of the different scenarios leading to Turing instability based on this analysis is presented in Table 2.1. In this table, we classify the different regions in which the system is stable (that is, the regions in which there is no Turing instability) as a function of the values of the parameters a, p, and d.

The analysis of Eq. 2.23 shows that, when $p = p_c = 12d^2/(48a - 25)$, the two instability thresholds coincide at $f_{T\pm} = f_c = -5p_c/(6d)$. At this bifurcation point, the wavenumbers are $k_\pm = k_c = \sqrt{12f_c}5$.

In the case when the two pattern forming instabilities are not close one to another, a theoretical study based on a truncated Fourier analysis has been performed [57]. In this article, the authors have derived a normal form associated with stripes, hexagons 0 and honeycombs (hexagons π) for Eq. 2.16. They performed a relative stability analysis of given patterns with respect to perturbations, favoring formation of other patterns with different symmetries. The results of their analysis have been summed up in the bifurcation diagram presented in Fig. 2.14. As can be seen from this figure, as one increases the intensity of the injected field amplitude, the homogeneous steady state loses stability at y_{T-}, and a branch of hexagons ($H0$) appear. This branch is stable on a wide range of parameters. As the intensity of the injected field is further increased, a region of coexistence between hexagons and stripes is reached. Then, the $H0$ branch becomes unstable, and the only stable solution remaining stable corresponds to the stripes branch. A small region of coexistence between stripes and honeycombs ($H\pi$) is then reached, before the stripes solution loses stability. When the injected field amplitudes becomes y_{T+}, the homogeneous steady state recovers its stability. There are hence domains of coexistence between different kinds of patterns.

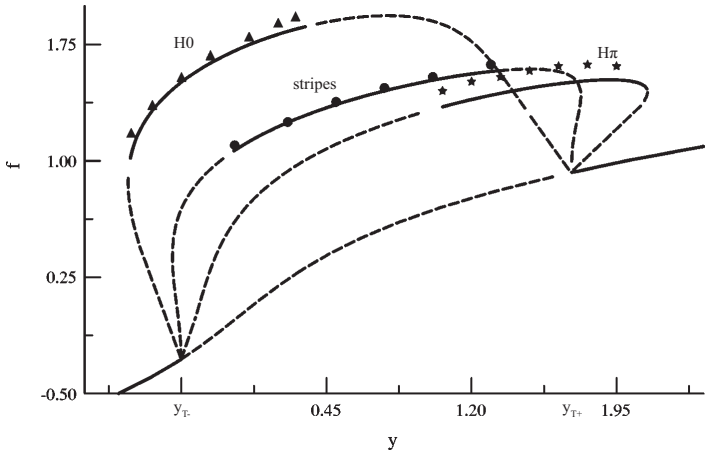

Fig. 2.14: Bifurcation diagram (lines) and numerical simulations (points)for distant instabilities in 2 dimensions for the normal form associated with Eq. 2.16. Only maxima of spatial oscillations are presented here. The H0 branch (Δ) corresponds to hexagons, the middle branch corresponds to stripes ($\bullet$), and the Hπ branch ($\star$) corresponds to honeycombs. Dotted lines correspond to numerically unstable parts. Parameters are $p = 1$, $d = -5$, and $a = 3.75$. Reproduced from [57].

Of particular interest are the regions of coexistence between homogeneous states and patterned states. These regions are the small region of coexistence between homogeneous steady state and $H0$ close to y_{T-}, and the small region of coexistence between the homogeneous steady state and $H\pi$ close to y_{T+}. In these regions, a spatially organized state can coexist with a homogeneous state. This is one of the conditions required for the generation of localized structures. Unfortunately, the normal form procedure does not allow to study these objects [61]. Numerical study of these objects is the subject of the next section.

2.6 LOCALIZED STRUCTURES AND THEIR BIFURCATION SNAKING DIAGRAMS

In the region where localized structures can be drawn (the so-called pinning region), the system exhibits a high degree of multistability. In this region, a homogeneous steady state can coexist with an infinite set of patterns made of an increasing number of localized structures. This phenomenon is called homoclinic snaking. Each complex of localized structures is characterized by either an odd or an even number of peaks. Examples of localized structures having odd and even number or peaks are presented in Fig. 2.15.

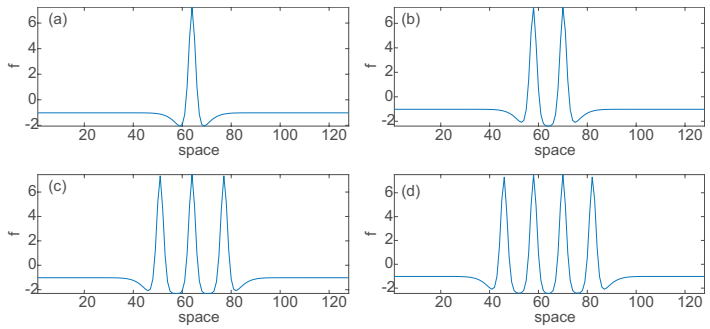

Fig. 2.15: Stationary localized structures formed with one (a), two (b), three (c), and four (d) peaks in the amplitude of the intracavity field. The parameters are $y = -0.35$,$p = -0.7$,$d = -1.2$, and $a = 0.75$.

Since the peak amplitudes of localized patterns comprising different numbers of solitons are close to each other,it is convenient to plot the "L2 norm" defined by the relation $W = \int dx|f - f_s|^2$ instead of the peak amplitudes. A typical bifurcation diagram, illustrating the dependence of W on the input field amplitude y, is shown in Fig. 2.16. It consists of two snaking curves: one corresponding to localized patterns

with an odd number of peaks and the other to patterns with an even number of peaks. The two interweaved snaking curves emerge from the Turing instability point located at $f = f_{T+}$. For each curve, as W increases, at every turning point where the slope becomes infinite, a pair of additional peaks appears in the pattern.

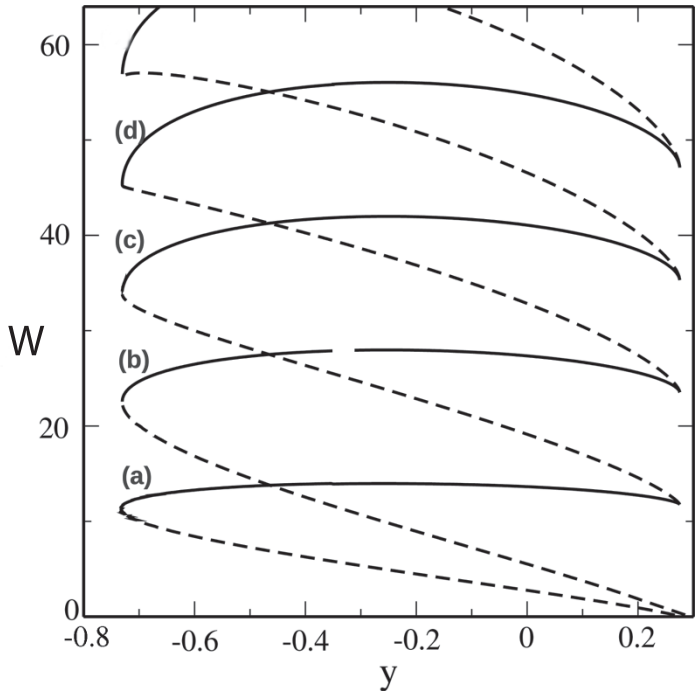

Fig. 2.16: Snaking bifurcation diagram of Eq. 2.16 showing two interweaved snaking curves: the branches (a)–(d) correspond to one through four localized structures, respectively (see Fig. 2.15). The full and the broken lines correspond to stable and unstable localized branches of solutions, respectively. The parameters are $p = -0.7$,$d = -1.2$, and $a = 0.75$. Reproduced from [62].

2.7 CONCLUSIONS

In this chapter, we have built an experimental setup, and we have investigated the formation of two-dimensional localized structures in the transverse section of a 80μm diameter VCSEL. Bistability corresponding to spontaneous appearance and disappearing of a localized structure have been observed, as a function of optical injection

power, and as a function of VCSEL current. Oscillating tails of the localized structures have also been observed. Spontaneous appearance and disappearance of two localized structures have also been observed, which is a manifestation of multistability.

All of these measurements have been performed while the linearly polarized optical injection had its direction matching the one in which the VCSEL spontaneously lases in while being pumped close to its current threshold.

Considering a model for the specific case of a VCSEL injection-locked in polarization and frequency in the vicinity of the nascent bistability, we provided nonlinear perturbative analysis and obtained a modified Swift-Hohenberg equation. Based on this equation, we showed that, in one transverse dimension, stationary-cavity solitons exhibited a clustering behavior in the pinning range of parameters where spatially homogeneous and periodic solutions were both linearly stable. In this range, we constructed a snaking bifurcation diagram associated with localized structures having an odd, or an even number of peaks.

3

VECTOR LOCALIZED STRUCTURES IN BROAD AREA VCSELS

Polarization is a fundamental property of light that has been neglected in the previous chapter. We could do so, because the polarization degree of freedom was taken away by the optical injection (polarization locking). This is a reasonible assumption, as the VCSEL was electrically pumped close to its lasing threshold (where its linear polarization direction is vertical), and the optical injection linear polarization was vertical. However, if we now consider a relatively large angle between the optical injection linear polarization direction and the linear polarization direction of the VCSEL, we cannot assume that the dynamics of the electric field will be limited to this particular linear polarization direction.

In this chapter, we first experimentally characterize the polarization state of localized structures when they are generated using a linearly polarized optical injection. The polarization direction is varied in a 90° span. These measurements show that the localized structure polarization is not exactly the one of the optical injection. In fact, the polarization state of the so-generated localized structures is not linear, as it acquires distinct ellipticity. In the second part of this chapter, we use the spin-flip VCSEL model derived in chapter 2 to study such vector localized structures. The localized structures numerically generated using this model present an ellipticity comparable to the one from the experimental results, and carry out detailed mapping of the steady states and their stability in the plane of injection strength-frequency detuning between optical injection and VCSEL.

3.1 EXPERIMENTAL OBSERVATION OF VECTOR LOCALIZED STRUCTURES

To study the polarization properties of localized structures in VCSELs, it is necessary to modify the experimental setup described in chapter 2. In this section, we describe the modifications made to that setup. Next, we present experimental observation of vector localized structures, alongside with their polarization properties, described in terms of their Stokes parameters.

We first describe the experimental setup. Then we describe the results obtained with it.

3.1.1 *Experimental setup for investigation of polarization properties of localized structures in VCSELs*

A scheme of the experimental setup for investigation of polarization properties of localized structures in VCSELs is presented in Fig. 3.1. There are two main differences with the scheme presented in Fig. 2.2: first, the variable optical density filter from the former setup has been replaced by a combination of a half-wave plate and a polarizer. This allows the polarization state of the injected light to be kept well linearly polarized. Second, another analysis branch has been placed. It consists of an

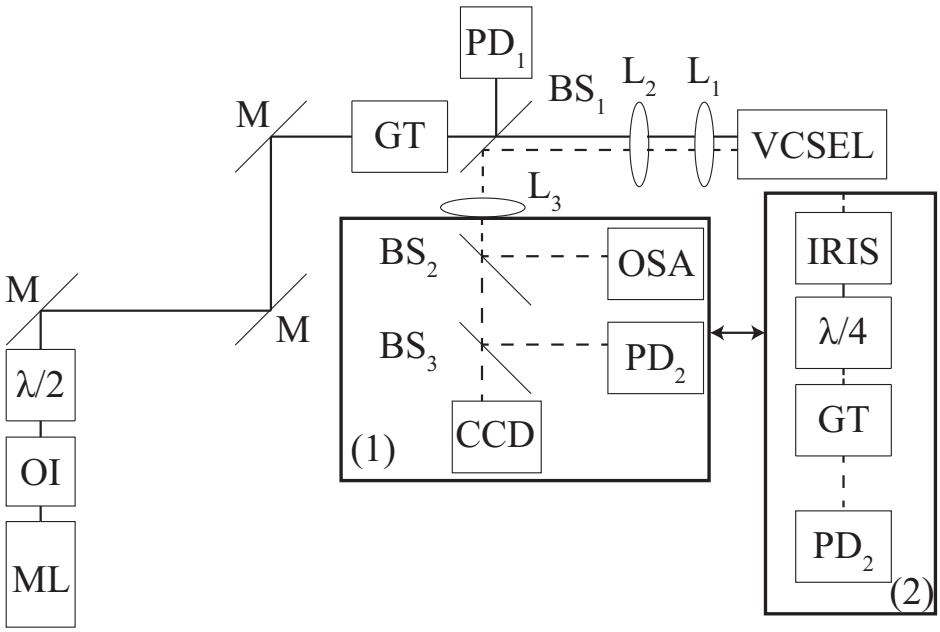

Fig. 3.1: Experimental setup schematic. The full line is the path of the light from the master laser, whereas the dashed line is the path followed by the light from the VCSEL. The analysis branch (1) is used for general localized structure characterization, whereas the analysis branch (2) is used for determination of polarization properties of localized structures. ML: master laser, OI: optical isolator, $\lambda/2$: half wave plate, M: mirror, GT: Glan Thompson prism, PD: photodiode, OSA: optical spectrum analyser,$\lambda/4$: quarter wave-plate.

iris (to isolate the localized structure from the background), a quarter-wave plate, a polarizer and a photodiode. These three elements allow to measure the polarization state of the localized structure, using the method described in [63].

To measure the Stokes parameters, we perform 6 measurements, for different orientations of the quarter-wave plate and the polarizer. The intensities measured at the photodiode PD_2 for measurement of the Stokes parameters are $I_{0,0}$, $I_{45,45}$, $I_{90,90}$, $I_{135,135}$, $I_{0,45}$, and $I_{0,135}$, where $I_{\alpha,\beta}$ is a measurement that has been performed while the quarter-wave plate makes an angle α with horizontal, and the polarizer makes an angle β with horizontal. These quantities are related to the Stokes parameters by

$$S_0 = I_{0,0} + I_{90,90}, \tag{3.1}$$
$$S_1 = I_{0,0} - I_{90,90}, \tag{3.2}$$
$$S_2 = I_{45,45} - I_{135,135}, \tag{3.3}$$
$$S_3 = I_{0,45} - I_{0,135}. \tag{3.4}$$

These quantities can be related to the projections of the electric field on its linear components E_x and E_y by the relations

$$S_0 = |E_x|^2 + |E_y|^2, \tag{3.5}$$
$$S_1 = |E_x|^2 - |E_y|^2, \tag{3.6}$$
$$S_2 = E_x^* E_y + E_x E_y^*, \tag{3.7}$$
$$S_3 = i(E_x^* E_y - E_x E_y^*). \tag{3.8}$$

The parameter S_0 represents the total intensity of the electromagnetic wave. The positive part of S_1 accounts for the amount of light linearly polarized in the horizontal direction, its negative part holds for the vertically polarized component.

S_1, S_2 and S_3 provide the amount of light polarized, respectively, along x and y axes, at 45 degrees with respect to the x and y axes, and left and right circularly polarized.

S_1, S_2, and S_3 are sometimes normalized. To distinguish between these two conventions, we use capital letters for the Stokes parameters, and small font letters for normalized quantities: $s_i = S_i/S_0$, for $i \in [1:3]$.

3.1.2 *Experimental observation of vector localized structures in VCSELs*

In this section, we use the experimental setup described in Sec. 3.1.1. The experimental procedure reads as follows: first, we choose a linear polarization direction for the optical injection. Then, we repeat the procedure described in Sec. 2.2.2, in order to prove that the considered region of the transverse plane of the VCSEL is indeed a localized structure. An example thereof, for an optical injection linear polarization making an angle of -30° with horizontal, is presented in Fig. 3.2.

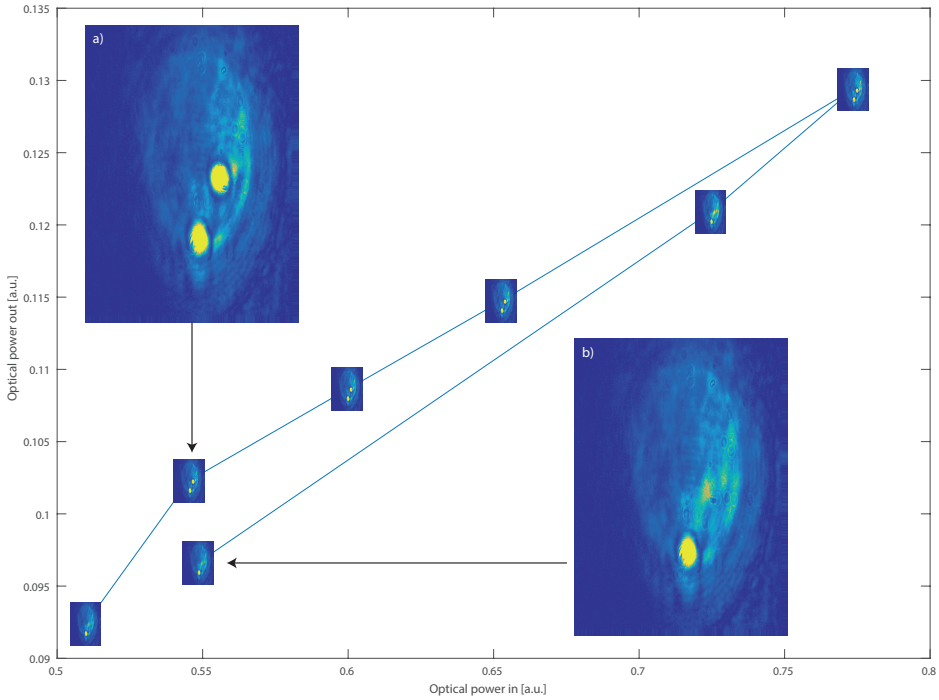

Fig. 3.2: Bistability curve, i.e. the VCSEL output power as a function of injection power obtained for an optical injection polarized in the direction of the one of the free-running VCSEL. The wavelength of the optical injection is $\lambda_M = 983.35$nm. The inset a) (resp. b)) represents the near field profile on the upper (resp. lower) branch of the hysteresis. These results have been obtained with the VCSEL kept at 25.00°C with an injection current of 45.0 mA. Each measurement has been marked with the corresponding near field profile.

Once the bistable character of the localized structure has been proven, the optical injection power is set quite strong, such as the system will stay on the higher branch of the hysteresis. Then, the analysis branch (1) in Fig. 3.1 is replaced by the analysis branch (2). We then use the iris to isolate the localized structure from the rest of the VCSEL radiation, before measuring the localized structure's Stokes parameters. This experiment is then repeated for various directions of the optical injection linear polarization.

Results of these measurements are presented in Fig. 3.3. This figure presents the Stokes parameters $s_{1,2,3}$, normalized over the localized structure total power S_0, as a function of the optical injection linear polarization direction with respect to horizontal, Ψ. The angle θ between the horizontal and the direction of the main axis of the localized structure polarization ellipse is also depicted in that figure.

The Stokes parameters s_1 and s_2 provide insight into the proportion of localized structure power that is linearly polarized. s_3 describes the amount of light that is circularly polarized. The circular component of the localized structure power does not come from the optical injection. Indeed, when the s_3 component is at a maximum, at 20°, a measurement of the optical injection Stokes parameters brings a measurement of $s_{3OI} = -0.00627$. This value is twenty times smaller than the one of corresponding localized structure $s_3 = 0.22$. The ellipticity of the localized structure hence cannot be attributed to the one of the optical injection, but is inherent to the optically injected VCSEL. We will theoretically investigate these effects in the next section.

3.2 THEORETICAL DESCRIPTION OF VECTOR LOCALIZED STRUCTURES

To describe the previous experimental results, we first describe the evolution of light in a free-running VCSEL, taking into account the polarization dynamics. Then, we add an optical injection in this description, before taking the assumption that the dynamics all take place in a single linear polarization direction.

To derive the equations governing the evolution in time and space of the electric field inside such a structure, we will start from the very general Maxwell-Bloch equations (as in [42]), written for the convention $\mathbf{F} \equiv [F_x(x,y,t)\mathbf{u_x} + F_y(x,y,t)\mathbf{u_y}]e^{i(\mathbf{k}\cdot\mathbf{z}-\nu t)} + c.c.$. In this expression, $F_x(x,y,t)$ and $F_y(x,y,t)$ are the slowly varying field amplitudes of the fields polarized in the x and y directions, respectively. $\mathbf{u}_x$ and $\mathbf{u}_y$ are unitary vectors along these directions. $\mathbf{k}$ and ν are the wavevector and frequency of the electric field.

One considers the four-level model in Fig. 3.4: charge carriers are either of positive or negative spin projection. Due to spin conservation and depending on the

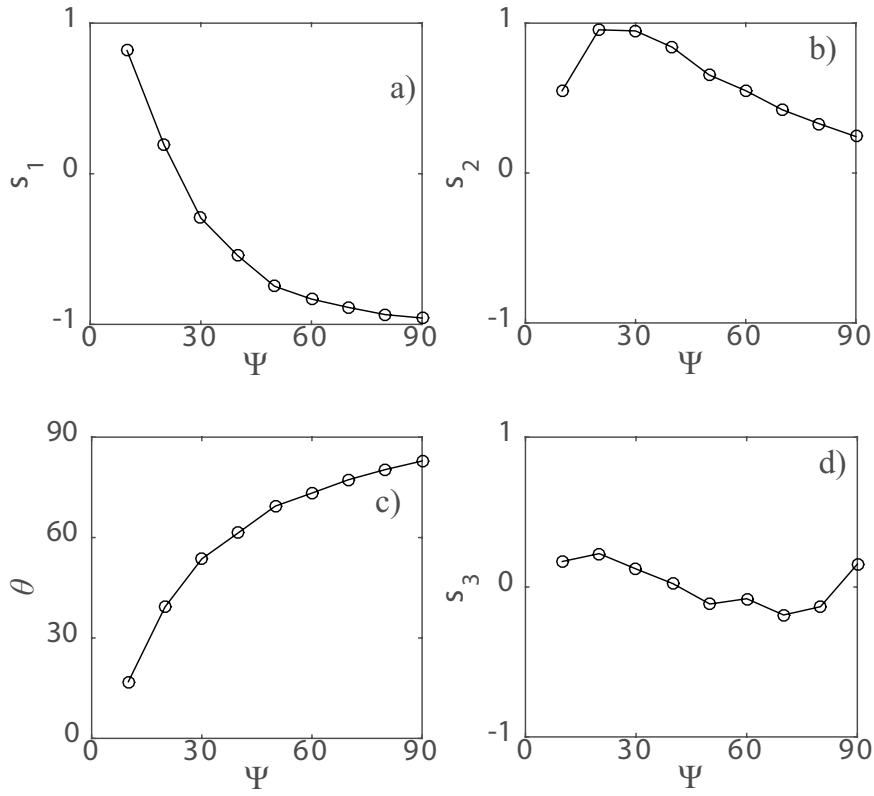

Fig. 3.3: Stokes parameters of a localized structure as a function of optical injection linear polarization angle with horizontal Ψ. a): s_1. b): s_2. c):angle between main axis of the polarization ellipse and horizontal θ.d): s_3. VCSEL is kept at 25.00°C, injection current is 45.0 mA and optical injection wavelength is kept at 983.3 nm.

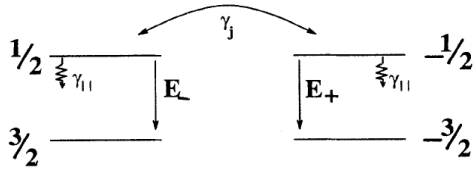

Fig. 3.4: Four level model for quantum well VCSELs. The energy levels i describe carriers of spin i. As the transition of a carrier happens, a photon of left (resp. right) circular polarization is emitted, contributing to the electric field $\mathbf{E}_+$ (resp. $\mathbf{E}_-$). Exchange rate between different spin sign populations is denoted γ_j.

sign of their spin, their decay from level $+(-)3/2$ to level $+(-)1/2$ will result in the generation of a right (left) circularly polarized light. We define the quantities

$$D = \frac{n_1 + n_{-1} - (n_3 + n_{-3})}{2}, \tag{3.9}$$

$$d = \frac{n_{-1} - n_{-3} - (n_1 - n_3)}{2}, \tag{3.10}$$

where population of carriers having a spin $i/2$ is denoted n_i. that way, D is the average population inversion, whereas d is the difference between the negative and positive spin population inversions. In the mean-field, slowly-varying envelope, and paraxial approximations, the model describing the spatio-temporal evolution of the fields $F_\pm$, $P_\pm$, and of the populations D and d read [42]:

$$\frac{\partial F_\pm}{\partial t} = -\kappa F_\pm - i\nu F_\pm - ig_0^* P_\pm + i\frac{c^2}{2\nu}\nabla_\perp^2 F_\pm, \tag{3.11}$$

$$\frac{\partial P_\pm}{\partial t} = -[\gamma_\perp + i(\omega - \nu)]P_\pm + ig_0 F_\pm (D \pm d), \tag{3.12}$$

$$\frac{\partial D}{\partial t} = -\gamma_\parallel (D - \sigma) + [ig_0^*(F_+^* P_+ + F_-^* P_-) + c.c.] + D_f \nabla_\perp^2 D, \tag{3.13}$$

$$\frac{\partial d}{\partial t} = -\gamma_j d + [ig_0^*(F_+^* P_+ - F_-^* P_-) + c.c.] + D_f \nabla_\perp^2 d. \tag{3.14}$$

In these equations, g_0 is the coupling constant between the slowly varying amplitudes of the right and left circularly polarized elements of the electric field $F_\pm$ and the corresponding matter polarization slowly varying envelope $P_\pm$. κ is the inverse photon lifetime in the cavity. The frequency associated with the transitions depicted in Fig. 3.4 is ω. The transverse Laplacian $\nabla_\perp^2$ in the electric field equation accounts for diffraction, whereas the one in the population equations accounts for diffusion of

the carriers; it acts in the plane transverse to the propagation of light. $\gamma_\perp$ is the relaxation rate for polarization. σ is the pumping rate associated with current injection. D_f is the diffusion coefficient for carriers. c is the speed of light. $\gamma_\parallel$ is the relaxation rate for carriers and γ_j is the spin exchange rate.

As the dipole decay rate is much faster than the other timescales involved in these equations, one can adiabatically eliminate polarization. This leads to

$$P_\pm = \frac{g_0(i\gamma_\perp + \omega - \nu)}{\gamma_\perp^2 + (\omega-\nu)^2} F_\pm (D \pm d) \tag{3.15}$$

and

$$\begin{aligned}\frac{\partial F_\pm}{\partial t} &= -(\kappa + i\nu)F_\pm + \frac{|g_0|^2[\gamma_\perp - i(\omega-\nu)]F_\pm(D\pm d)}{\gamma_\perp^2 + (\omega-\nu)^2} \\ &\quad + i\frac{c^2}{2\nu}\nabla_\perp^2 F_\pm\end{aligned} \tag{3.16}$$

$$\begin{aligned}\frac{\partial D}{\partial t} &= -\gamma_\parallel(D-\sigma) + D_f\nabla_\perp^2 D \\ &\quad - \frac{2\gamma_\perp|g_0|^2[|F_+|^2(D+d) + |F_-|^2(D-d)]}{\gamma_\perp^2 + (\omega-\nu)^2},\end{aligned} \tag{3.17}$$

$$\begin{aligned}\frac{\partial d}{\partial t} &= -\gamma_j d + D_f\nabla_\perp^2 d \\ &\quad - \frac{2\gamma_\perp|g_0|^2[|F_+|^2(D+d) - |F_-|^2(D-d)]}{\gamma_\perp^2 + (\omega-\nu)^2}.\end{aligned} \tag{3.18}$$

The rescaling is now performed as follows:

$$E_\pm \equiv \sqrt{\frac{2\gamma_\perp|g_0|^2}{\gamma_\parallel[\gamma_\perp^2 + (\omega-\nu)^2]}} F_\pm,$$

$$(N,n) \equiv \frac{\gamma_\perp|g_0|^2(D,d)}{\kappa(\gamma_\perp^2 + (\omega-\nu)^2)},$$

$$\alpha \equiv \frac{\omega-\nu}{\gamma_\perp},$$

$$\mu \equiv \frac{|g_0|^2\gamma_\perp\sigma}{\kappa[\gamma_\perp^2 + (\omega-\nu)^2]}.$$

After some algebra, Eqs. 3.16-3.18 become

$$\frac{\partial E_\pm}{\partial t} = -(\kappa + i\nu)E_\pm + \kappa(1 - i\alpha)E_\pm(N \pm n) + i\frac{c^2}{2\nu}\nabla_\perp^2 E_\pm, \tag{3.19}$$

$$\frac{\partial N}{\partial t} = -\gamma_\parallel[N - \mu + |E_+|^2(N + n) + |E_-|^2(N - n)] + D_f\nabla_\perp^2 N, \tag{3.20}$$

$$\frac{\partial n}{\partial t} = -\gamma_j n - \gamma_\parallel[|E_+|^2(N + n) - |E_-|^2(N - n)] + D_f\nabla_\perp^2 n. \tag{3.21}$$

In these equations, the different field polarizations are only coupled through the population equations. To account for the unavoidable birefringence effects, one phenomenologically introduces the two constants γ_a, the amplitude anisotropy, and γ_p, the phase anisotropy [64]:

$$\begin{aligned}\frac{\partial E_\pm}{\partial t} &= -(\kappa + i\nu)E_\pm + \kappa(1 - i\alpha)E_\pm(N \pm n) \\ &\quad + i\frac{c^2}{2\nu}\nabla_\perp^2 E_\pm - \gamma_a E_\mp - i\gamma_p E_\mp,\end{aligned} \tag{3.22}$$

$$\frac{\partial N}{\partial t} = -\gamma_\parallel[N - \mu + |E_+|^2(N + n) + |E_-|^2(N - n)] + D_f\nabla_\perp^2 N, \tag{3.23}$$

$$\frac{\partial n}{\partial t} = -\gamma_j n - \gamma_\parallel[|E_+|^2(N + n) - |E_-|^2(N - n)] + D_f\nabla_\perp^2 n. \tag{3.24}$$

To have a zero frequency when the VCSEL is at the lasing threshold current [64], we now set $\nu = \kappa\alpha$. This leads to

$$\begin{aligned}\frac{\partial E_\pm}{\partial t} &= \kappa(1 - i\alpha)(N \pm n - 1)E_\pm + i\frac{c^2}{2\kappa\alpha}\nabla_\perp^2 E_\pm \\ &\quad - \gamma_a E_\mp - i\gamma_p E_\mp,\end{aligned} \tag{3.25}$$

$$\begin{aligned}\frac{\partial N}{\partial t} &= -\gamma_\parallel\left[N(1 + |E_+|^2 + |E_-|^2) - \mu + n(|E_+|^2 - |E_-|^2)\right] \\ &\quad + D_f\nabla_\perp^2 N,\end{aligned} \tag{3.26}$$

$$\begin{aligned}\frac{\partial n}{\partial t} &= -\gamma_j n + D_f\nabla_\perp^2 n \\ &\quad - \gamma_\parallel\left[n(|E_+|^2 + |E_-|^2) + N(|E_+|^2 - |E_-|^2)\right].\end{aligned} \tag{3.27}$$

As the optical injection we plan to add in this model is linearly polarized, it makes sense to rewrite Eqs. 3.25-3.27 in their (x, y) components:

$$\begin{aligned}\frac{\partial E_x}{\partial t} &= -(\kappa+\gamma_a)E_x + i(\kappa\alpha-\gamma_p)E_x \\ &\quad + \kappa(1-i\alpha)(NE_x + inE_y) + \frac{ic^2}{2\kappa\alpha}\nabla_\perp^2 E_x,\end{aligned} \tag{3.28}$$

$$\begin{aligned}\frac{\partial E_y}{\partial t} &= -(\kappa-\gamma_a)E_y + i(\kappa\alpha+\gamma_p)E_y \\ &\quad + \kappa(1-i\alpha)(NE_y - inE_x) + \frac{ic^2}{2\kappa\alpha}\nabla_\perp^2 E_y,\end{aligned} \tag{3.29}$$

$$\begin{aligned}\frac{\partial N}{\partial t} &= -\gamma_\parallel\left[N(1+|E_x|^2+|E_y|^2) - \mu + 2n\Im(E_xE_y^*)\right] \\ &\quad + D_f\nabla_\perp^2 N,\end{aligned} \tag{3.30}$$

$$\frac{\partial n}{\partial t} = -\gamma_j n + D_f\nabla_\perp^2 n - \gamma_\parallel\left[n(|E_x|^2+|E_y|^2) + 2N\Im(E_xE_y^*)\right]. \tag{3.31}$$

3.2.1 *VCSEL under linearly polarized optical injection*

We now add optical injection in the equations for the electric field. The detuning between the resonator frequency and the optical injection frequency is depicted as $\Delta\omega$, the injection power is denoted κE_I and its linear polarization direction is described by Ψ, the angle between horizontal and the linear polarization direction. One gets then

$$\begin{aligned}\frac{\partial E_x}{\partial t} &= -(\kappa+\gamma_a)E_x + i(\kappa\alpha-\gamma_p+\Delta\omega)E_x \\ &\quad + \kappa(1-i\alpha)(NE_x + inE_y) + i\frac{c^2}{2\kappa\alpha}\nabla_\perp^2 E_x + \kappa E_I\cos(\Psi),\end{aligned} \tag{3.32}$$

$$\begin{aligned}\frac{\partial E_y}{\partial t} &= -(\kappa-\gamma_a)E_y + i(\kappa\alpha+\gamma_p+\Delta\omega)E_y \\ &\quad + \kappa(1-i\alpha)(NE_y - inE_x) + i\frac{c^2}{2\kappa\alpha}\nabla_\perp^2 E_y + \kappa E_I\sin(\Psi),\end{aligned} \tag{3.33}$$

$$\begin{aligned}\frac{\partial N}{\partial t} &= -\gamma_\parallel\left[N(1+|E_x|^2+|E_y|^2) - \mu + 2n\Im(E_xE_y^*)\right] \\ &\quad + D_f\nabla_\perp^2 N,\end{aligned} \tag{3.34}$$

$$\frac{\partial n}{\partial t} = -\gamma_j n + D_f\nabla_\perp^2 n - \gamma_\parallel\left[n(|E_x|^2+|E_y|^2) + 2N\Im(E_xE_y^*)\right]. \tag{3.35}$$

In the case when the linear polarization of the optical injection has an arbitrary direction, we will neglect diffusion of the carriers D_f. It brings, defining $a \equiv \frac{c^2}{2\kappa\alpha}$

$$\begin{aligned}\frac{\partial E_x}{\partial t} &= -(\kappa+\gamma_a)E_x + i(\kappa\alpha - \gamma_p + \Delta\omega)E_x \\ &\quad + \kappa(1-i\alpha)(NE_x + inE_y) + ia\nabla_\perp^2 E_x + \kappa E_I\cos(\Psi),\end{aligned} \tag{3.36}$$

$$\begin{aligned}\frac{\partial E_y}{\partial t} &= -(\kappa-\gamma_a)E_y + i(\kappa\alpha + \gamma_p + \Delta\omega)E_y \\ &\quad + \kappa(1-i\alpha)(NE_y - inE_x) + ia\nabla_\perp^2 E_y + \kappa E_I\sin(\Psi),\end{aligned} \tag{3.37}$$

$$\frac{\partial N}{\partial t} = -\gamma_\parallel\left[N(1+|E_x|^2+|E_y|^2) - \mu + 2n\Im(E_xE_y^*)\right] \tag{3.38}$$

$$\frac{\partial n}{\partial t} = -\gamma_j n - \gamma_\parallel\left[n(|E_x|^2+|E_y|^2) + 2N\Im(E_xE_y^*)\right]. \tag{3.39}$$

We will in the continuation of this work refer to this equation system (Eqs.3.36-3.39) as the VCSEL spin-flip model. This model notably features two main timescales, given by the photon lifetime κ (hundreds of ns^{-1}) and the carrier lifetime $\gamma_\parallel$ (some ns$^-1$). The control parameters are μ, the injection current, E_I, the optical injection power, Ψ, its linear polarization angle with horizontal, and $\Delta\omega$, the frequency difference between optical injection and cavity.

3.2.2 *Link between the spin-flip and the scalar VCSEL mean field models*

The model described in the previous chapter can be derived from the Eqs. 3.36-3.39. If we now assume that the VCSEL is locked in both frequency and polarization to the linearly polarized optical injection, then there is no need for two field envelope variables. In that case, the VCSEL does not emit light in the orthogonal polarization, and Eqs. 3.36-3.39 can be simplified, taking $E_y = \Psi = n = 0$. They then reduce to

$$\begin{aligned}\frac{\partial E}{\partial t} &= -(\kappa+\gamma_a)E + i(\kappa\alpha - \gamma_p + \Delta\omega)E \\ &\quad + \kappa(1-i\alpha)NE + i\frac{c^2}{2\kappa\alpha}\nabla_\perp^2 E + \kappa E_I,\end{aligned} \tag{3.40}$$

$$\frac{\partial N}{\partial t} = -\gamma_\parallel\left[N(1+|E|^2) - \mu\right] + D_f\nabla_\perp^2 N, \tag{3.41}$$

In these equations, E_x has been replaced by E, as it is the only component of the electric field to survive. One can now scale time to the photon lifetime $t' \equiv \kappa t$:

$$\begin{aligned}\frac{\partial E}{\partial t'} &= -(1+\frac{\gamma_a}{\kappa})E + i(\alpha - \frac{\gamma_p - \Delta\omega}{\kappa})E \\ &\quad + (1-i\alpha)NE + i\frac{c^2}{2\kappa^2\alpha}\nabla_\perp^2 E + E_I,\end{aligned} \tag{3.42}$$

$$\frac{\partial N}{\partial t'} = -\frac{\gamma_\parallel}{\kappa}\left[N(1+|E|^2) - \mu\right] + \frac{D_f}{\kappa}\nabla_\perp^2 N, \tag{3.43}$$

The population inversion and space can be rescaled too, using

$$Z \equiv \frac{N}{2C} + 1,$$

$$\nabla_\perp^2 \equiv \frac{2\kappa^2\alpha}{c^2}\nabla_\perp'^2.$$

That brings

$$\begin{aligned}\frac{\partial E}{\partial t'} &= -\left[1 + \frac{\gamma_a}{\kappa} + i\left(-\alpha + \frac{\gamma_p - \Delta\omega}{\kappa}\right)\right]E \\ &\quad + (1-i\alpha)2C(Z-1)E + i\nabla_\perp'^2 E + E_I,\end{aligned} \tag{3.44}$$

$$\frac{\partial Z}{\partial t'} = -\frac{\gamma_\parallel}{\kappa}\left[(Z-1)(1+|E|^2) - \frac{\mu}{2C}\right] + \frac{2D_f\kappa\alpha}{c^2}\nabla_\perp'^2 Z, \tag{3.45}$$

We now use, to describe the equivalent diffusion of the carriers d_f, cavity losses η, cavity detuning θ, carrier decay rate γ and current injection I the following conventions:

$$d_f \equiv \frac{2D_f\kappa^2\alpha}{c^2\gamma_\parallel},$$

$$\eta \equiv \frac{\gamma_a}{\kappa},$$

$$\theta \equiv \frac{\gamma_p - \Delta\omega}{\kappa},$$

$$\gamma \equiv \frac{\gamma_\parallel}{\kappa},$$

$$I \equiv \frac{\mu}{2C} + 1.$$

Replacing these quantities in Eqs. 3.44 and 3.45, we recover the VCSEL scalar mean field model described in [23] given in Eqs. 2.1-2.2:

$$\frac{\partial E}{\partial t'} = -(1+\eta+i\theta)E + 2C(1-i\alpha)(Z-1)E + i\nabla_\perp'^2 E + E_I, \quad (3.46)$$

$$\frac{\partial Z}{\partial t'} = -\gamma\left[Z - I + |E|^2(Z-1) - d_f\nabla_\perp'^2 Z\right]. \quad (3.47)$$

These equations have been discussed in chapter 2

3.3 HOMOGENEOUS STEADY STATES OF THE VCSEL SPIN-FLIP MODEL AND THEIR LINEAR STABILITY

In order to find localized structures in the VCSEL spin flip model described by Eqs. 3.36-3.39, we first investigate the homogeneous steady states of these equations, defined by $\partial X_0/\partial t = \nabla_\perp^2 X_0 = 0$, where X stands for the electric field envelopes $E_{x,y}$, and the populations D and d.

The homogeneous steady states of Eqs. 3.36-3.39 yield:

$$\begin{aligned} 0 &= -(\kappa+\gamma_a)E_{x0} + i(\kappa\alpha - \gamma_p + \Delta\omega)E_{x0} \\ &\quad + \kappa(1-i\alpha)(N_0E_{x0} + in_0E_{y0}) + \kappa E_I\cos(\Psi), \end{aligned} \quad (3.48)$$

$$\begin{aligned} 0 &= -(\kappa-\gamma_a)E_{y0} + i(\kappa\alpha + \gamma_p + \Delta\omega)E_{y0} \\ &\quad + \kappa(1-i\alpha)(N_0E_{y0} - in_0E_{x0}) + \kappa E_I\sin(\Psi), \end{aligned} \quad (3.49)$$

$$0 = N_0(1+|E_{x0}|^2+|E_{y0}|^2) - \mu + 2n_0\Im(E_{x0}E_{y0}^*), \quad (3.50)$$

$$0 = \gamma_j n_0 + \gamma_\parallel\left[n_0(|E_{x0}|^2+|E_{y0}|^2) + 2N_0\Im(E_{x0}E_{y0}^*)\right]. \quad (3.51)$$

Defining $E_x = X + iY$, and $E_y = W + iV$, the characteristic matrix reads

$$\begin{pmatrix} P & A & \kappa n_0\alpha & -\kappa n_0 & \kappa(X_0+\alpha Y_0) & -\kappa(V_0-\alpha W_0) \\ -A & P & \kappa n_0 & \kappa n_0\alpha & \kappa(-\alpha X_0+Y_0) & \kappa(W_0+\alpha V_0) \\ -\kappa n_0\alpha & \kappa n_0 & P & C & \kappa(W_0+\alpha V_0) & \kappa(Y_0-\alpha X_0) \\ -\kappa n_0 & -\kappa n_0\alpha & -C & P & \kappa(V_0-\alpha W_0) & \kappa(-X_0-\alpha Y_0) \\ D & G & J & L & B & -2\gamma_\parallel(Y_0W_0-V_0X_0) \\ F & H & K & M & -2\gamma_\parallel(Y_0W_0-V_0X_0) & Q \end{pmatrix},$$

with $A = -\kappa\alpha + \gamma_p - \Delta\omega + ak^2 + \kappa N_0\alpha$, $B = -[\gamma_\parallel(1+X_0^2+Y_0^2+W_0^2+V_0^2)+\lambda]$, $C = -\kappa\alpha - \gamma_p - \Delta\omega + \kappa\alpha N_0 + ak^2$, $D = -2\gamma_\parallel(N_0X_0 - n_0V_0)$, $F = -2\gamma_\parallel(n_0X_0 - N_0V_0)$, $G = -2\gamma_\parallel(N_0Y_0 + n_0W_0)$, $H = -2\gamma_\parallel(n_0Y_0 + N_0W_0)$, $J = -2\gamma_\parallel(N_0W_0 +$

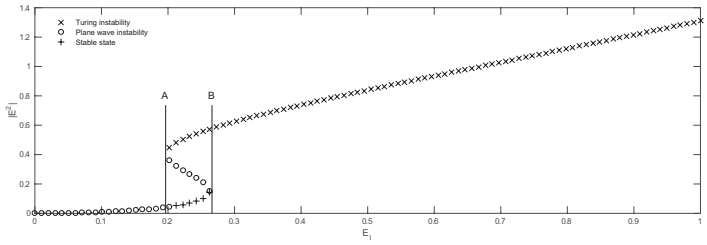

Fig. 3.5: Homogeneous steady states for $|E|^2$ as a function of optical injection power E_I for the model (3.36)-(3.39). Stable states (plus signs), plane wave unstable states (circles) and Turing unstable states (crosses). The spin-flip model parameters are $\kappa = 200$ ns^{-1}, $\gamma_a = 1$, $\alpha = 3$, $\gamma_p = -20$ ns^{-1}, $\Delta\omega = 200$ ns^{-1}, $a = 1$, $\gamma_{\parallel} = 1$ ns^{-1}, $\mu = 1.05$, $\gamma_j = 50$ ns^{-1}, $\Psi = 0.5$ rad. A and B lines represent the limits of the bistable region.

$n_0Y_0)$, $K = -2\gamma_{\parallel}(n_0W_0 + N_0Y_0)$, $L = -2\gamma_{\parallel}(N_0V_0 - n_0X_0)$, $M = -2\gamma_{\parallel}(n_0V_0 - N_0X_0)$, $P = -(\kappa + \gamma_a - \kappa N_0 + \lambda)$, and $Q = -[\gamma_j + \gamma_{\parallel}(X_0^2 + Y_0^2 + W_0^2 + V_0^2) + \lambda]$.

Linear stability analysis of Eqs. 3.36-3.39 is performed in two ways: first, we describe the evolution of the stability of the system for all values of the parameters fixed, apart from the injection strength E_I. In a second stage, we investigate the evolution of the stability of the system when two parameters are varied: the injection strength E_I, and the detuning between the injection field and the VCSEL frequency $\Delta\omega$.

In Fig. 3.5, the homogeneous steady states of the system are presented, as a function of optical injection power E_I, as well as their stability properties, computed from the characteristic matrix. In this figure, $\times$ denote Turing unstable states, $\circ$ represent plane wave unstable states, and $+$ stand for stable states. For low injection strength values, the system is unstable. As the injection strength E_I is increased, when the line A is met, another state, that is Turing unstable, begins to coexist with this unstable state. Soon after, as one further increases the intensity of the optical injection, the first state becomes stable, while it still coexists with the turing unstable state. As the optical injection is further increased, when the line B is met, the lower energy state ceases to exist, leaving the upper energy Turing unstable state as the only possible state of the system.

In Fig. 3.6, a mapping of the stability of the system in the vicinity of the parameters of Fig. 3.5 is presented. In this figure, the different stability scenarios are presented as color codes. It is worth remarking that unstable steady states located in the middle of S-shaped hysteresis curves are not considered here.

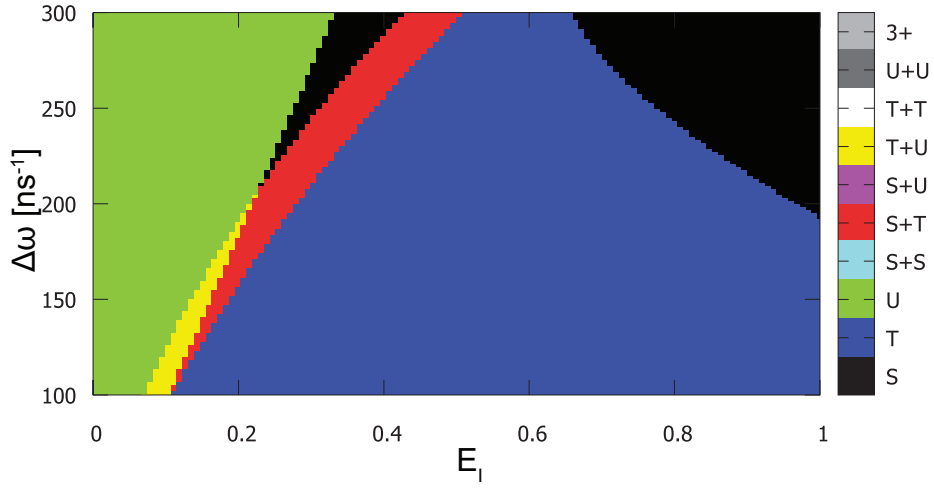

Fig. 3.6: Mapping of spin-flip VCSEL model homogeneous solution and their stability in the plane of injection strength E_I-frequency detuning between optical injection and VCSEL cavity $\Delta\omega$. Green, blue and black denote the presence of a single unstable, Turing unstable, and stable state, respectively. Yellow (red) denote the coexistence of a Turing unstable state with an unstable (stable) state. Apart from $\Delta\omega$, parameters are the same as in Fig. 3.5.

One notices that for low optical injection power E_I, the system is unstable. Depending on the detuning parameter $\Delta\omega$, an increase of E_I can either lead to a stabilization of this state, or the appearance of a Turing unstable state, coexisting with the formerly mentionned unstable state. Further increasing the optical injection power brings a stable state coexisting with a Turing unstable state (that is, the combination of the two previously mentioned effects). With ever increasing optical injection strength, the stable state disapears, to leave the Turing unstable state as the only possible state of the system. Finally, if the frequency difference $\Delta\omega$ is high enough, this Turing unstable state turns into a stable state.

A parameter set of particular interest is depicted in Figs. 3.7 and 3.8. These parameters are the same, apart from $\mu = 1.01$, and $\alpha = 5$, in a small detuning parameter range. In these figures, a region of coexistence of two different Turing branches with a stable homogeneous steady state exists. That means that two different patterns can *in principle* be generated from the same initial condition, alongside with a homogeneous state, for the same parameter values (just by changing the initial condition). Even though the homogeneous steady state has been observed, as well

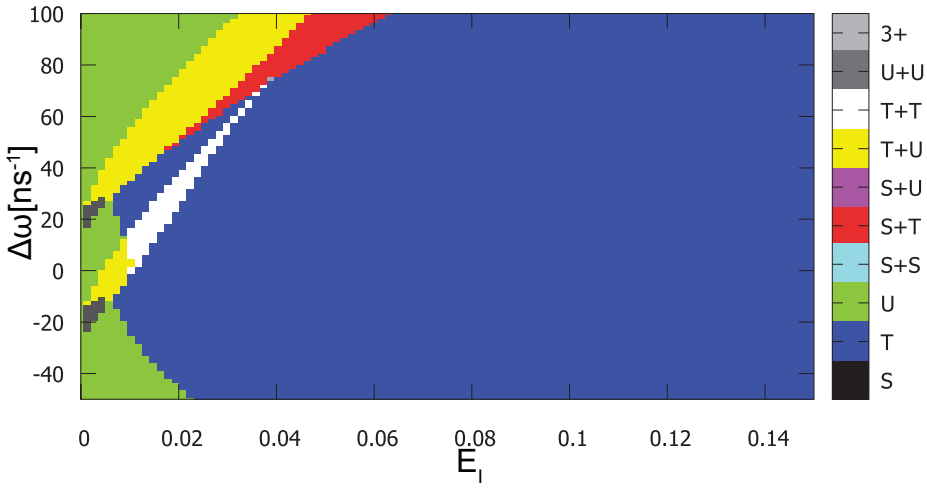

Fig. 3.7: Mapping of spin-flip VCSEL model homogeneous solution and their stability in the plane of injection strength E_I-frequency detuning between optical injection and VCSEL cavity $\Delta\omega$. The color code is the same as in Fig. 3.6, with deep grey (white) describing the coexistence of two (Turing)unstable states. Light grey corresponds to the presence of three states. Parameters are the same as in Fig. 3.6, apart from $\mu = 1.1$, and $\alpha = 5$.

as one of the patterns, the second pattern has not yet been observed numerically, and is the subject of ongoing work.

3.4 VECTOR LOCALIZED STRUCTURES IN THE VCSEL SPIN FLIP MODEL

Numerical simulations of Eqs. 3.36-3.39 have been performed in one of the domains of coexistence between a homogeneous steady state and a Turing unstable state: the domain between the lines A and B of Fig. 3.5. Results have been plotted using relations 3.5-3.8 as a function of the Stokes parameters. This is shown in Fig. 3.9. This localized structure does not have a linear polarization state, as the Stokes parameter S_3 is clearly higher than the background level on the localized structure.

Numerical simulations have been repeated in one dimension for comparison with the experimental results presented in Fig. 3.3. They are presented in Fig. 3.10. As can be seen from this figure, the numerically simulated localized structures exhibit a quite large s_3. Comparing this figure with the experimental results shown in Fig. 3.3,

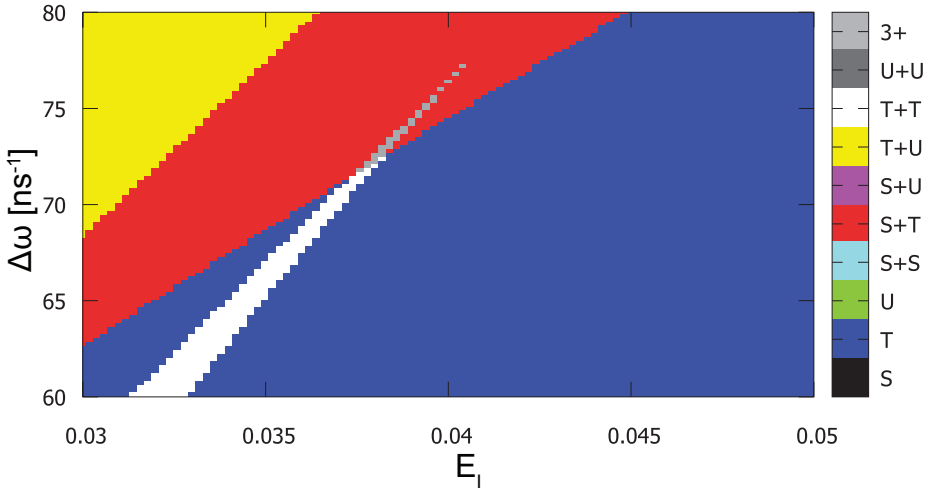

Fig. 3.8: Close-up of Fig. 3.7 for the tristable regime.

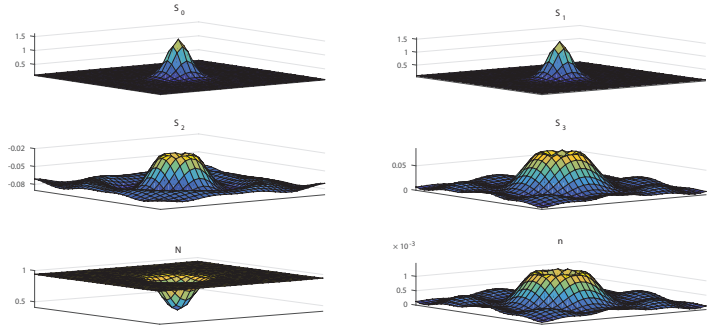

Fig. 3.9: (Color Online) Numerical evidence of presence of dissipative structures in the spin-flip VCSEL model described by Eqs. 3.36- 3.39. Parameters are the same as in Fig. 3.5, with $E_I = 0.265$. Integration has been performed using a Runge-Kutta of order 4 method with a time step of 0.0001 for the temporal integration, and a finite difference method of accuracy 4 and space step 0.045 for the spatial integration on a 50×50 grid.

we observe qualitatively the same behavior. Some small divergences between the two figures can be explained by the lack of knowledge of the spin-flip decay rate that is important for the modelling.

3.5 CONCLUSION

In this chapter, we have built an experimental setup for generation and characterization of vector localized structures in the transverse section of a broad area VCSEL. Bistability corresponding to the spontaneous appearance and disappearance of a localized structure has been observed, as a function of optical injection power. The Stokes parameters of these localized structures have been measured, for orientations of the optical injection linear polarization varying in a 90° span. This analysis revealed that localized structures acquired ellipticity.

A model for describing the polarization dynamics of localized structures in a broad area VCSEL has been derived: the VCSEL spin-flip model. Based on this model, we performed a linear stability analysis. That is, we investigated the dependance of the homogeneous steady states of the system and their linear stability analysis as a function of optical injection strength E_I, and, in a second stage, as a function of optical injection strength E_I, and of the frequency detuning between optical injection and the VCSEL frequency $\Delta\omega$. This linear stability analysis revealed a bistable region of coexistence between a Turing unstable branch, and a homogeneous stable branch. Localized structures have been numerically found in this regime. Linear stability analysis of the VCSEL spin-flip model in the plane optical injection strength-frequency detuning between optical injection and VCSEL cavity has led to the discovery of a tristable region.

Numerical simulations of the VCSEL spin-flip model have been compared with experimental data. There is a good agreement between numerical and experimental data. A quite large ellipticity of the polarization state of localized structures, described by the s_3 parameter, has been both measured and computed to be as high as $s_3 \approx 0.2$.

One may expect that, owing to its general character, the vector localized structure should be observed in other spatially extended systems. Using localized structures in broad-area VCSELs that can be switched on and off independently as pixels for information processing [25] constitutes a bitmap. Considering the Stokes parameters of the vector localized structures demonstrated here, one would potentially create a colormap instead of a bitmap, i.e. each pixel contains information in a 3-parameter space (s_1, s_2, s_3) that easily can be translated into a color code. In such a way, the density of information can be dramatically increased.

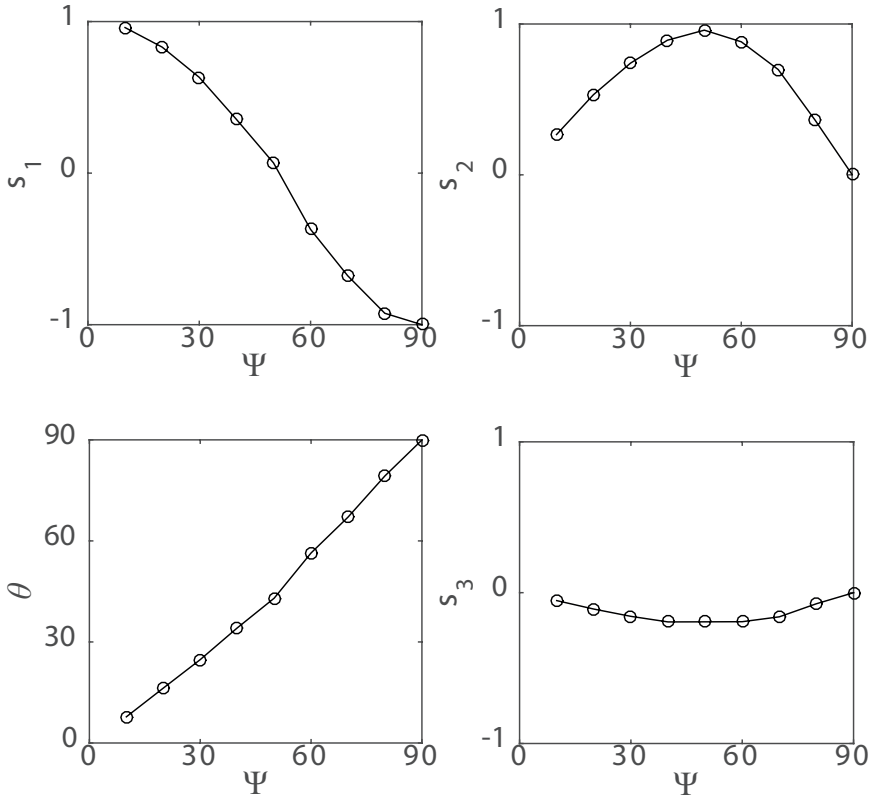

Fig. 3.10: Stokes parameters of numerically generated CSs as a function of Ψ. Parameters are $a = 1\text{ns}^{-1}$, $\alpha = 3, \Delta\omega = 200\text{ns}^{-1}, \gamma_{\|} = 1\text{ns}^{-1}, \gamma_a = 0.1\text{ns}^{-1}, \gamma_p = -20\text{ns}^{-1}, \gamma_j = 50\text{ns}^{-1}, \kappa = 200\text{ns}^{-1}$ and $\mu = 1.05$. Various values of E_I have been used.

4

MOTION OF LOCALIZED STRUCTURES DUE TO DELAYED FEEDBACK

Delayed feedback is a well documented issue, that has a tremendous impact on the dynamics of almost any system (see e.g. [65]). The interest of their use in lasers has been realized very early (see by example a review on this matter [51]). A frequency-selective optical feedback has been proven to allow localized structures generation in VCSELs [33]. Even in that context, localized structures appear as stable stationary objects.

However, delayed feedback can theoretically set these structures into motion. This feature has been abundantly discussed in the litterature (see by example [66, 67, 68, 69, 70]), even though no experimental observation has been performed so far.

In this chapter, we will investigate theoretically when and how fast does this motion occur, in two different cases. First, we will restrict ourselves to the nascent bistability regime, as in Eq. 2.16. We will first evidence this delay-induced motion of localized structures numerically. Then, we will derive an analytical expression for the threshold associated with this motion, as well as for the velocity of localized structures. In a second stage, this analysis is repeated in the more general case of the VCSEL scalar model described by Eqs. 2.1-4.2, supplemented with a delay term.

4.1 INTRODUCTION

In this chapter, we consider the system described in Fig. 4.1. We place ourselves in the validity framework of Eqs. 2.1-4.2, that is, the VCSEL is locked in polarization and frequency to the optical injection, we consider only one cavity mode for lasing emission, apply the mean field limit and the slowly variable amplitude approximation. Moreover, we consider the feedback in the Rozanov-Lang-Kobayashi approach [71, 72]. This means that we neglect standing waves developping in the external cavity. Instead, we only consider light emitted to come back to the VCSEL after one and only one round trip in the external cavity. If the external cavity is of length L, the round trip time τ is then $\tau = 2L/c$. In these approximations, the equation describing

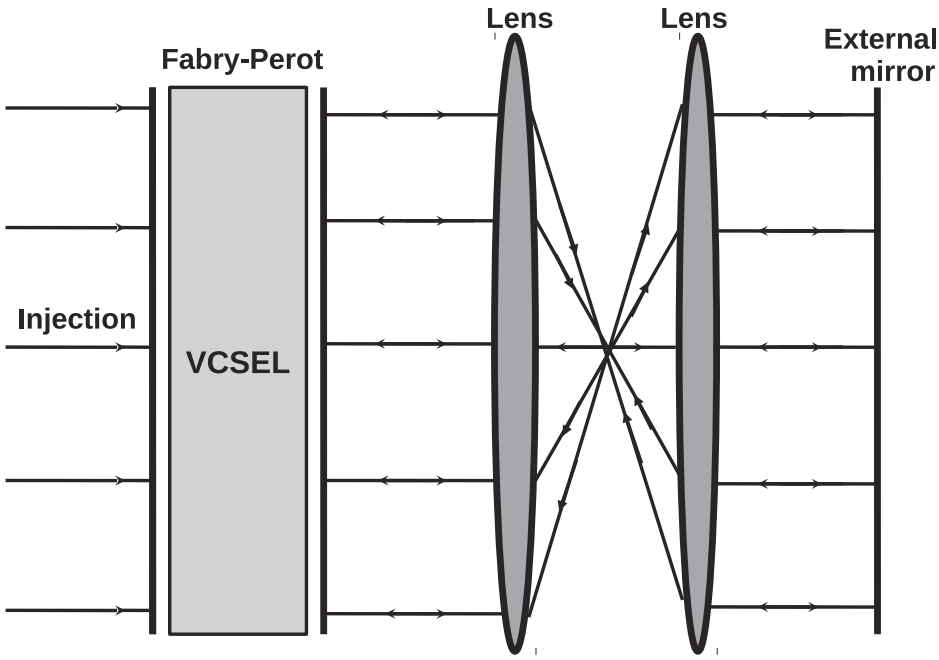

Fig. 4.1: VCSEL submitted to optical injection and placed in an external cavity, where diffraction is compensated.

the spatio-temporal evolution of the carrier population remains unchanged: Eq. 4.2. The spatio-temporal evolution of the electric field yields

$$\begin{aligned}\frac{\partial E}{\partial t'} &= -(1+\eta+i\theta)E + 2C(1-i\alpha)(Z-1)E \\ &\quad + i\nabla_{\perp}'^2 E + E_I + \zeta e^{i\varphi}E(t-\tau),\end{aligned} \tag{4.1}$$

$$\frac{\partial Z}{\partial t'} = \quad -\gamma\left[Z - I + |E|^2(Z-1) - d_f\nabla_{\perp}'^2 Z\right]. \tag{4.2}$$

In these equations, τ has been scaled the same way t has been, to the photon lifetime. The phase of the feedback is ϕ, and the scaling and efficiency of the optical feedback are described by the parameter ζ. Other parameters are described in chapter 2

This equation will be studied in Sec. 4.2.3.

For the moment, we will place ourselves in the validity regime of Eq. 2.16, that is, small cavity detuning and nascent bistability regime. Additionally, we place ourselves in the large external cavity regime (which allows to scale the delay time the

same way time has been scaled), weak feedback regime, and either constructive or destructive optical feedback. The feedback term is hence scalar, and can be integrated in Eq. 2.16 directly. This model now yields

$$\frac{\partial f}{\partial t} = y - f\left(p + f^2\right) + \left(d - \frac{5f}{2}\right)\nabla_\perp^2 f - a\nabla_\perp^4 f - 2(\nabla_\perp f)^2 + \eta f(t-\tau). \quad (4.3)$$

In this equation, $|\eta|$ is the scalar feedback amplitude. Its sign describes whether the interference is constructive ($+$ sign) or destructive ($-$ sign). The next section is devoted to the study of the localized structure delay-induced motion in the restricted framework of this equation.

4.2 NASCENT BISTABILITY REGIME

To investigate delay-induced motion in the framework of Eq. 4.3, we first perform a linear stability analysis of this equation, before investigating this model numerically. In the last part, we derive the quantities associated with the delay-induced motion: threshold for motion, and velocity of this motion.

4.2.1 *Linear Stability Analysis*

The homogeneous steady state solutions $\bar{f}$ of Eq. 4.3 are solutions of

$$y = \bar{f}\left(p - \eta + \bar{f}^2\right). \quad (4.4)$$

We consider a small deviation around the homogeneous state $\bar{f}$ proportional to $e^{\lambda t + \mathbf{k}\cdot\mathbf{r}}$, where $\mathbf{r} = (x, y)$ and $\mathbf{k}$ is the transverse wavevector. The corresponding transcendental characteristic equation is

$$\lambda = -\left(3\bar{f}^2 + p\right) + \left(\frac{5\bar{f}}{2} - d\right)k^2 - ak^4 + \eta e^{-\lambda\tau}. \quad (4.5)$$

Turing instabilities correspond to the occurrence of zero real root $\lambda = 0$ and $\partial\lambda/\partial k = 0$.

Comparing the homogeneous steady states 4.4 with the homogeneous steady states f_s of Eq. 2.16 described in Eq. 2.19, we remark that the change of variable $p \to p - \eta$ is equivalent to $f_s \to \bar{f}$. In the specific case of the investigation of Turing instabilities, where $\lambda = 0$, this change of variable also changes the characteristic equation Eq. 2.20 to Eq. 4.5. For these reasons, the results derived in Sec. 2.5 are

directly translatable to Eq. 4.3, just by performing the change of variable $p \to p - \eta$. This includes Eqs. 2.21 to 2.23, and table 2.1. For the sake of compactness, we will refer in the rest of this chapter to Eqs. 2.21 and 2.23 when needed, for equations taking into account this change of variables.

The delayed feedback however has a strong influence on the system, not only because of its symmetry breaking properties. Even if one considers only a Turing instability, a change in the value of the parameter η has the same effect as a change with opposing sign in the value of the parameter p. To illustrate this statement, different marginal stability curves associated with different values of feedback strength η are depicted in Fig. 4.2. Critical points as a function of the feedback strength are evidenced in Fig. 4.3. Figure 4.4 represents the critical wavenumbers associated with modulational instabilities.

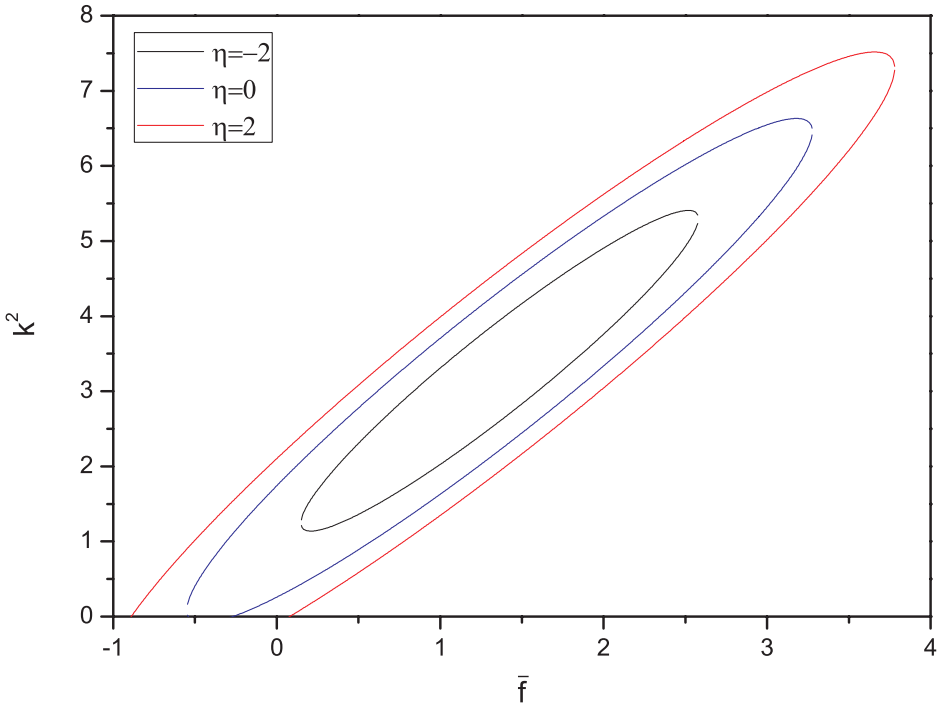

Fig. 4.2: Marginal stability curves in the plane $(\bar{f}, k^2)$. Parameters are $p = -0.9$, $d = -1.5$ and $a = 0.75$. Different feedback strengths have been considered: $\eta = -2$ (black),$\eta = 0$(blue) and $\eta = 2$(red). Results obtained using Eq. 2.21.

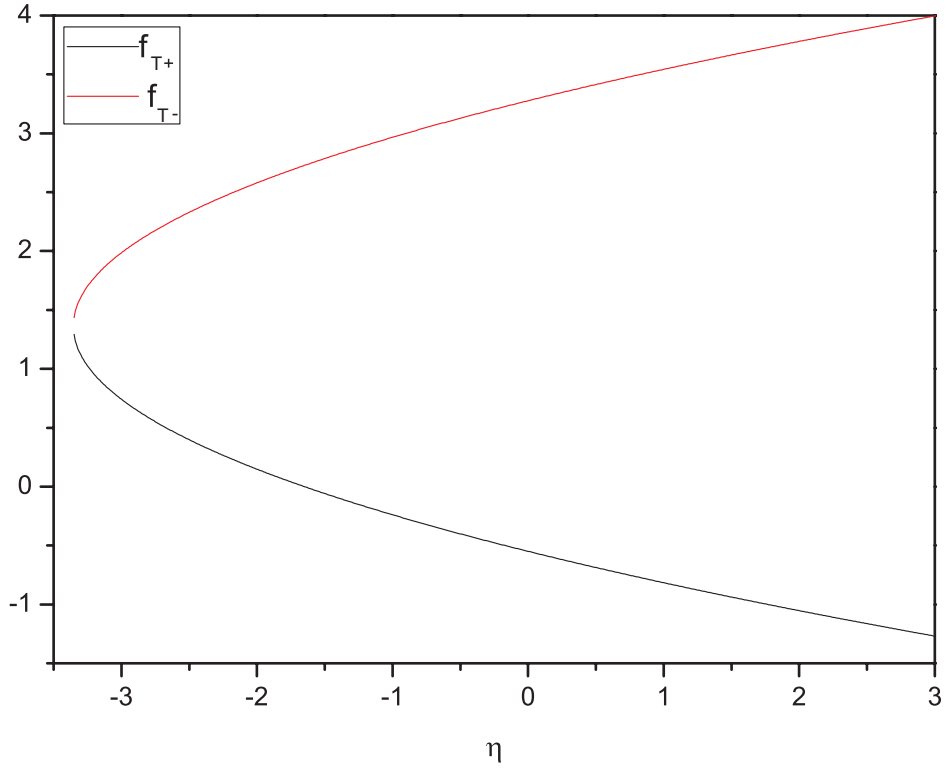

Fig. 4.3: Turing instability thresholds as a function of the feedback strength. Parameters are $p = -0.9$, $d = -1.5$ and $a = 0.75$. Results obtained using Eq.(2.23).

Delayed feedback has a much more important influence when it comes to studying the effects of a travelling wave instability. This instability occurs when a pair of complex conjugate eigenvalues has a zero real part, i.e., $\lambda = \pm i\Omega$. That is, when

$$\eta \cos(\Omega\tau) = (3\bar{f}_{TW\pm}^2 + p) + (d - \frac{5\bar{f}_{TW\pm}}{2})k_{TW\pm}^2 + ak_{TW\pm}^4, \quad (4.6)$$

$$\eta \sin(\Omega\tau) = -\Omega. \quad (4.7)$$

Two examples of stability curves associated with the travelling wave instabilities are shown in Figs. 4.5 and 4.6. These curves describe the evolution of the homogeneous steady states as functions of driving field y in the monostable and bistable regimes. They also describe the unstable wave numbers associated with the travelling-wave instabilities as a function of the homogeneous steady state.

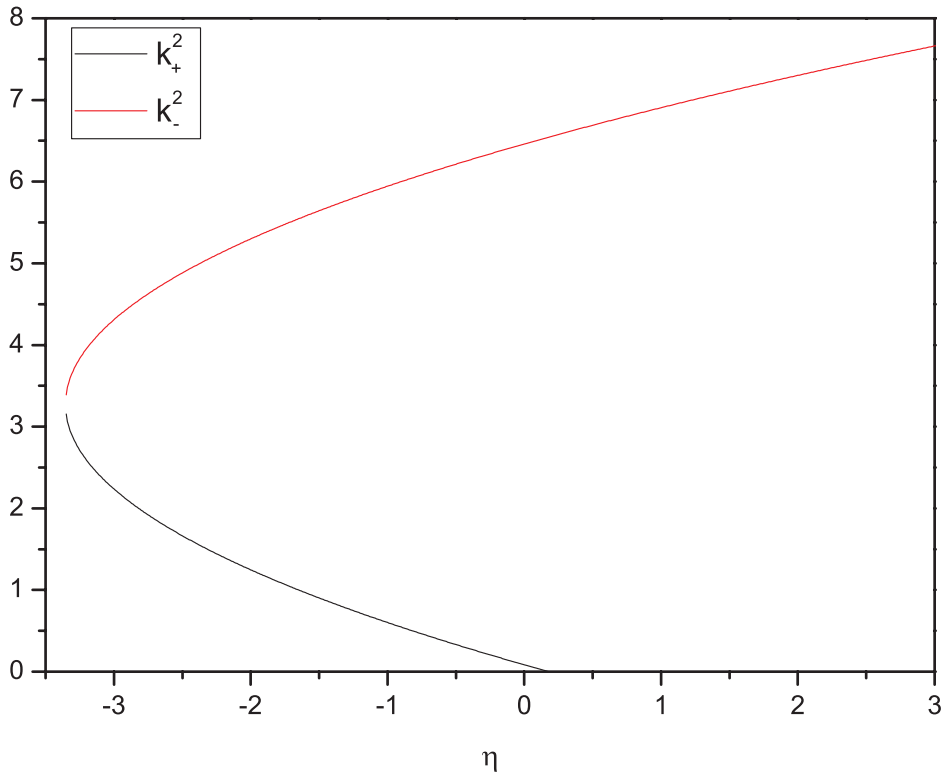

Fig. 4.4: Critical wavenumbers associated with modulational instabilities as a function of the feedback strength. Parameters are $p = -0.9$, $d = -1.5$ and $a = 0.75$. Results obtained using Eq. 2.21

4.2.2 *Numerical simulations*

If the delayed feedback is weak enough, then Eq. 4.3 admits stationary localized structures. In Fig. 4.7, we present numerical simulations of Eq. 4.3 with $\eta = 0.01$, $\tau = 1$, and the rest of the parameters being equal to the ones of Fig. 2.15. Clearly, the snaking bifurcation mechanism discussed in chapter 2 and shown in Fig. 2.16 is still present when the optical feedback is weak.

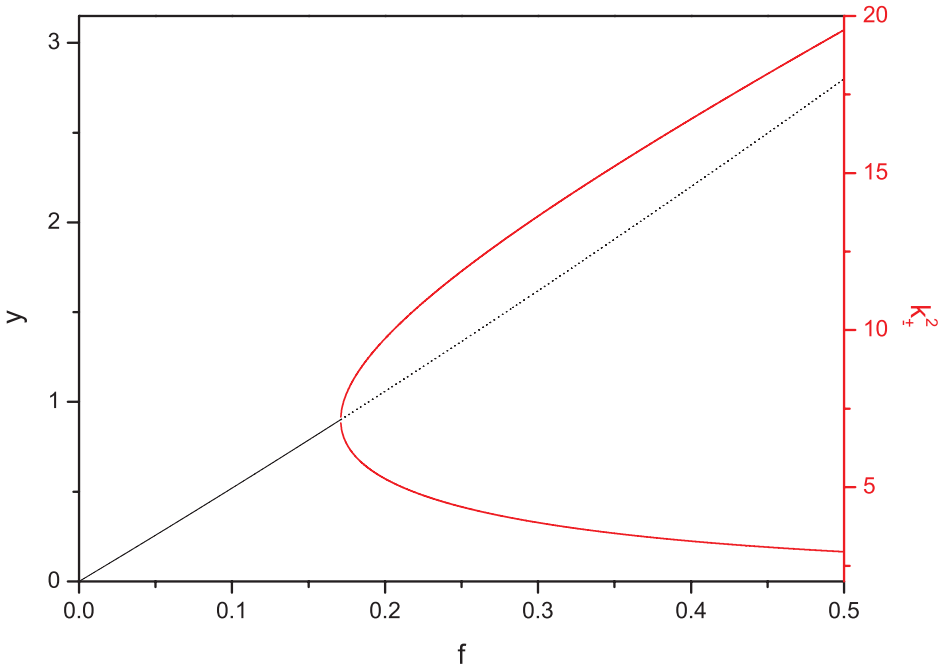

Fig. 4.5: Stability curves associated with the travelling wave instability in the monostable regime. Black, full (dashed) line: injection strength as a function of the homogeneous stable (unstable) steady state. Results obtained using Eqs. 4.4 and 4.5. Red: wavenumber of the travelling wave instability as a function of the homogeneous steady state. Results obtained using Eqs. 4.6 and 4.7. Feedback parameters are $\eta = -0.1$ and $\tau = 15$. Numerical solution of Eq. 4.7 gives the angular frequency for the travelling wave instability: $\Omega = 0.100$. Other parameters are $p = 5$, $a = 0.1$, and $d = -1$.

If the delay feedback strength exceeds a threshold given by $\eta\tau = -1$ [66], a single localized structure starts to move in an arbitrary direction (due to the isotropy in space) as shown in the time space-map of Fig. 4.8.

Figure 4.9 is an example of two bounded localized structures that are initially separated. They start to repel each other, and exhibit a motion in opposite directions. The numerical simulations have been performed using periodic boundary conditions.

Numerical simulations in two dimensions show a similar behavior: in Fig. 4.10, a single peaked localized structure submitted to delayed feedback moves in an arbitrary direction. Repelling of two localized structures due to delayed feedback is shown in Fig. 4.11.

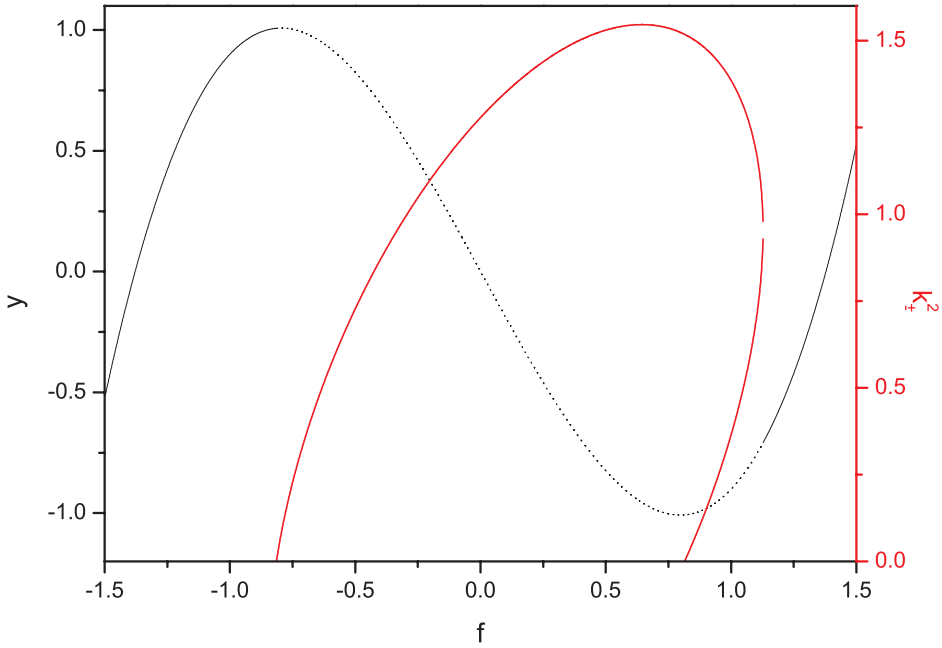

Fig. 4.6: Stability curves associated with the travelling wave instability in the bistable regime. Black, full (dashed) line: injection strength as a function of the homogeneous stable (unstable) steady state. Results obtained using Eqs. 4.4 and 4.5. Red: wavenumber of the travelling wave instability as a function of the homogeneous steady state. Results obtained using Eqs. 4.6 and 4.7. Feedback parameters are $\eta = -0.1$ and $\tau = 15$. Numerical solution of Eq. 4.7 gives the angular frequency for the travelling wave instability: $\Omega = 0.100$. Other parameters are $p = -2$, $a = 2$, and $d = -1$.

4.2.3 *Drift instability: calculation of the velocity*

In this section, we describe the spontaneous motion of localized structures induced by the delayed feedback, in the framework of Eq. 4.3. We calculate the threshold value of the feedback strength above which localized structures start to move in an arbitrary direction and derive an expression for the velocity of the localized structure.

To derive the drift instability threshold, we will apply a method similar to the one used in Ref. [66]. To do so, we rewrite equation (4.3) in the form

$$\begin{aligned}\frac{\partial f}{\partial t} &= y - f\left(\tilde{p} + f^2\right) + \left(d - \frac{5f}{2}\right)\nabla_\perp^2 f \\ &\quad - a\nabla_\perp^4 f - 2(\nabla_\perp f)^2 + \eta[f(t-\tau) - f(t)],\end{aligned} \tag{4.8}$$

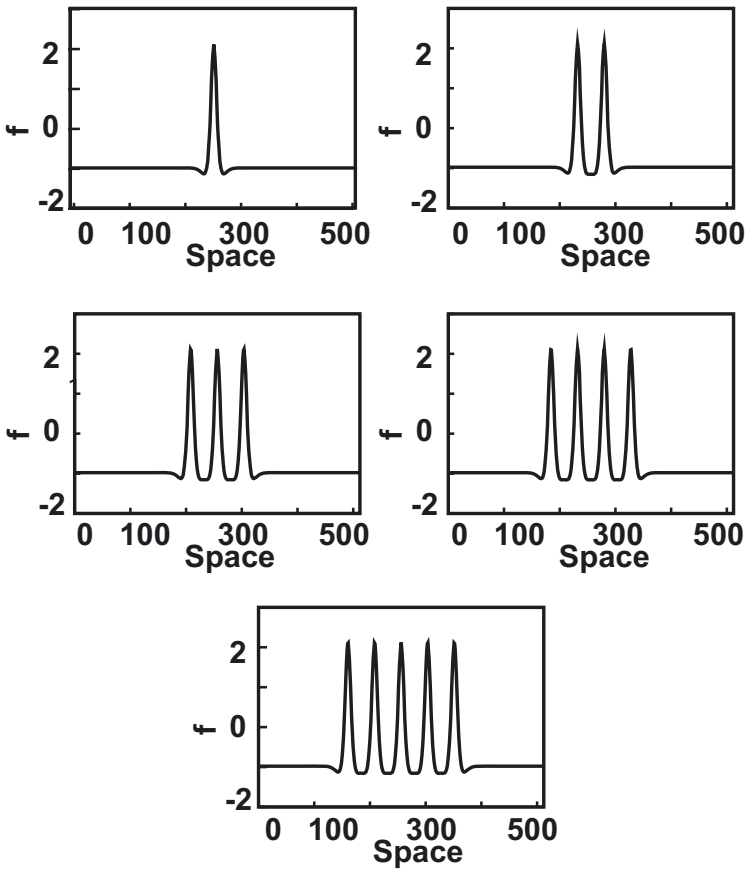

Fig. 4.7: Numerical simulation of Eq. 4.3 in one dimension, with one (up left) to five (down) peaked localized structures. Parameters are $y = -0.35$, $p = -0.7$, $d = -1.2$, $\eta = 0.1$, $\tau = 1$, and $a = 0.75$.

with $\tilde{p} \equiv p - \eta$. We assume that Eq. 4.8, without the term $\eta[f(t-\tau) - f(t)]$, has a stable stationary radially symmetric structure solution. f is then only a function of the distance to the center of this structure $f = f_0(|\mathbf{r}|)$. Stability of this solution means all the solutions Λ of the following eigenvalue problem:

$$\mathcal{L}_\perp A = \Lambda A \tag{4.9}$$

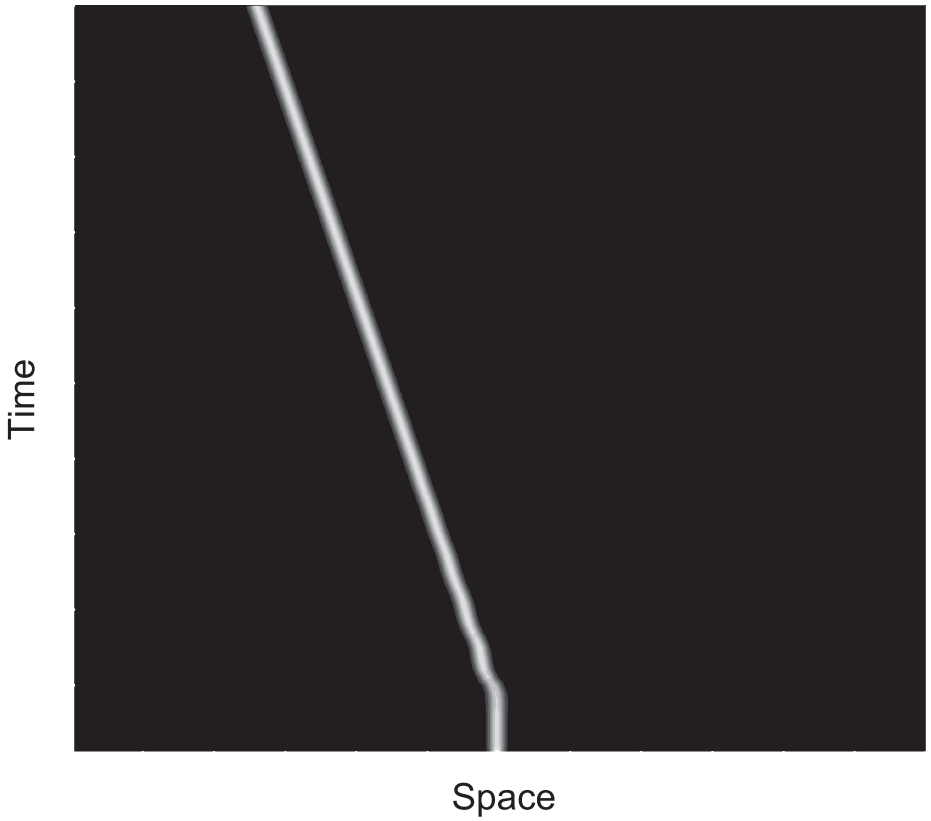

Fig. 4.8: Space-time map of a moving localized structure solution of Eq. 2.16 in 1 dimension. Parameters are $y = -0.5$, $p = -0.9$, $d = -1.5$, $\eta = -0.15$,$\tau = 15$ and $a = 0.75$.

with the self adjoint operator

$$\mathcal{L}_\perp = -\left(\tilde{p} + 3f_0^2 + \frac{5\nabla_\perp^2 f_0}{2}\right) + \left(d - \frac{5f_0}{2}\right)\nabla_\perp^2 - a\nabla_\perp^4 \qquad (4.10)$$

are real and negative except for a pair of zero eigenvalues, corresponding to the translational invariance of Eq. 4.8, $\Lambda_{1,2} = 0$. Since the term $\eta[f(t-\tau) - f(t)]$ vanishes at any stationary solution, the stationary structure $f_0(|\mathbf{r}|)$ is also a solution of Eq. 4.8 with $\eta \neq 0$. We now introduce a slight perturbation in the shape of the

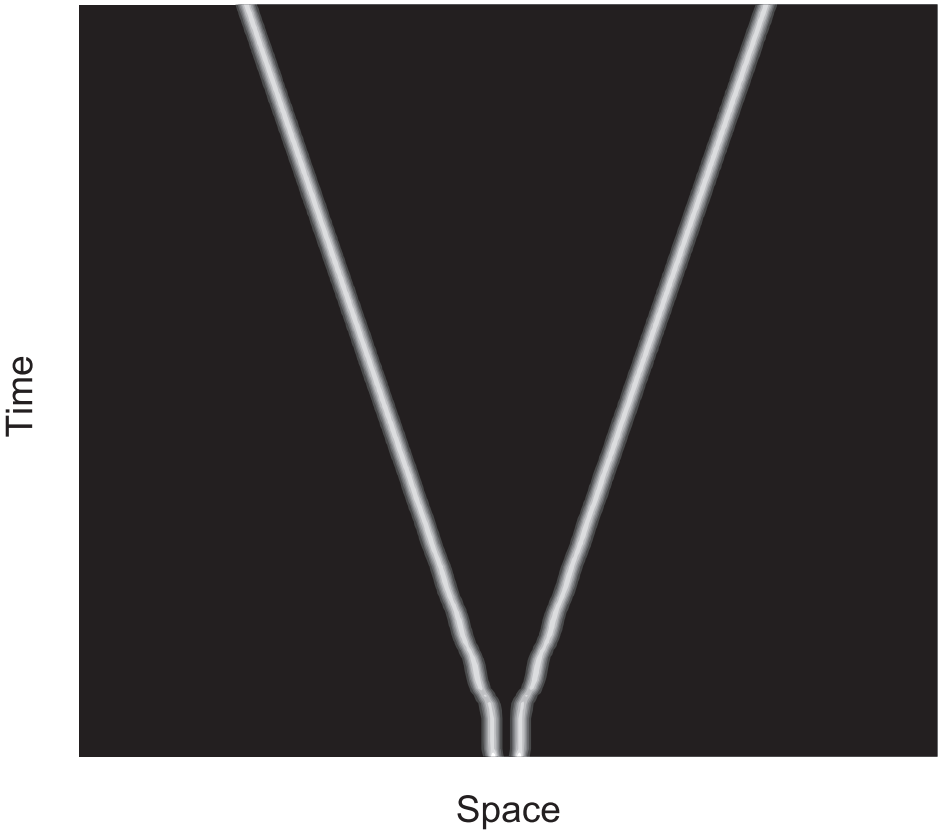

Fig. 4.9: Space-time map of two repelling localized structures solution of Eq. 2.16 in 1 dimension. Parameters are $y = -0.5$, $p = -0.9$, $d = -1.5$, $\eta = -0.15$,$\tau = 15$ and $a = 0.75$.

localized structure in the form $f(r,t) = f_0(|\mathbf{r}|) + Ae^{\mu t}$ into Eq. 4.8. Extracting the linear contributions in the perturbation brings

$$\mathcal{L}_\perp A = \left(\mu + \eta(1 - e^{-\mu\tau})\right) A, \tag{4.11}$$

From Eqs. 4.10 and 4.11 we notice that, for $\eta \neq 0$, the stability of localized structure solution f_0 requires that the real parts of all the solutions μ of the equation

$$\mu + \eta(1 - e^{-\mu\tau}) = \Lambda \tag{4.12}$$

must be non-positive for all Λ.

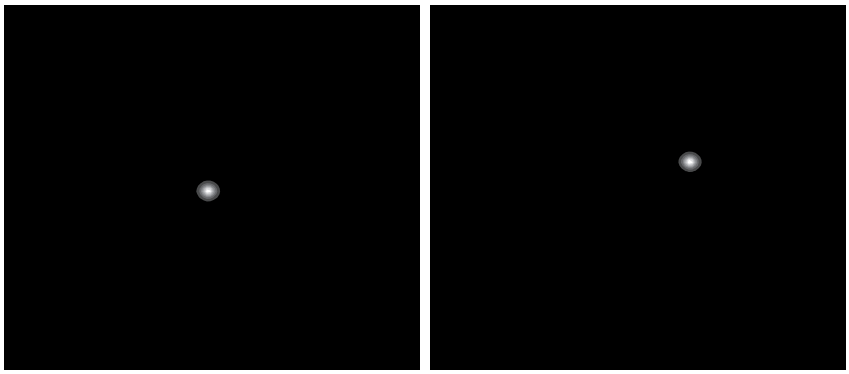

Fig. 4.10: A moving localized structure solution of Eq. 2.16 in 2 dimensions. Parameters are $y = -0.5$, $p = -0.9$, $d = -1.5$, $\eta = -0.15$,$\tau = 15$ and $a = 0.75$.

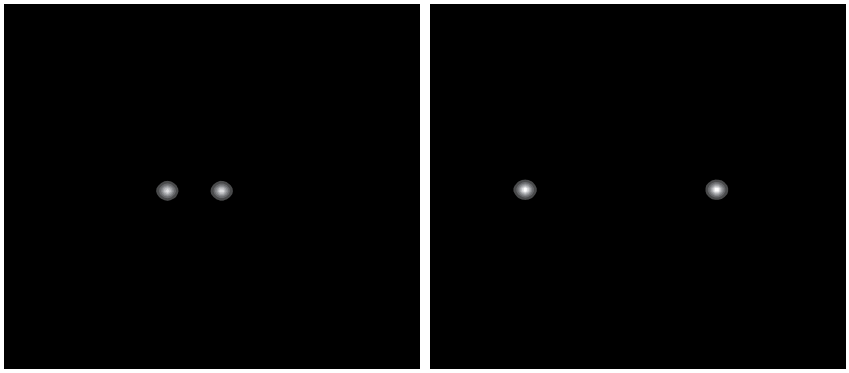

Fig. 4.11: Two repelling localized structures solution of Eq. 2.16 in 2 dimensions, at t=20 and t=100. Parameters are $y = -0.5$, $p = -0.9$, $d = -1.5$, $\eta = -0.15$,$\tau = 15$ and $a = 0.75$.

In particular, assuming that $|\mu| << 1$ and expanding Eq. 4.12 up to the second-order terms in μ, we obtain two real solutions, for the twofold degenerate eigenvalue $\Lambda_{1,2} = 0$ that read

$$\mu_{1,2} = \frac{2(\eta\tau + 1)}{\eta\tau^2}, \mu_{3,4} = 0, \tag{4.13}$$

where zero solutions $\mu_{3,4}$ are associated with the translational symmetry of the model equations and $\mu_{1,2}$ change their sign at the drift instability point $\eta\tau = -1$. At this point, where Eq. 4.11 has the fourfold degenerate solution $\mu_{1,2,3,4} = 0$, the stationary structure solution loses stability, and the uniformly moving structure solution bifurcates from the stationary one. According to Eq. 4.13, the stationary structure is stable for $-1/\tau < \eta < 0$ and becomes unstable for $\eta\tau < -1$. The velocity of the moving single-localized structure can be estimated by performing an expansion in terms of a small parameter ζ, which measures the distance from the drift instability threshold $\eta\tau = -1 - \zeta^2$. Let us look for a solution to Eq. 4.8 in the form of a uniformly moving-localized structure,

$$f(\mathbf{r}, t) = f_0(\mathbf{R}) + \zeta^3 \delta f(\mathbf{R}) + \ldots, \mathbf{R} = \mathbf{r} - \mathbf{v}t, \tag{4.14}$$

where f_0 is the stationary structure solution evaluated at the drift instability point, $\mathbf{v} = \zeta\mathbf{V}$ is the structure velocity, and δf is the correction to the structure shape due to its motion. Plugging this expression into Eq. 2.16, using the expansion $f_0(\mathbf{R} - \zeta V\tau) = f_0(\mathbf{R}) - \zeta\tau\mathbf{V}\cdot\nabla_\perp f_0(\mathbf{R}) + (\zeta\tau\mathbf{V}\cdot\nabla_\perp)^2 f_0(\mathbf{R})/2 - (\zeta\tau\mathbf{V}\cdot\nabla_\perp)^3 f_0(\mathbf{R})/6 + \ldots$, and collecting third order in ζ , we obtain the following inhomogeneous problem:

$$\mathcal{L}_\perp \delta f = \mathbf{V}\cdot\nabla_\perp f_0 + \frac{\eta\tau^3}{6}(\mathbf{V}\cdot\nabla_\perp)^3 f_0. \tag{4.15}$$

According to the solvability condition, the right-hand side of this equation should be orthogonal to the translational neutral modes $A_{x,y} = \partial_x f_0, \partial_y f_0$. By multiplying Eq. 4.15 with the linear combination of these modes $\mathbf{V}\cdot\nabla_\perp f_0/V \equiv f_1$ and integrating over 2D space, we obtain the equation for the localized structure velocity,

$$V\left(\int_{\mathbb{R}^2} f_1^2 dxdy - \frac{\eta}{6}V^2\tau^3 \int_{\mathbb{R}^2} f_1 f_3 dxdy\right) = 0, \tag{4.16}$$

,where $f_3 = \frac{(\mathbf{V}\cdot\nabla_\perp)^3 f_0}{|\mathbf{V}|^3}$. Setting $f_2 = \frac{(\mathbf{V}\cdot\nabla_\perp)^2 f_0}{|\mathbf{V}|^2}$, a non-trivial solution of this equation is given by

$$v = \zeta V = \frac{Q}{\tau}\sqrt{-(1+\eta\tau)} \qquad \text{with} \qquad Q = \sqrt{6\frac{\int_{\mathbb{R}^2} f_1^2 dxdy}{\int_{\mathbb{R}^2} f_2^2 dxdy}}, \tag{4.17}$$

where the relation $\int_{\mathbb{R}^2} f_1 f_3 dxdy = \int_{\mathbb{R}^2} f_2^2 dxdy$ is used, which is obtained by integration by parts. The expression for the structure velocity 4.17 coincides with that obtained earlier for the case of the variational Swift-Hohenberg equation [66], which describes a driven passive nonlinear cavity filled with two-level atoms. This expression is valid not only for a single-localized structure, but also for any localized pattern.

The spatial form of the pattern affects only the factor Q in Eq. 4.17, which can be calculated numerically. In particular, for the parameter values $y = -0.35$, $p = -0.7$, $d = -1.2$, and $a = 0.75$, we obtain $Q = 1.44$. The dependence of the structure velocity on the time delay calculated using Eq. 4.17 is plotted for fixed values of the feedback strength in Fig. 4.12. It is seen that velocity reaches its maximum at $\tau = -2/\eta$, which is $v_{max} = -Q\eta/2$.

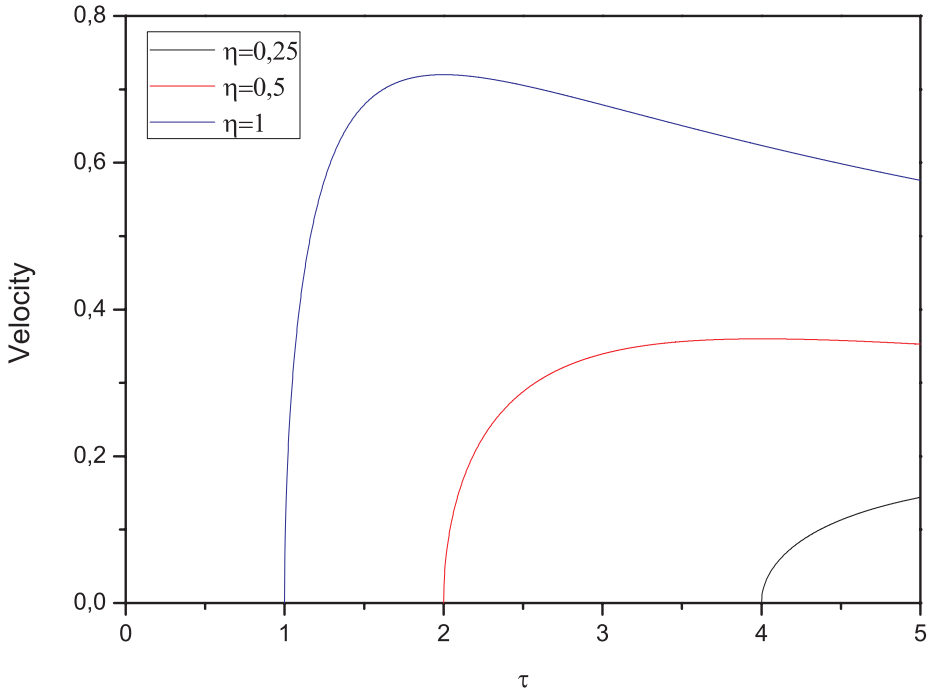

Fig. 4.12: Velocity of the CS as a function of the time delay τ for different values of the feedback strength. Calculated from Eq. 4.17. Parameters are $y = -0.35$, $p = -0.7$, $d = -1.2$, and $a = 0.75$.

4.3 DRIFT ANALYSIS IN THE VCSEL MEAN FIELD SCALAR MODEL

Example of moving two-dimensional LS are shown in Fig. 4.13. The single and the three moving peaks are obtained from numerical simulations of Eqs. (4.1) and (4.2). The boundary condition are periodic in both transverse dimensions.

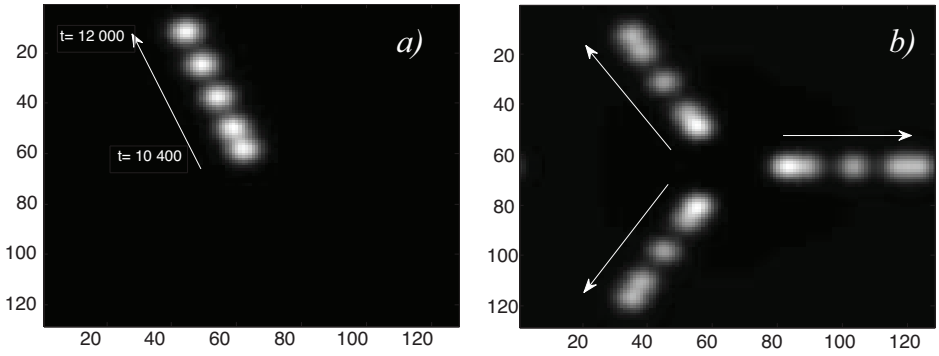

Fig. 4.13: Field intensity illustrating a moving a single (a) and three (b) peak LS. Parameter values are $C = 0.45$, $\theta = -2.$, $\alpha = 5.$, $\eta = 0$. Feedback parameters are $\zeta = 0.135$, $\tau = 100$, $\varphi = 0.5$. Maxima are plain white.

In the case when the system is transversely isotropic, the velocity of the LS motion has an arbitrary direction. The self-induced motion of the LS is associated with a pitchfork bifurcation where the stationary LS loses stability and a branch of stable LSs uniformly moving with the velocity $v = |\mathbf{v}|$ bifurcates from the stationary LS branch. The bifurcation point can be obtained from the first order expansion of the uniformly moving LS in power series of the small velocity v. Close to the pitchfork bifurcation point this expansion reads:

$$E(x - vt, y) = E_0(x - vt, y) + vE_1(x - vt, y) + ... \tag{4.18}$$

$$Z(x - vt, y) = Z_0(x - vt, y) + vZ_1(x - vt, y) + ..., \tag{4.19}$$

where without the loss of generality we assume that the LS moves along the x-axis on the (x, y)-plane. Here $E_0(x, y) = X_0(x, y) + iY_0(x, y)$ and $Z_0(x, y)$ describes the stationary axially symmetric LS profile, which corresponds to the time-independent solution of Eqs. (4.1) and (4.2) with $\tau = 0$. Although formally this solution depends on the feedback parameters ζ and φ we neglect this dependence assuming that the feedback rate is sufficiently small, $\zeta \ll 1$. Substituting this expansion into Eqs. (4.1) and (4.2) and collecting the first order terms in small parameter v we obtain:

$$L \begin{pmatrix} \Re E_1 \\ \Im E_1 \\ Z_1 \end{pmatrix} = \begin{pmatrix} \Re[\partial_x E_0(1 - \zeta\tau e^{i\varphi})] \\ \Im[\partial_x E_0(1 - \zeta\tau e^{i\varphi})] \\ \gamma^{-1}\partial_x Z_0 \end{pmatrix} \tag{4.20}$$

where the linear operator L is given by

$$L = \begin{pmatrix} \mu - 2C(Z_0 - 1) & \nabla^2 - \theta - 2C\,\alpha\,(Z_0 - 1) & -2C(X_0 + \alpha Y_0) \\ -\nabla^2 + \theta + 2C\,\alpha\,(Z_0 - 1) & \mu - 2C(Z_0 - 1) & -2C(Y_0 - \alpha X_0) \\ 2(Z_0 - 1)X_0 & 2(Z_0 - 1)Y_0 & -d\nabla^2 + 1 + |E_0|^2 \end{pmatrix}.$$

By applying the solvability condition to the right hand side of Eq. (3), we obtain the drift instability threshold

$$\zeta\tau = \frac{1 + \gamma^{-1}(b/c)}{\sqrt{1 + (a/c)^2}\cos[\varphi + \arctan(a/c)]} \tag{4.21}$$

with

$$a = \langle\psi_1^\dagger, \psi_2\rangle - \langle\psi_2^\dagger, \psi_1\rangle, \quad b = \langle\psi_3^\dagger, \psi_3\rangle, \quad c = \langle\psi_1^\dagger, \psi_1\rangle + \langle\psi_2^\dagger, \psi_2\rangle. \tag{4.22}$$

Here

$$\psi = (\psi_1, \psi_2, \psi_3)^T = \partial_x\,(X_0, Y_0, Z_0)^T \tag{4.23}$$

is a translational neutral mode of the operator L, $L\psi = 0$, while $\psi^\dagger = \left(\psi_1^\dagger, \psi_2^\dagger, \psi_3^\dagger\right)^T$ is the corresponding solution of the homogeneous adjoint problem $L^\dagger\psi^\dagger = 0$. The scalar product $\langle\cdot\rangle$ is defined as $\langle\psi_j^\dagger, \psi_k\rangle = \int_{-\infty}^{+\infty}\psi_j^\dagger\psi_k\,dxdy$. To estimate the coefficients a and b we have calculated the function $\psi^\dagger$ numerically using the relaxation method in two transverse dimensions, (x, y). The results of these calculations are shown in Fig. 4.14 together with the axially symmetric profile E_0 of the stationary LS. It is seen from this figure that similarly to the neutral mode ψ defined by (4.23) the neutral mode $\psi^\dagger$ of the adjoint operator $L^\dagger$ is an even function of the coordinate y and an odd function of the coordinate x, which is parallel to the LS direction of motion.

The dependence of the critical feedback rate ζ corresponding to the drift instability threshold defined by Eq. (4.21) on the feedback phase φ and carrier relaxation rate γ is illustrated by Fig. 4.15. In this figure the curves labeled by different numbers correspond to different values of γ. Considering the fact that the feedback in Eq. (4.1) is introduced with the minus sign, we see that the drift instability takes place only for those feedback phases when the interference between the cavity field and the feedback field is destructive, i.e. when cos function in the denominator of the right hand side of Eq. (4.21) is positive. On the contrary, when this interference is constructive the feedback has a stabilizing effect on the LS. Furthermore, the slower is the carrier relaxation rate, the higher is the drift instability threshold. Since the stationary LS solution does not depend on the carrier relaxation rate γ, the coefficients a and b in the threshold condition (4.21) are also independent of γ. Therefore, (4.21)

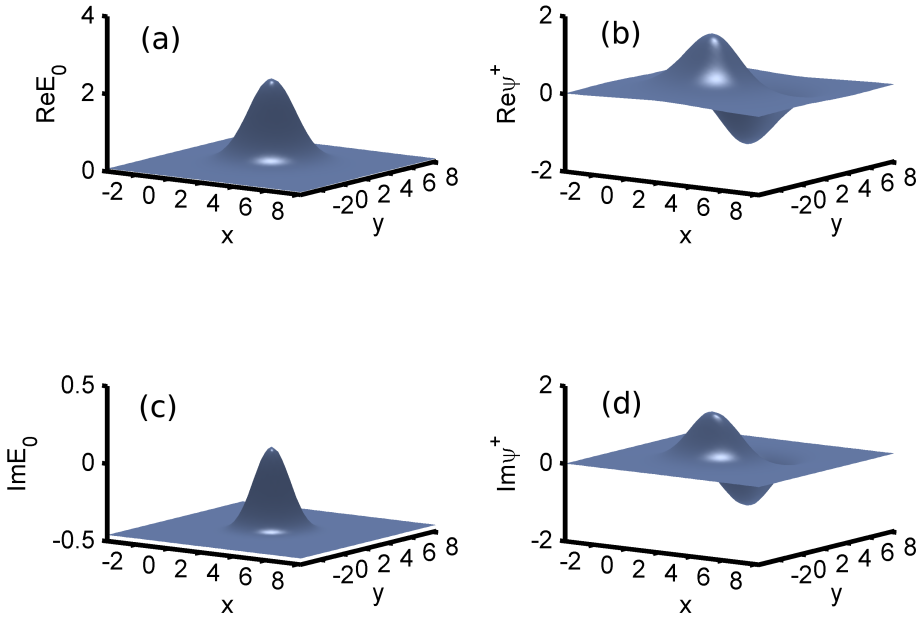

Fig. 4.14: Left panels: real and imaginary parts of the stationary structure profile, $X_0 = \Re E_0$ (a) $Y_0 = \Im E_0$ (c). Right panels: real and imaginary parts of the neutral mode of the adjoint operator L^+, $\psi_1^+ = \Re\psi^+$ (b) and $\psi_2^+ = \Im\psi^+$ (d). Parameters values: $\eta = 0.0$, $\theta = -2.0$, $C = 0.45$, $\alpha = 5.0$, $\gamma = 0.05$, $\tau = 100$, $d = 0.052$, $E_i = 0.8$, $I = 2$.

gives an explicit dependence of the threshold feedback rate on the carrier relaxation rate. In particular, in the limit of very fast carrier response, $\gamma \gg 1$, and zero feedback phase, $\varphi = 0$, we recover from (4.21) the threshold condition $\zeta\tau = 1$ which was obtained earlier for the LS drift instability induced by a delayed feedback in the real Swift-Hohenberg equation [66]. Note that at $\gamma \to \infty$, $a \neq 0$, and $\varphi = -\arctan a$ the critical feedback rate appears to be smaller than that obtained for the real Swift-Hohenberg equation, $\zeta\tau = (1+a^2)^{-1/2} < 1$.

As it was demonstrated above, the bifurcation threshold responsible for self-induced drift of LS in the VCSEL transverse section is obtained by expanding the slowly moving localized solution in the small velocity v, substituting this expansion into the model equations (4.1),(4.2), and matching the first order terms in v. In order to describe the slow evolution of the LS velocity slightly above the bifurcation threshold, one needs to perform a similar procedure with $E = E_0(x - x_0(t), y) + \sum_{k=1}^{3} \epsilon^k E_k(x - x_0(t), y, t) + \ldots$ and $Z = Z_0(x - x_0(t), y) + \sum_{k=1}^{3} \epsilon^k Z_k(x - x_0(t), y, t) +$

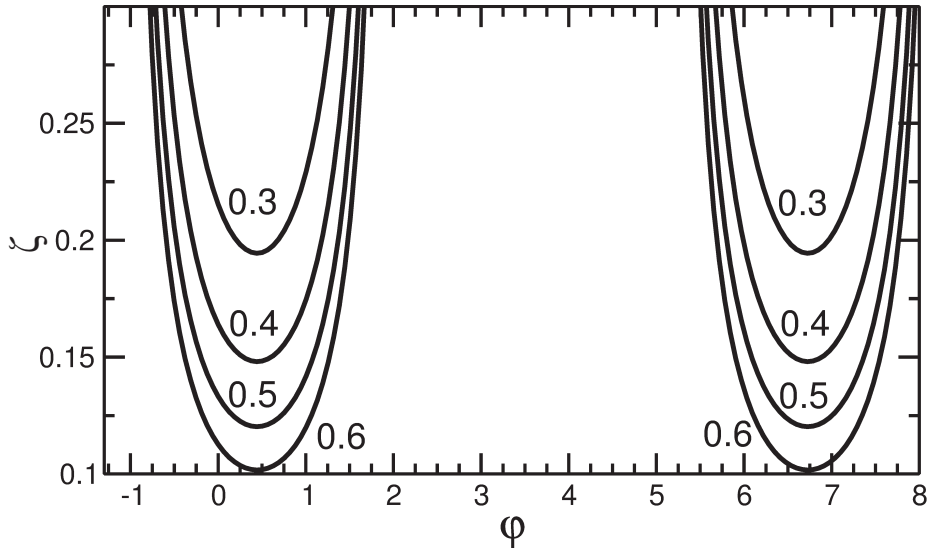

Fig. 4.15: Critical value of the feedback rate ζ corresponding to the drift bifurcation vs feedback phase φ calculated for different values of the carrier relaxation rate γ. The values of the parameter γ are shown in the figure. Other parameters are the same as in Fig. 4.14.

..., where $dx/dt = v(t) = \mathcal{O}(\epsilon)$, $dv/dt = \mathcal{O}(\epsilon^3)$ and ϵ is a small parameter characterizing the distance from the bifurcation point. Then, omitting detailed calculations, in the third order in ϵ, we obtain the normal form equation for the LS velocity:

$$\frac{p}{2}\frac{dv}{dt} = v(\delta\zeta q - \zeta\tau^2 r v^2), \tag{4.24}$$

where $\delta\zeta$ is the deviation of the feedback rate from the bifurcation point. The coefficients q, p, and r are given by $q = a\sin\varphi + c\cos\varphi$, $p = q + b$, and $r = f\sin\varphi + g\cos\varphi + \mathcal{O}(\tau^{-1})$, respectively. Here a, b, and c are defined by Eq. (4.22) and $f = \langle\psi_1^\dagger, \partial_{xxx}Y_0\rangle - \langle\psi_2^\dagger, \partial_{xxx}X_0\rangle$, $h = \langle\psi_3^\dagger, \partial_{xxx}Z_0\rangle$, $g = \langle\psi_1^\dagger, \partial_{xxx}X_0\rangle + \langle\psi_2^\dagger, \partial_{xxx}Y_0\rangle$. The stationary LS velocity above the drift instability threshold is obtained by calculating the nontrivial steady state of Eq. (4.24),

$$v = \sqrt{\delta\zeta}Q, \tag{4.25}$$

$$Q = \frac{1}{\tau}\sqrt{\frac{q}{r\zeta}}. \tag{4.26}$$

The coefficient Q determines how fast the LS velocity increases with the square root of the deviation from the critical feedback rate. The dependence of this coefficient on the feedback phase is illustrated by Fig. 4.16.

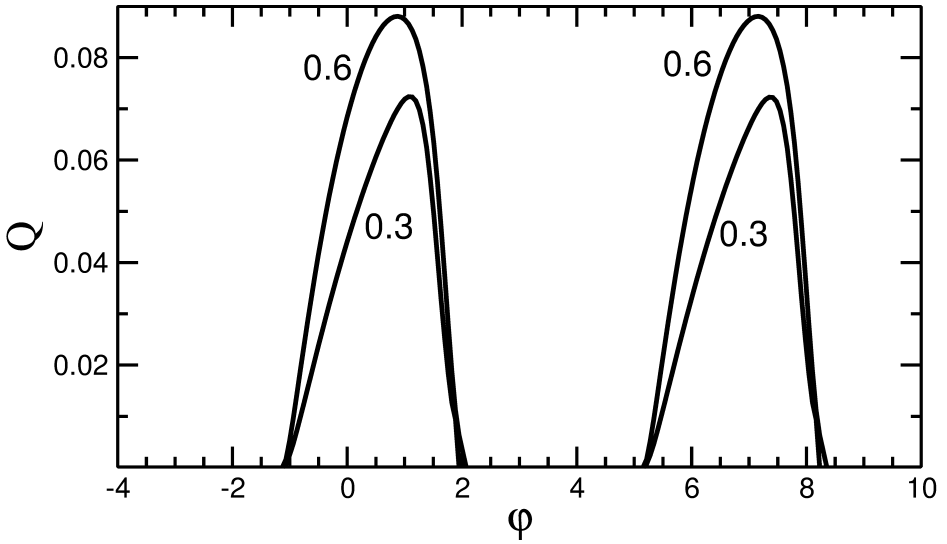

Fig. 4.16: Coefficient Q describing the growth rate of the LS velocity with the square root of the deviation from the critical feedback rate. The values of the parameter γ are shown in the figure. Other parameters are the same as in Fig. 4.14.

4.4 CONCLUSION

In this chapter, we considered a VCSEL submitted to optical injection and delayed optical feedback. To mathematically describe the evolution of such a system, we added a delayed term in the mean-field model, as well as in the reduced model, the modified Swift-Hohenberg equation with a delay term.

In the framework of the modified Swift-Hohenberg equation with a delay term, we performed a linear stability analysis and investigated the Turing pattern formation in the presence of delay, in the monostable and bistable regimes. Numerical simulations have shown the presence of stationary localized structures, as well as moving localized structures. The motion of those localized structures is then linked with a drift instability. The threshold for this instability, and the speed at which it occurs are derived. These quantities depend only on the feedback parameters.

In the more general framework of the VCSEL mean field model, we also numerically and theoretically investigated the motion of localized structures. The motion threshold and speed of the localized structures are found to depend not only on the feedback parameters, but also on the decay rate for charge carriers, as well as on the phase of the optical feedback. We provide analytical expressions for both the threshold of localized structures drfit instability, and the velocity of this motion.

5

TEMPORAL LOCALIZED STRUCTURES IN NONLINEAR FIBER CAVITIES

Localized structures can be spatial, like the ones we described in this thesis so far. Their stabilization mechanisms notably involve diffraction, to couple the spatiotemporal evolution of adjacent points of the plane transverse to the propagation axis together. In the paraxial approximation, the diffraction is modelled by the term $i\nabla_{\perp}^{2}E$ in the models we have used so far.

Localized structures can also be generated in one dimensional systems (such as an optical fiber). In that configuration, the transport process that allows the presence of a localized dissipative structure, and plays the role of diffraction, is chromatic dispersion. To describe chromatic dispersion in the reference frame of a pulse, moving at the group velocity, a term $\partial^2 E/\partial\tau^2$ is introduced. The similarities in the mathematical descriptions of diffraction and chromatic dispersion allow to describe temporal and spatial localized structures in a very similar fashion. However, we have to keep in mind that the objects described by these models are very different: a spatial soliton is a stationary bright peak in the field transverse to the propagation of light, whereas a temporal soliton is a pulse that propagates inside an optical fiber.

In this chapter, we first introduce two different models. The first one describes the polarization properties of a temporal localized structure in a low birefringence fiber, whereas the second describes the effect of high order dispersion effects on temporal localized structures generated in a Photonic Crystal Fiber (PCF) cavity, tailored for minimizing second order dispersion. These two models are a generalization of the well known Lugiato-Lefever model [10]. This model will be presented in section 5.1, alongside with the adaptations that have been performed to describe polarization effects, and the influence of high order dispersion. The model derived for study of polarization effects will be the subject of section 5.2, whereas section 5.3 will be devoted to the study of the influence of higher orders of dispersion.

5.1 INTRODUCTION

High-finesse cavities filled with a Kerr medium and driven by a coherent injected beam (see Fig. 5.1a) are described in the mean field approach by the well known Lugiato-Lefever equation

$$\frac{\partial E}{\partial t} = S - (\alpha + i\delta)E + \frac{i}{2}\left(\frac{\partial^2 E}{\partial x^2} + \frac{\partial^2 E}{\partial y^2}\right) + i|E|^2 E. \tag{5.1}$$

In this equation, $E(t, x, y)$ is the normalized slowly varying envelope for the electric field inside the cavity. The injected field amplitude S is a positive defined quantity, in order to set the origin of the phase.The time variable t corresponds to the slow evolution of E over successive round-trips. α is the cavity losses, δ is the frequency detuning between optical injection and cavity. x and y are the space coordinates in the plane transverse to the propagation of light.

It has been shown in [73] that the Lugiato-Lefever equation 5.1can also be applied to a fiber cavity, as described in Fig. 5.1b). In that case, the term $\frac{i}{2}\left(\frac{\partial^2 E}{\partial x^2} + \frac{\partial^2 E}{\partial y^2}\right)$ is replaced by a single coordinate τ, a fast-time describing the intracavity field envelope evolution within the fiber cavity. It is worth remarking that, in that case, one cannot speak of Turing instability to describe the patterns arising in numerical simulations of Eq. 5.1. Indeed, Eq. 5.1 is written for optical fibers in the reference frame moving with the group velocity. What will appear as a stable pattern in the numerical simulations corresponds physically to a train of pulses. We hence describe this phenomenon as a Modulation Instability (MI), and use the pulsation ω instead of the wavevector k.

It is a classic model for the analysis of several important physical situations, including all fiber cavities [73], ring cavity filled with left-handed materials [74], and the generation of optical frequency combs in microresonators [75, 76]. Equation 5.1 has been analytically and numerically proved to be able to host localized structures in one and two dimensions [13]. Localized structures from this model have also been found experimentally in one dimension [16].

In the first part of this chapter, we discuss the polarization properties of localized structures generated in a low birefringence fiber. Before doing so, it is worth remarking that a study of dissipative structures formed in the transverse plane of a spatially extended cavity described by a variant of eq. 5.1 has been performed in [40]. In this article, the authors modified eq. 5.1, to describe a birefringent Kerr medium. To take into account this birefringence, and study the polarization patterns arising in such a

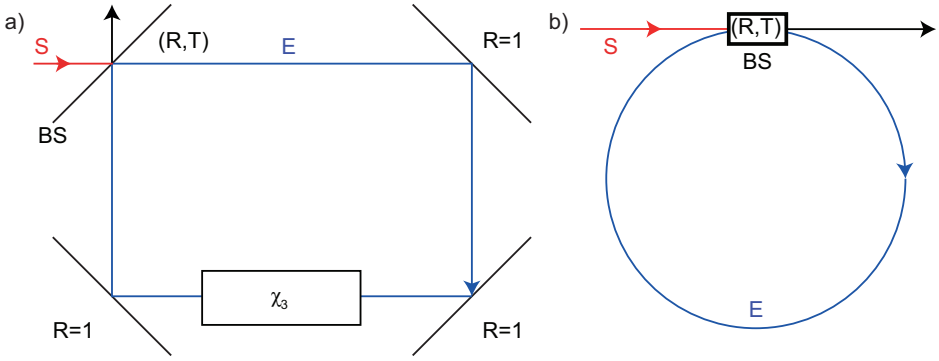

Fig. 5.1: Schematic setup of (a) a spatially extended ring cavity filled with a Kerr medium and submitted to optical injection, and (b) a fiber ring cavity submitted to optical injection. S is the optical injection strength, and E is the slowly varying envelope of the electric field circulating in both configurations. R is the reflectivity of the beamsplitter BS at the entrance of the cavity, T is its transmittivity.

cavity, an interplay between the different components of the electric field needs to be added in the description of the system. This yields [40]

$$\frac{\partial E_\pm}{\partial t} = S_\pm + iE_\pm(A|E_\pm|^2 + (A+B)|E_\mp|^2) - (1+i\theta)E_\pm + ia\nabla_\perp^2 E_\pm. \qquad (5.2)$$

In these equations, the slowly varying electric field envelope and the external optical injection have been expressed in terms of their circularly polarized components $E_\pm$ and $S_\pm$. Losses have been normalized to unity. A and B are parameters related to the susceptibility tensor of the Kerr medium. These equations have been derived for propagation in a free space ring cavity, that is described in Fig. 5.1a). Such a model cannot be adapted to highly birefringent fibers. Indeed, in such systems, the time spent in the cavity depends on the polarization of the electric field. The different polarization components hence cannot be described using the same τ limits, and the same time scales.

We can however consider weakly birefringent fibers, in which this time difference can be neglected. The interplay between the different polarization components then takes place, because of the cross phase modulation. Another effect that one needs to include to properly describe polarization effects in optical fibers is four-wave mixing. However, for the sake of simplicity, and to keep the general form of Eq. 5.1, we neglect this effect. This allows, by changing the chromatic dispersion term into diffraction, to describe two-dimensional localized structures in birefringent materials (see the similarities with Eqs. 5.2).

In that restricted framework, the equations describing the spatio-temporal evolution of the electric field slowly varying envelopes are

$$\frac{\partial E_x}{\partial t} = S\cos(\Psi) - (1+i\theta_x)E_x + i\left(|E_x|^2 + \frac{2|E_y|^2}{3}\right)E_x + i\beta_2\frac{\partial^2 E_x}{\partial \tau^2}, \quad (5.3)$$

$$\frac{\partial E_y}{\partial t} = S\sin(\Psi) - (1+i\theta_y)E_y + i\left(|E_y|^2 + \frac{2|E_x|^2}{3}\right)E_y + i\beta_2\frac{\partial^2 E_y}{\partial \tau^2}. \quad (5.4)$$

Here, E_x and E_y are the parts of the slowly varying electric field envelope polarized in the horizontal and vertical plane, respectively. The holding beam S is real, and positive to fix the origin of the phase, with Ψ its linear polarization direction with respect to horizontal. The detunings between the frequency of the holding beam and the cavity resonances for each polarization direction are θ_x and θ_y. The second order chromatic dispersion coefficient is β_2, considered to be the same for horizontal and vertical polarization directions. The study of this equation set will be the subject of the next section.

In the second part of this chapter, we consider a Photonic Crystal Fiber (PCF) cavity. The term "crystal" is used to describe such fibers because of the periodic arrangement of its transverse section. This periodicity allows notably single mode propagation, among a lot of other possibilities [77]. In particular, one can tune the chromatic dispersion around a certain wavelength, to reduce it significantly.We limit our analysis to PCF cavities operated close to the zero dispersion regime. In that regime, it is necessary to take into account chromatic dispersion of high order.A development in power series of the chromatic dispersion truncated to order four yields [78]

$$\frac{\partial E}{\partial t} = S - (1+i\Delta)E + i|E|^2 E - iB_2\frac{\partial^2 E}{\partial \tau^2} + B_3\frac{\partial^3 E}{\partial \tau^3} + iB_4\frac{\partial^4 E}{\partial \tau^4}. \quad (5.5)$$

In this equation, B_i denotes the chromatic dispersion coefficient of order i, and Δ is the detuning parameter. The study of this system will be the subject of section 5.3

5.2 VECTOR LOCALIZED STRUCTURES IN A LOW BIREFRINGENCE FIBER CAVITY

In order to study the effects of the birefringence on the dynamics of the system, we first perform a linear stability analysis of Eqs. 5.3-5.4. Homogeneous steady states (HSS) of these equations are

$$0 = S\cos(\Psi) - (1+i\theta_x)E_{x0} + i\left(|E_{x0}|^2 + \frac{2|E_{y0}|^2}{3}\right)E_{x0}, \tag{5.6}$$

$$0 = S\sin(\Psi) - (1+i\theta_y)E_{y0} + i\left(|E_{y0}|^2 + \frac{2|E_{x0}|^2}{3}\right)E_{y0}. \tag{5.7}$$

The linear stability analysis with respect to small perturbations of the form $e^{\lambda t + i\omega\tau}$ leads to the characteristic matrix

$$\begin{pmatrix} -1-\lambda-2\Im E_{x0}\Re E_{x0} & A & -\frac{4\Im E_{x0}\Re E_{y0}}{3} & -\frac{4\Im E_{x0}\Im E_{y0}}{3} \\ B & -1-\lambda+2\Re E_{x0}\Im E_{x0} & \frac{4\Re E_{x0}\Re E_{y0}}{3} & \frac{4\Re E_{x0}\Im E_{y0}}{3} \\ -\frac{4\Re E_{x0}\Im E_{y0}}{3} & -\frac{4\Im E_{x0}\Im E_{y0}}{3} & -(1+\lambda+2\Re E_{y0}\Im E_{y0}) & D \\ \frac{4\Re E_{x0}\Re E_{y0}}{3} & \frac{4\Im E_{x0}\Re E_{y0}}{3} & C & F \end{pmatrix}$$

where $A = \theta_x - \left(|E_{x0}|^2 + \frac{2|E_{y0}|^2}{3}\right) - 2\Im E_{x0}^2 + \beta_2\omega^2$, $B = -\theta_x + \left(|E_{x0}|^2 + \frac{2|E_{y0}|^2}{3}\right) + 2\Re E_{x0}^2 - \beta_2\omega^2$, $C = -\theta_y + \left(|E_{y0}|^2 + \frac{2|E_{y0}|^2}{3}\right) + 2\Re E_{y0}^2 - \beta_2\omega^2$, $D = \theta_y - \left(|E_{y0}|^2 + \frac{2|E_{x0}|^2}{3}\right) - 2\Im E_{y0}^2 + \beta_2\omega^2$, $F = -1 + 2\Re E_{y0}\Im E_{y0} - \lambda$.

Steady state solutions $|E_{x0}|^2 + |E_{y0}|^2$ solutions of Eqs. 5.6-5.7 and their stability are shown in Fig. 5.2 for three different values of the detuning θ_x. The injection field S is the bifurcation parameter and the y-axis is the sum of the two components of the electric field $|E|^2 = |E_x|^2 + |E_y|^2$. We observe that, when increasing θ_x, the width of the bistability between a stable and a MI unstable state (delimited by the limit points A and B in Fig. 5.2) increases, whereas the bistability between two modulationaly unstable states (delimited by the limit points C and D in Fig. 5.2) decreases. Furthermore, the bistable regions A-B and C-D move to higher and lower injection strengths, respectively. These combined effects lead to a coexistence of the stable state with two different MI unstable states [See Fig. 5.2(c) and S between C and D]. In this range of parameters and depending on the initial conditions, the system will therefore exhibit either a stable homogeneous state, or a MI pattern corresponding to the intermediate branch A-D, or a MI pattern corresponding to the higher MI unstable branch. We are particularly interested by this situation.

In order to have more information on the region of coexistence of a stable state with two branches of MI unstable states, we map the stability regions in the plane

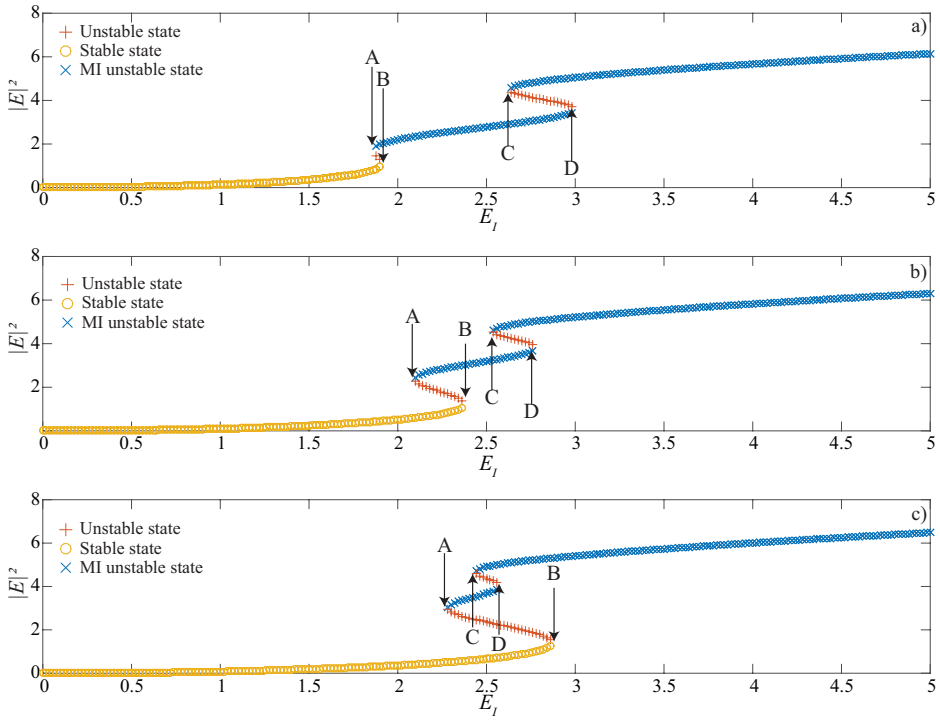

Fig. 5.2: Linear stability analysis for different values of θ_x and with S as the bifurcation parameter. A and B denote the lower and higher limits of a hysteresis, whereas C and D denote the lower and higher limits of the other hysteresis. Parameters are $\beta_2 = 1, \psi = \pi/4$, $\theta_y = 4.3$, $\theta_x = 2$(a), $\theta_x = 2.5$(b), and $\theta_x = 3$(c).

(S, θ_x) as shown in Fig. 5.3. The black and blue regions correspond to areas in which the system admits a stable homogeneous steady state and a modulationaly unstable state, respectively. The red and green colors stand for regions where two homogeneous steady states coexist: the red - coexistence of a stable homogeneous state and a MI unstable state, and green - coexistence of two MI unstable states. Finally, white represents the coexistence of a stable homogeneous state, and two MI unstable states.

Note that for the chosen parameters (especially $\theta_y = 4.3$), the system does not show any monostable regime. This is expected, as for the Lugiato-Lefever model that is not discriminated in polarization, the system is bistable for $\theta > \sqrt{3}$ [10]. We observe that the white area is relatively small compared to other regions. Examples of numerical simulations in this white region are presented in Fig. 5.4. Two different sets of data are presented in this figure, as a function of their Stokes parmaters, which are connected to the linearly polarized components E_x and E_y by

$$S_0 = |E_x|^2 + |E_y|^2, \tag{5.8}$$

$$S_1 = |E_x|^2 - |E_y|^2, \tag{5.9}$$

$$S_2 = E_x^* E_y + E_x E_y^*, \tag{5.10}$$

$$S_3 = i(E_x^* E_y - E_x E_y^*). \tag{5.11}$$

Both simulations sets have been performed with periodic boundary conditions. In Fig. 5.4a) and b), the Stokes parameters S_0 and S_1 corresponding to the low energy pattern are presented. In Fig. 5.4c) and d), the same Stokes parameters for the high energy pattern are presented.

When a stable state and a MI pattern coexist, it is often possible to generate localized structure solutions. In the white region, as detailed in Fig. 5.4, there are two different MI patterns coexisting with a stable state. We hence can expect that the system can generate two kinds of localized structures for the values of parameters in the white area.

Indeed, numerical simulations of Eqs. 5.3-5.4 with periodic boundary conditions in the τ coordinate show evidence of the coexistence of the two possible localized structure states. An example thereof is given in Fig. 5.5.

The initial condition used in this numerical simulation consits of a homogeneous background on which two hard perturbations with different polarization properties have been added, in the vicinity of $\tau = 8$ and $\tau = 30$. As can be seen from Fig. 5.5, there are three distinct regions in space: around $\tau = 8$ and $\tau = 30$ two localized structures labelled A and B, and in between the background. The localized structure labelled A has the higher intensity (S_0 parameter) in space, this localized structure therefore corresponds to the brightest region in space. Next to its maximum value is

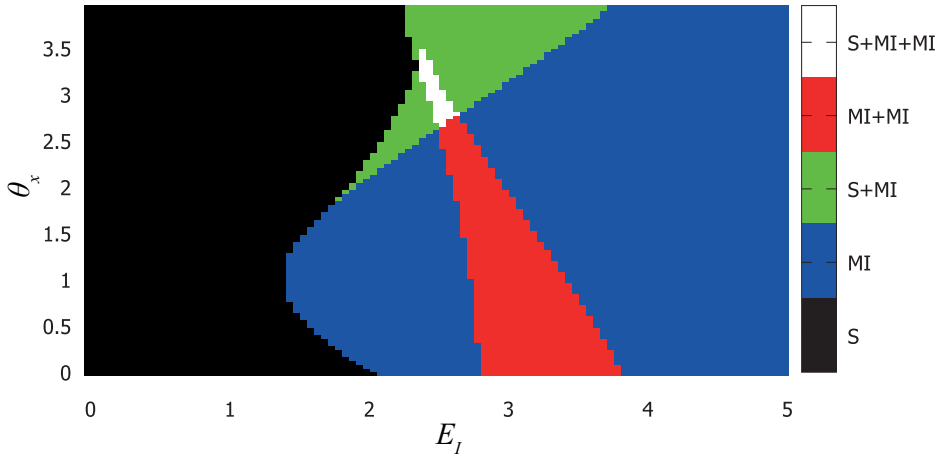

Fig. 5.3: Stability regimes of the homogeneous steady states in the parameter plane (S, θ_x). Black color corresponds to region where the system allows a single stable state, blue to a single MI unstable state, red to the coexistence of a stable state and a MI unstable state, white to the coexistence of two MI unstable states and gray to the coexistence of a stable state with two MI unstable states. The map has been obtained from a linear stability analysis of Eqs. 5.3-5.4. Parameters are the same as in Fig. 5.2.

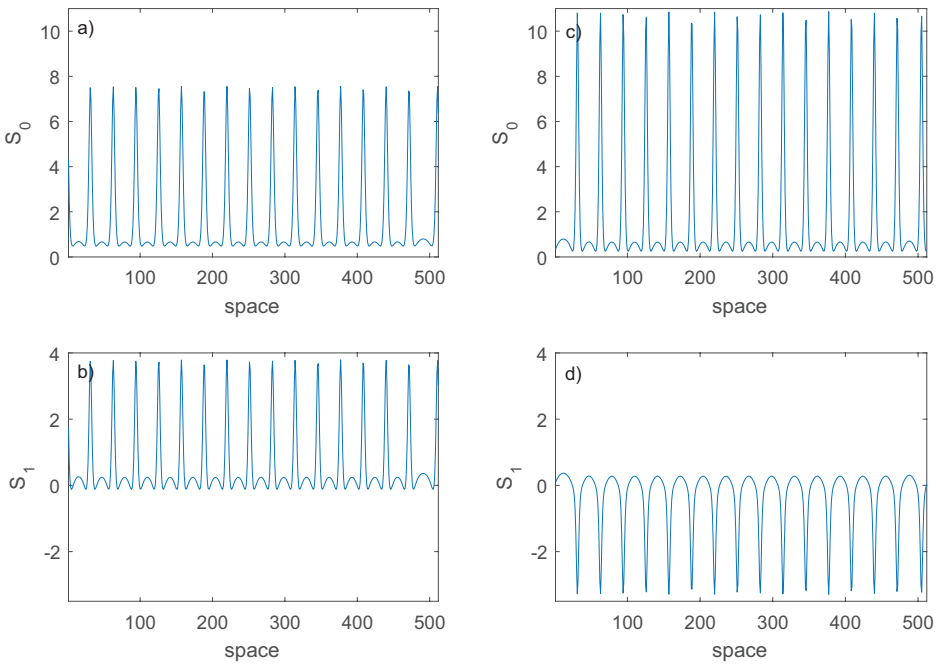

Fig. 5.4: Numerical simulations of Eqs. 5.3-5.4 for $S = 2.54$, $\theta_x = 2.75$, $\beta_2 = 1$, $\theta_y = 4.3$ and $\Psi = \pi/4$. The τ step has been fixed to 0.2, and the time step has been set to 0.01. The sets a),b) and c),d) have been obtained for different initial conditions.

represented its polarization state which is an ellipse. The parameters of this ellipse have been calculated at the maximum value of S_0. Two other ellipses have been drawn on this graph. The lower (unmarked) one represents the polarization state of the background whereas B corresponds to the maximum of the second localized structure. The difference between their polarization states can be evidenced by looking at their Stokes parameters: at its maximum intensity, the localized structure A has a negative S_1 and a positive S_2, whereas the localized structure B has a positive S_1 and a negative S_2. Both these structures have a large negative S_3 (slightly different between localized structures A and B). This indicates a large right handed circular component.

We now compare the properties of these localized structures with the ones of other systems that can also generate different kinds of localized structures. In Refs. [79, 48], they generate three kinds of localized structures. The first one is a classical Polarization Locked Vector Soliton (PLVS), as the ones we deal with in this chapter. The two others are polarization precessing vector localized structures with a spiral attractor, and a vector localized structure evolving on two semicircles on the Poincaré sphere. Here, we describe a system able to host two PLVS attractors, on two Poincaré spheres with different radii. In Refs. [46, 47], the biggest difference between the different structures that can be hosted in the system is their handednesses. That means, they describe structures that can either be left or right-handed, with all other ellipse parameters remaining the same. In terms of Stokes parameters, the different structures they generate have common S_0, S_1 and S_2, and their S_3 parameters differ by their sign while having the same amplitude (with a 5% tolerance). This is not the case here, as evidenced in the plot of the S_3 parameter, which has a different value for the localized structures A and B, but the same sign. Finally, in Ref. [80], the different vector localized structures that have been generated are a PLVS and a Group Velocity Locked Vector Soliton. Here, we predicted existence of two different PLVS solutions. This is actually a consequence of the simplifications that have been performed to derive our model: as in the classical Lugiato-Lefever model [10, 73], our fiber cavity is phase locked to the holding beam, and hence so are the localized structures.

To conclude, we have investigated a weakly birefringent fiber cavity submitted to linearly polarized optical pumping. We have shown that there exists a parameter domain in which two MI branches coexist with a homogeneous steady state. Numerical simulations of the vectorial LL model have revealed the existence of two localized structures having different Stokes parameters, i.e. different polarization properties, each one being associated with a different MI branch.

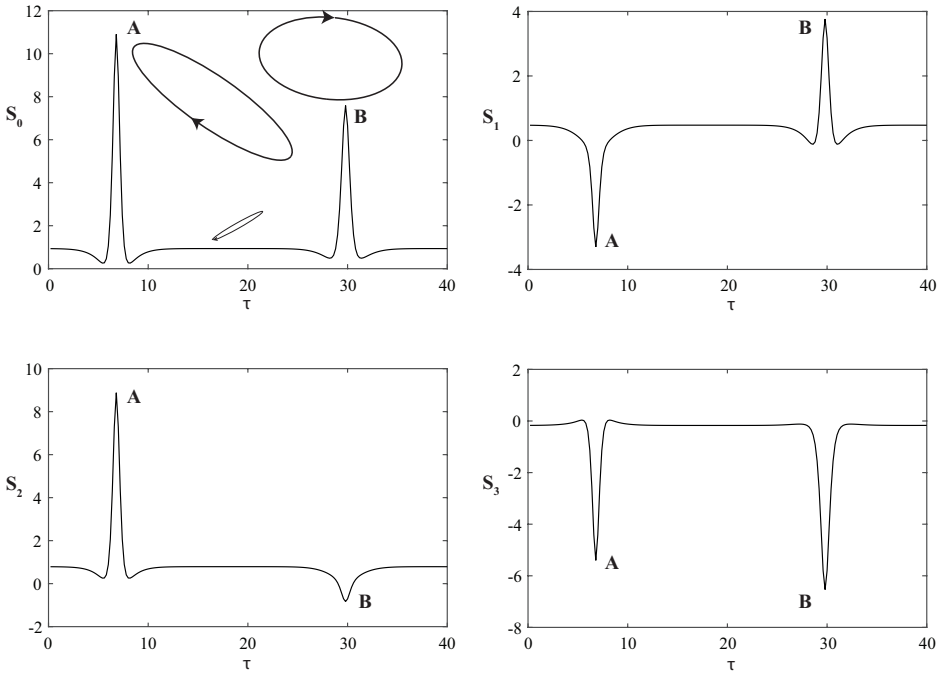

Fig. 5.5: Numerical simulation of Eqs. 5.3-5.4, after 500 units of time, expressed as a function of the Stokes parameters of the output field. On the upper-left plot (S_0), localized structures and the background have been marked with their respective polarization ellipses. The τ step has been fixed at 0.2, the time step has been fixed to 0.01. The τ integration has been performed using a second order finite difference method, whereas the time integration has been performed using a Runge-Kutta method of order 4. Parameters are $S = 2.54$, $\theta_x = 2.75$, $\beta_2 = 1$, $\theta_y = 4.3$, and $\Psi = \pi/4$.

5.3 PHOTONIC CRYSTAL FIBER CAVITIES

In this section, we investigate temporal localized structures generated in a dispersion managed PCF cavity. We first perform a linear stability analysis of Eq. 5.5, that describes the different stability regimes of this equation. Then, we will place ourselves in the vicinity of the second modulation instability point, where we perform a weakly nonlinear stability analysis of this model. Finally, localized structures and clusters are described in the last part.

5.3.1 *Linear stability analysis*

The HSSs of Eq. 5.5 describing a photonic crystal fiber cavity in which chromatic dispersion of order 2 is compensated satisfy

$$S = [1 + i(\Delta - |E_s|^2)]E_s. \tag{5.12}$$

We perform a linear stability analysis of the HSS with respect to finite frequency perturbations of the form $\exp(\lambda t + i\Omega\tau)$, this analysis yields the eigenvalues

$$\lambda = -1 + iB_3\Omega^3 \pm \sqrt{I_s^2 - (-\Delta + 2I_s + B_2\Omega^2 + B_4\Omega^4)^2} \tag{5.13}$$

where $I_s = |E_s|^2$ corresponds to the uniform intensity background of light. The system becomes unstable when one of these two eigenvalues becomes zero at a finite frequency. The system exhibits a modulational instability between the first threshold $I_{c1} = 1$, and the second threshold $I_{c2} = [2\kappa + \sqrt{\kappa^2 - 3}]/3$ with $\kappa = B_2^2/(4B_4) + \Delta$. It has been shown in [78, 81] that the fourth-order dispersion limits the region of modulation instability between these two intensity levels. Indeed, when $B_4 = 0$, the second threshold does not exist. We note also frequency degeneracy Ω_l^2 and Ω_u^2 at the first instability threshold where $\Omega_{l,u}^2 = [-B_2 \pm \sqrt{B_2^2 + 4B_4(\Delta - 2)}]/(2B_4)$. At the second threshold I_{c2}, a new critical frequency appears $\Omega^2 = -B_2/2B_4$.

In what follows, we remove the frequency degeneracy for the first threshold by choosing B_2, B_4 and Δ such as $B_2^2 + 4(\Delta - 2)B_4 = 0$. In this case, the MI zone is limited between two thresholds, the first at $I_{1c} = 1$ and the second will be at $I_{2c} = 5/3$, while the destabilized frequencies in both thresholds will be equal to $\Omega_c^2 = \Omega_l^2 = \Omega_u^2 = -B_2/(2B_4)$. Remarkably, the MI can occur in the PCF cavity only if the signs of B_2 and B_4 are opposite.

5.3.2 *Weakly nonlinear analysis*

We shall describe the nonlinear evolution of the system in the vicinity of the second instability point $I_{2c} = 5/3$. The small-amplitude inhomogeneous stationary solutions, i.e., solutions that are independent of slow t and fast τ times can be calculated analytically by employing the standard theory [82, 83]. For this purpose, we first decompose the electric field into its real and imaginary parts: $E = x_1 + ix_2$ and introduce the excess variables as $(x_1(t,\tau), x_2(t,\tau)) = (x_{1s}, x_{2s}) - (U(t,\tau), V(t,\tau))$ with x_{1s} and x_{2s} are, respectively, the real and the imaginary parts of the homogeneous solutions independent of t and τ. The homogeneous solutions of Eq. (1) obey to

$$-x_{1s} + S - x_{2s}(x_{1s}^2 + x_{2s}^2 - \Delta) = 0 \quad , \tag{5.14}$$

$$-x_{2s} + x_{1s}(x_{1s}^2 + x_{2s}^2 - \Delta) = 0 \quad . \tag{5.15}$$

Next, we introduce a small parameter $\epsilon \ll 1$ which describes the distance from the critical modulational point. We expand all variables around their critical values at the bifurcation point:

$$S = S_{2c} + \epsilon\mu_1 + \epsilon^2\mu_2 + \cdots \tag{5.16}$$

$$(U, V) = \epsilon(U_0, V_0) + \epsilon^2(U_1, V_1) + \epsilon^3(U_2, V_2) + \cdots \tag{5.17}$$

$$(x_{1s}, x_{2s}) = (a_0, b_0) + \epsilon(a_1, b_1) + \epsilon^2(a_2, b_2) + \cdots \tag{5.18}$$

We expand the time as

$$\frac{\partial}{\partial t} = \frac{\partial}{\partial T_0} + \epsilon\frac{\partial}{\partial T_1} + \epsilon^2\frac{\partial}{\partial T_2} + \cdots \tag{5.19}$$

At the leading order in ϵ we find that $a_0 = b_0 = \mu_1 = 0$. At this order, near the critical point we can approximate soltuions by a linear superposition of the corresponding critical frequencies Ω_c and Q_c

$$(U_0, V_0) = \left(1, \frac{\rho+3}{1-3\rho}\right)\tilde{W}\exp i(Q_c T_0 + \Omega_c \tau) + c.c. \tag{5.20}$$

where $c.c.$ denotes the complex conjugate and $\rho = 5/3 - \Delta$. The complex amplitude $\tilde{W}$ associated with the frequency Ω_c does not depend on the time τ, it depends only on the time T_0. The quantities a_i, b_i, U_i, and V_i can be calculated by inserting 5.16-5.19 into 5.5, 5.14, and 5.15 and equating terms with the same powers of ϵ. At order ϵ^2, the solvavility condition imposes that $a_1 = b_1 = \mu_1 = 0$. The application of

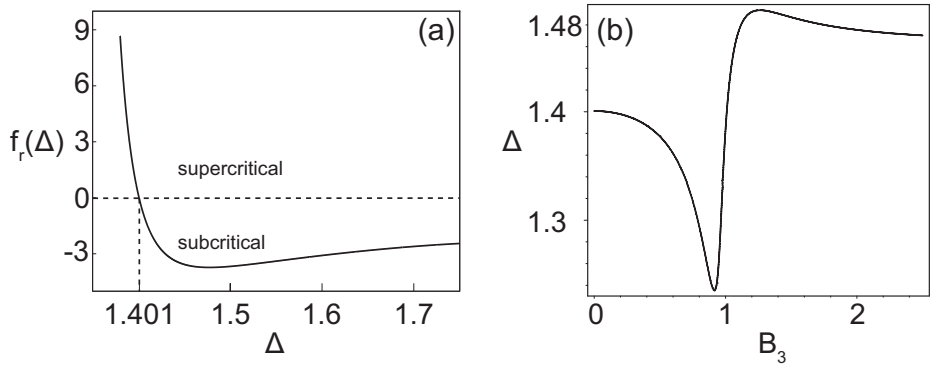

Fig. 5.6: The threshold associated with the transition from super- to sub-critical modulational instability is plotted (a) as a function of the detuning parameter Δ for $B_3 = 0$; (b) in the plane (B_3, Δ). Others parameters are $B_4 = 0.5$, and $B_2 = \sqrt{4B_4(2-\Delta)}$

the solvability condition to the order ϵ^3 brings an amplitude equation for the unstable mode. In terms of the unscaled amplitudes (W=ϵ $\tilde{W}$+ $\cdots$), we obtain

$$\frac{\partial W}{\partial t} = \mu W + (f_r + i f_i) W |W|^2 \tag{5.21}$$

Where

$$\mu = \frac{S - S_{2c}}{(3\rho+1))(\rho+3)S_c} \text{ with } S_{2c} = \sqrt{\frac{5}{3}}\sqrt{1+\rho^2} \tag{5.22}$$

$$f_r = \frac{ac+bd}{c^2+d^2} \text{ and } f_i = \frac{bc-ad}{c^2+d^2} \tag{5.23}$$

where the coefficients a, b, c and d are expressed in term of the detuning parameter $\Delta = 5/3 - \rho$

$$
\begin{aligned}
a &= -4(\Delta-2)(\alpha_1+\alpha_2)+\alpha_3 \\
\alpha_1 &= 59049\Delta^7 - 798255\Delta^6 + 4417983\Delta^5 - 13345641\Delta^4 \\
\alpha_2 &= 24735807\Delta^3 - 29605896\Delta^2 + 21969258\Delta - 7708940 \\
\alpha_3 &= 600(486\Delta^6 - 5508\Delta^5 + 24435\Delta^4 - 57654\Delta^3 + 82686\Delta^2 - 73156\Delta + 30792)B_3\Omega^3 \\
b &= -60(3\Delta-4)(243\Delta^5 - 2268\Delta^4 + 7398\Delta^3 - 11412\Delta^2 + 11040\Delta - 7304)B_3\Omega^3 \\
c &= 3(3\Delta^2 - 20\Delta + 28)(3\Delta-4)^2 c_1 \\
c_1 &= (9\Delta^2 - 30\Delta + 34)^2(100(B_3\Omega^3)^2 - 81\Delta^2 + 348\Delta - 372) \\
d &= -60(\Delta-2)(3\Delta-14)(3\Delta-4)^2(9\Delta^2 - 30\Delta + 34)^2 B_3\Omega^3
\end{aligned}
$$

When $f_r(\Delta) < 0$, the modulational instability is subcritical. In this case, it is necessary to retain the fifth order in ϵ, since equation (5.21) loses its meaning. Thus, if $f_r(\Delta) > 0$, the modulational instability is supercritical, leading to stable small amplitude temporal structures. The parameter regime where the bifurcation is supercritical is plotted in Fig. 5.6a. The transition from super- to sub-critical modulationnal instability is explicitly given by $f_r = 0$. This condition corresponds to the threshold of the emergence of temporal cavity solitons that we shall discuss is the next section. The dependence of the threshold as a function of the third order dispersion coefficient and of the detuning parameter is shown in Fig. 5.6b. Note, however, that the third order dispersion affects the threshold of the modulational instability as well. In the supercritical case where $f_r(\Delta) > 0$, we seek for solutions of Eq. 5.21 in the form of $W = A\exp(iRt)$. Inserting this ansatz in Eq. 5.21. The stationary solutions are

$$A_s = 0,\ A_s = \pm\sqrt{\frac{-\mu}{f_r}} \text{ and } R = \frac{\mu f_i}{f_r} \tag{5.24}$$

The third order dispersion breaks the symmetry $(\tau, -\tau)$. This breaking symmetry induces a motion of temporal structures and the linear and nonlinear corrections to their velocity are

$$v = v_l + v_{nl} \text{ with } v_l = \frac{\partial \lambda_i}{\partial \Omega} \text{ and } v_{nl} = \frac{\partial R}{\partial \Omega} \tag{5.25}$$

In terms of the dynamical parameters the linear and the nonlinear velocities are

$$v_l = 3B_3\Omega^2 \text{ and } v_{nl} = \frac{\mu}{f_r}\frac{\partial f_i}{\partial \Omega} \tag{5.26}$$

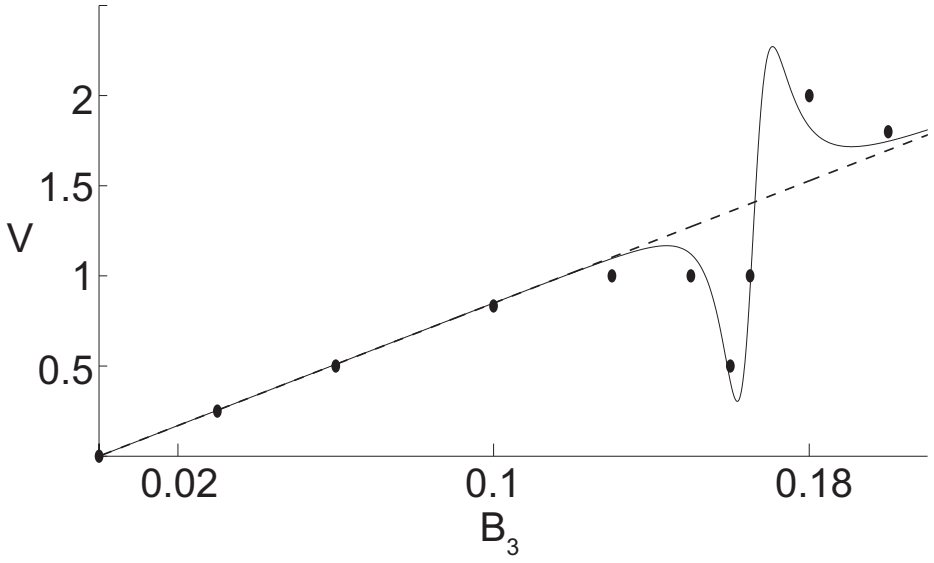

Fig. 5.7: Linear velocity of the periodic structure and its nonlinear correction with respect to B_3. Dashed curve denotes the linear velocity. The velocity with its nonlinear correction (Eq. 5.25) is plotted by a solid line. The velocity obtained from direct numerical simulations of Eq. (2) are indicated by circles. Parameters are $S = 1.4307$, $\epsilon^2 = 0.006$, $\Delta = 1.2$, $B_4 = 0.1$, and $B_2 = -0.5657$.

The velocity as a function of the third order dispersion coefficient (Eq. 5.26) is plotted in Fig. 5.7. The velocity of moving temporal structures calculated through numerical simulations of the model Eq. 5.5 is in good agreement with the one estimated from the above analysis.

5.3.3 *Moving localized structures*

In this section, we are interested in the situation where the bifurcation towards modulational instability appears subcritically. In the absence of the third order dispersion, the typical bifurcation diagram is shown in Fig. 5.8. In the domain, denoted by L, the system exhibits a coexistence between two stable solutions: the homogeneous steady state (uniform background) and the temporal train of periodic pulses that emerges from subcritical modulational instability. Temporal dark cavity solitons, connecting the HSS and a branch of periodic solutions, are found in a well-defined region of parameters called a pinning zone denoted L in Fig. 5.8. It has been shown that temporal cavity solitons exhibit a homoclinic snaking type of bifurcation [84]. Depending on the initial condition used, a single dip, or multiple dips in the intensity profile can be generated in direct numerical simulations of Eq. 5.5. Examples of stationary temporal dark cavity solitons involving one to six dips are shown in Fig. 5.9. They are obtained from the same values of parameters and they are characterized by an oscillating exponentially decaying tails.

Let us now investigate the effect of third order dispersion on the dark cavity solitons. As we have already mentioned, this effect breaks the reflexion symmetry ($\tau \rightarrow -\tau$) of temporal cavity solitons emerging from subcritical bifurcation point. This symmetry breaking induces a drift of the temporal cavity solitons with a constant velocity. Examples of drifiting temporal dark cavity solitons are shown in τ-t maps of the Fig. 5.10.

5.4 CONCLUSIONS

In this chapter, we have investigated nonlinear fiber resonators, to find phenomena similar to the ones developed in other chapters.

A link with chapter 3 has been made in the case of a weakly birefringent fiber. We derived a model describing the spatio-temporal evolution of light in the approximations of a good cavity, dispersion length much longer than the cavity length, and by neglecting four-wave mixing. In that context, we perfromed a linear stability analysis of the homogeneous steady states. This analysis revealed a region in which a homo-

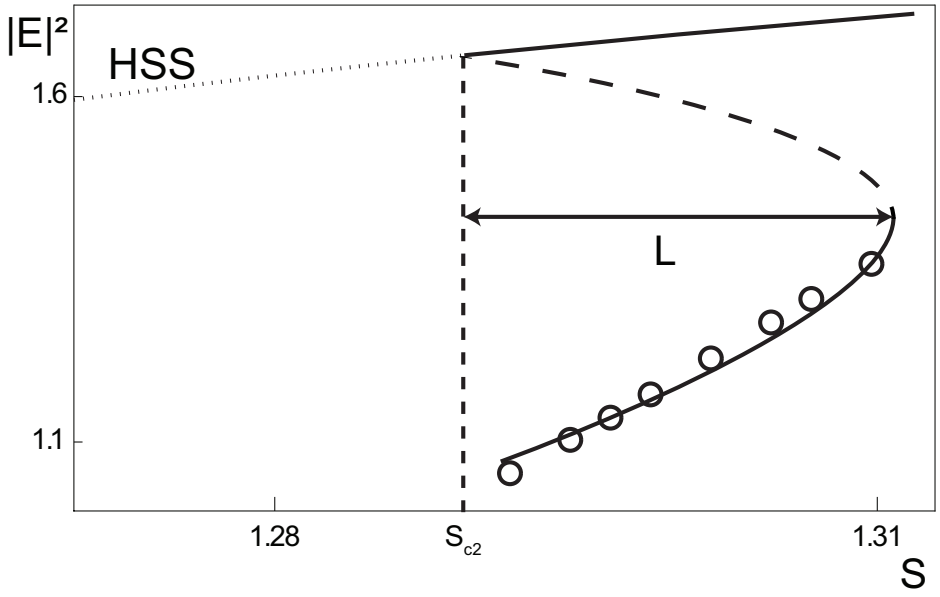

Fig. 5.8: Bifurcation diagram associated with the temporal train of periodic pulses that emerges from subcritical modulational instability. Parameter are $B_4 = 0.1$, $B_2 = -0.3347$, $B_3 = 0$, $\Delta = 1.72$, The full (dashed) curve indicates stable (unstable) solutions. The open circles represent the numerical values of the minimum intensity of the temporal train of periodic pulses.

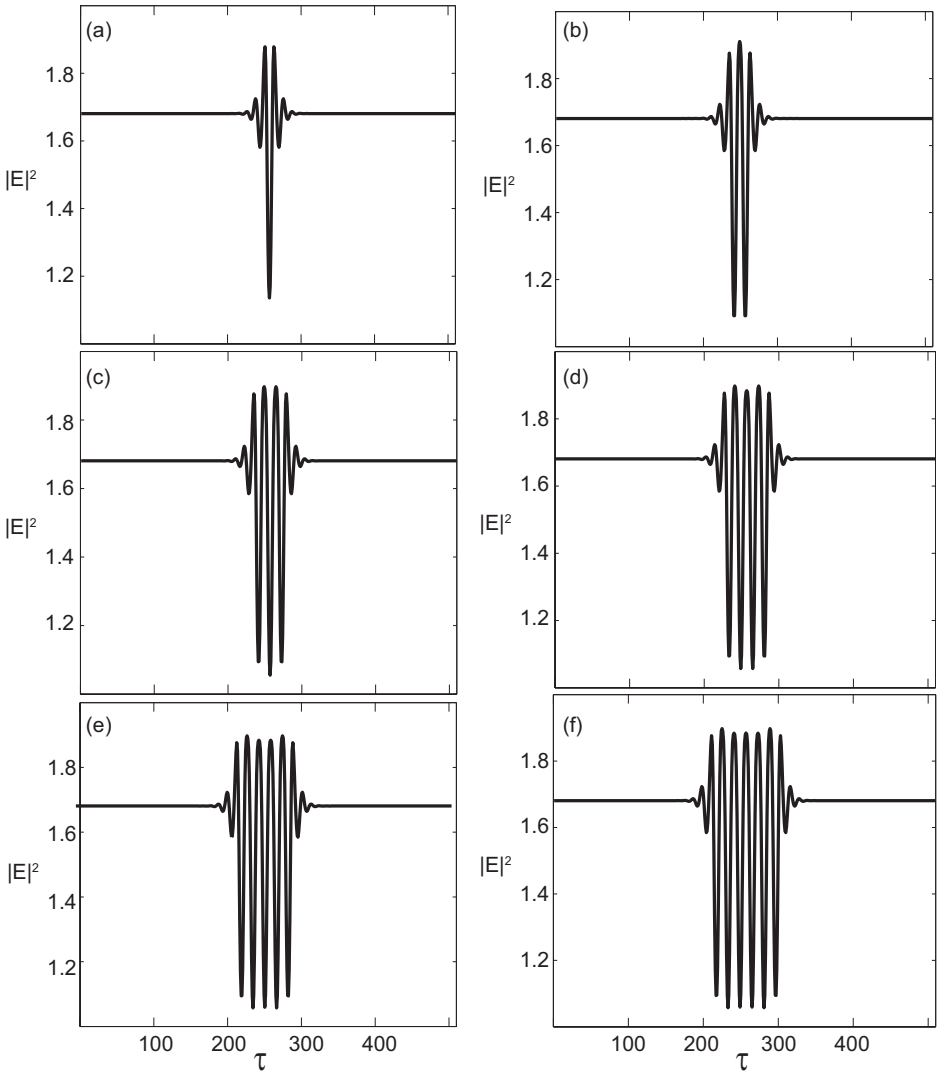

Fig. 5.9: Stationary temporal dark cavity solitons with up to 6 dips. (a)-(f) corresponding to 1-6 dips or holes in the insensity profiles, respectively. Parameters are the same as figure 5.7 with $B_3 = 0$.

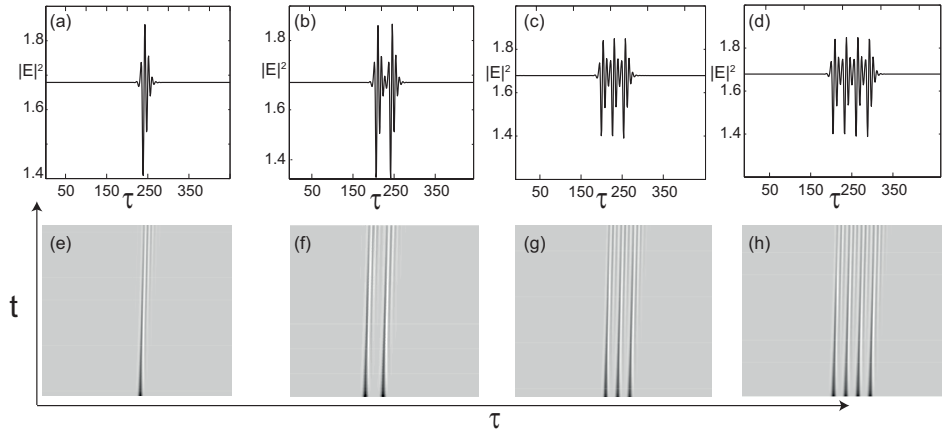

Fig. 5.10: Moving temporal dark cavity solitons with up to 4 dips. (a)-(d) are the intensity profiles in the PCF cavity at $t = 0$, whereas (e)-(h) are space-time maps in the (t,τ) plane. Parameters are the same as figure 5.7 with $B_3 = 0.1$.

geneous steady state coexists with two different modulation instabilities. Numerical simulations in this parameter range revealed a bistability between two different patterns. Numerical simulations also revealed the possibility of generating two different kinds of localized structures in that system.

A motion of localized structures due to a symmetry breaking has been developed in the second part of this chapter. Note however that the symmetry breaking phenomenon is fundamentally different to the one developed in chapter 4, as the symmetry breaking in that system happens in the space variable, whereas the one studied in chapter 4 breaks the time symmetry. We investigated this symmetry breaking in the vicinity of the second modulational instability point, where we computed the velocity of localized structures induced by the aforementioned symmetry breaking, in the supercritical regime. When the modulational instability appears subcritically, we found moving temporal dark solitons that can be either isolated or organized in clusters.

6 CONCLUSIONS AND PERSPECTIVES

6.1 CONCLUSIONS

In chapter 2, we have built an experimental setup, and we have investigated the formation of two-dimensional localized structures in the transverse section of a 80μm diameter VCSEL. Bistability corresponding to spontaneous appearance and disappearing of a localized structure have been observed, as a function of optical injection power, and as a function of VCSEL current. Oscillating tails of the localized structures have also been observed. Spontaneous appearance and disappearance of two localized structures have also been observed, which is a manifestation of multistability.

All of these measurements have been performed while the linearly polarized optical injection had its direction matching the one in which the VCSEL spontaneously lases in while being pumped close to its current threshold.

Considering a model for the specific case of a VCSEL injection-locked in polarization and frequency in the vicinity of the nascent bistability, we have carried out nonlinear perturbative analysis and obtained a modified Swift-Hohenberg equation. Based on this equation, we have shown that, in one transverse dimension, stationary-cavity solitons exhibit a clustering behavior in the pinning range of parameters where spatially homogeneous and periodic solutions are both linearly stable. In this range, we have constructed a snaking bifurcation diagram associated with localized structures having an odd, or an even number of peaks.

In chapter 3, we have extended our experimental setup for generation and characterization of vector localized structures in the transverse section of a broad area VCSEL. Bistability corresponding to the spontaneous appearance and disappearance of a localized structure has been observed, as a function of optical injection power. The Stokes parameters of these localized structures have been measured, for orientations of the optical injection linear polarization varying in a 90° span. This analysis has revealed that localized structures acquired ellipticity. These structures hence can be classified as vector localized structures.

A model for describing the polarization dynamics of localized structures in a broad area VCSEL has been implemented: the VCSEL spin-flip model. Based on this model, we have performed a linear stability analysis. That is, we have investi-

gated the dependance of the homogeneous steady states of the system and their linear stability as a function of optical injection strength E_I, and of the frequency detuning between optical injection and the VCSEL frequency $\Delta\omega$. This linear stability analysis has revealed a bistable region of coexistence between a Turing unstable branch, and a homogeneous stable branch. Localized structures have been numerically found in this regime. Linear stability analysis of the VCSEL spin-flip model in the plane optical injection strength-frequency detuning between optical injection and VCSEL cavity has led to the discovery of a tristable region.

Numerical simulations of the VCSEL spin-flip model have been compared with experimental data. There is a good agreement between numerical and experimental data. A quite large circularly polarized component in the polarization state of localized structures, described by the s_3 parameter, has been both measured and computed to be as high as $s_3 \approx 0.2$. Using localized structures in broad-area VCSELs that can be switched on and off independently as pixels for information processing [25] constitutes a bitmap. Considering the Stokes parameters of the vector localized structures demonstrated here, one would potentially create a colormap instead of a bitmap, i.e. each pixel contains information in a 3-parameter space (s_1, s_2, s_3) that easily can be translated into a color code. In such a way, the density of information can be dramatically increased.

In chapter 4, we have considered a VCSEL submitted to optical injection and delayed optical feedback. To mathematically describe the evolution of such a system, we have added a delayed term in the mean-field model, as well as in the reduced model, the modified Swift-Hohenberg equation with a delay term.

In the framework of the modified Swift-Hohenberg equation with a delay term, we have performed a linear stability analysis and investigated the Turing pattern formation in the presence of delay, in the monostable and bistable regimes. Numerical simulations have shown the presence of stationary localized structures, as well as moving localized structures. The motion of those localized structures is then linked with a drift instability. The threshold for this instability, and the speed at which it occurs are derived. These quantities depend only on the feedback parameters.

In the more general framework of the VCSEL mean field model, we also numerically and theoretically investigated the motion of localized structures. The motion threshold and speed of the localized structures are found to depend not only on the feedback parameters, but also on the decay rate for charge carriers, as well as on the phase of the optical feedback. We provide analytical expressions for both the threshold of localized structures drift instability, and the velocity of this motion.

Finally, in chapter 5, we have investigated nonlinear fiber resonators, to find phenomena similar to the ones developed in other chapters. A link with chapter 3 has been made in the case of a lowly birefringent fiber. We have derived a model de-

scribing the spatio-temporal evolution of light in the approximations of a good cavity, dispersion length much longer than the cavity length, and by neglecting four-wave mixing. In that context, we have performed a linear stability analysis of the homogeneous steady states. This analysis has revealed a region in which a homogeneous steady state coexists with two different modulation instabilities. Numerical simulations in this parameter range have revealed a bistability between two different patterns, as well as the possibility of generating two different kinds of localized structures in that system.

A motion of localized structures due to a symmetry breaking has been developed in the second part of this chapter. Note however that the symmetry breaking phenomenon is fundamentally different to the one developed in chapter 4, as the symmetry breaking in that system happens in the space variable, whereas the one studied in chapter 4 breaks the time symmetry. We have investigated this symmetry breaking in the vicinity of the second modulational instability point, where we have computed the velocity of localized structures induced by the aforementioned symmetry breaking, in the supercritical regime. When the modulational instability appears subcritically, we have found moving temporal dark solitons that can be either isolated or organized in clusters.

6.2 PERSPECTIVES

6.2.1 *Polarization properties of localized structures in VCSELs*

Under appropriate conditions, polarization represents a degree of freedom that can be exploited in order to create new types of localized structures. The study of temporal localized structures in a low birefringence fiber in chapter 5 has been performed in that spirit. Extensive mappings of the spin-flip VCSEL model are currently under investigations, to find tristable regimes suitable for localized structure generation of different types, qualitatively similar to the temporal ones described in the case of a low birefringence fiber.

This linear stability analysis has also suggested the presence of dark localized structures in the framework of the VCSEL spin-flip model. Their numerical, analytical, and numerical demonstration would be of considerable interest. Indeed, to the best of our knowledge, dark localized structures have never been observed in a spatially extended system.

6.2.2 ***Delay-induced motion of transverse localized structures***

The motion of localized structures described in chapter 4 is currently under experimental investigation. Promising results have already been obtained, even though no linear motion of localized structures has been observed so far. Instead of being set into linear motion, the localized structures submitted to an optical delayed feedback begin to oscillate around the place they have been generated at. This phenomenon is currently under theoretical investigations. A promising lead for explaining this phenomenon consists of considering the localized structure as being *trapped* in a defect at the surface of the emission surface of the VCSEL. This defect can be modelled as a harmonic potential, in which the structure can move the very same way a pendulum does around its equilibrium position.

BIBLIOGRAPHY

[1] I. Prigogine and R. Lefever, "Symmetry breaking instabilities in dissipative systems. ii," *The Journal of Chemical Physics*, vol. 48, no. 4, pp. 1695–1700, 1968.

[2] P. Glansdorff and I. Prigogine, *Thermodynamic Theory of Structure, Stability and Fluctuations*. Wiley, 1971.

[3] A. M. Turing, "The chemical basis of morphogenesis," *Philos. Trans. R. Soc. Lond. B. Biol. Sci.*, vol. 237, no. 641, pp. 37–72, 1952.

[4] H. Bénard, *Les tourbillons cellulaires dans une nappe liquide propageant de la chaleur par convection, en régime permanent*. PhD thesis, Université de Paris, 1901.

[5] V. Castets, E. Dulos, J. Boissonade, and P. De Kepper, "Experimental evidence of a sustained standing turing-type nonequilibrium chemical pattern," *Phys. Rev. Lett.*, vol. 64, pp. 2953–2956, Jun 1990.

[6] Q. Ouyang and H. L. Swinney, "Transition from a uniform state to hexagonal and striped turing patterns," *Nature*, vol. 352, pp. 610–612, 08 1991.

[7] M. Tlidi, K. Staliunas, K. Panajotov, A. G. Vladimirov, and M. G. Clerc, "Localized structures in dissipative media: from optics to plant ecology," *Philosophical Transactions of the Royal Society of London A: Mathematical, Physical and Engineering Sciences*, vol. 372, no. 2027, 2014.

[8] D. W. McLaughlin, J. V. Moloney, and A. C. Newell, "New class of instabilities in passive optical cavities," *Phys. Rev. Lett.*, vol. 54, pp. 681–684, Feb 1985.

[9] D. W. McLaughlin, J. V. Moloney, and A. C. Newell, "Solitary waves as fixed points of infinite-dimensional maps in an optical bistable ring cavity," *Phys. Rev. Lett.*, vol. 51, p. 75, Jul 1983.

[10] L. A. Lugiato and R. Lefever, "Spatial dissipative structures in passive optical systems," *Phys. Rev. Lett.*, vol. 58, pp. 2209–2211, May 1987.

[11] M. Tlidi, Y. Gandica, G. Sonnino, E. Averlant, and K. Panajotov, "Self-replicating spots in the brusselator model and extreme events in the one-dimensional case with delay," *Entropy*, vol. 18, no. 3, p. 64, 2016.

[12] M. Tlidi, P. Mandel, and R. Lefever, "Localized structures and localized patterns in optical bistability," *Phys. Rev. Lett.*, vol. 73, p. 640, Aug 1994.

[13] A. J. Scroggie, W. J. Firth, G. S. McDonald, M. Tlidi, R. Lefever, and L. A. Lugiato, "Pattern formation in a passive kerr cavity," *Chaos, Solitons and Fractals*, vol. 4, no. 8, p. 1323, 1994.

[14] M. G. Clerc, A. Petrossian, and S. Residori, "Bouncing localized structures in a liquid-crystal light-valve experiment," *Phys. Rev. E*, vol. 71, p. 015205, Jan 2005.

[15] S. Longhi, "Spatial solitary waves and patterns in type ii second-harmonic generation," *Opt. Lett.*, vol. 23, pp. 346–348, Mar 1998.

[16] F. Leo, S. Coen, P. Kockaert, S.-P. Gorza, P. Emplit, and M. Haelterman, "Temporal cavity solitons in one-dimensional kerr media as bits in an all-optical buffer," *Nat Photon*, vol. 4, p. 471, 07 2010.

[17] S. Barbay, R. Kuszelewicz, and J. R. Tredicce, "Cavity solitons in vcsel devices," *Advances in Optical Technologies*, vol. 2011, p. 628761, 2011.

[18] L. Lugiato, F. Prati, G. Tissoni, M. Brambilla, S. Barland, M. Giudici, and J. Tredicce, *Dissipative Solitons: from optics to biology and Medicine*, vol. 751 of *Lecture notes in physics*, ch. Cavity Solitons in Semiconductor Devices, pp. 1–42. Springer Berlin Heidelberg, 2008.

[19] T. Ackemann, W. J. Firth, and G.-L. Oppo, "Fundamentals and applications of spatial dissipative solitons in photonic devices," in *Advances In Atomic, Molecular, and Optical Physics* (P. R. B. E. Arimondo and C. C. Lin, eds.), vol. 57 of *Advances In Atomic, Molecular, and Optical Physics*, ch. 6, p. 323, Academic Press, 2009.

[20] R. Kuszelewicz, S. Barbay, G. Tissoni, and G. Almuneau, "Editorial on dissipative optical solitons," *Eur. Phys. J. D*, vol. 59, no. 1, p. 1, 2010.

[21] M. Brambilla, L. A. Lugiato, F. Prati, L. Spinelli, and W. J. Firth, "Spatial soliton pixels in semiconductor devices," *Phys. Rev. Lett.*, vol. 79, p. 2042, Sep 1997.

[22] D. Michaelis, U. Peschel, and F. Lederer, "Multistable localized structures and superlattices in semiconductor optical resonators," *Phys. Rev. A*, vol. 56, pp. R3366–R3369, Nov 1997.

[23] L. Spinelli, G. Tissoni, M. Brambilla, F. Prati, and L. A. Lugiato, "Spatial solitons in semiconductor microcavities," *Phys. Rev. A*, vol. 58, p. 2542, Sep 1998.

[24] V. B. Taranenko, I. Ganne, R. J. Kuszelewicz, and C. O. Weiss, “Patterns and localized structures in bistable semiconductor resonators,” *Phys. Rev. A*, vol. 61, p. 063818, May 2000.

[25] S. Barland, J. R. Tredicce, M. Brambilla, L. A. Lugiato, S. Balle, M. Giudici, T. Maggipinto, L. Spinelli, G. Tissoni, T. Knödl, *et al.*, “Cavity solitons as pixels in semiconductor microcavities,” *Nature*, vol. 419, no. 6908, p. 699, 2002.

[26] M. Grabherr, M. Miller, R. Jager, R. Michalzik, U. Martin, H. J. Unold, and K. J. Ebeling, “High-power vcsels: single devices and densely packed 2-d-arrays,” *Selected Topics in Quantum Electronics, IEEE Journal of*, vol. 5, no. 3, p. 495, 1999.

[27] M. Schulz-Ruhtenberg, Y. Tanguy, R. Jäger, and T. Ackemann, “Length scales and polarization properties of annular standing waves in circular broad-area vertical-cavity surface-emitting lasers,” *Applied Physics B*, vol. 97, no. 2, pp. 397–403, 2009.

[28] X. Hachair, F. Pedaci, E. Caboche, S. Barland, M. Giudici, J. R. Tredicce, F. Prati, G. Tissoni, R. Kheradmand, L. A. Lugiato, I. Protsenko, and M. Brambilla, “Cavity solitons in a driven vcsel above threshold,” *Selected Topics in Quantum Electronics, IEEE Journal of*, vol. 12, no. 3, pp. 339–351, 2006.

[29] M. Bache, F. Prati, G. Tissoni, R. Kheradmand, L. A. Lugiato, I. Protsenko, and M. Brambilla, “Cavity soliton laser based on vcsel with saturable absorber,” *Applied Physics B*, vol. 81, no. 7, p. 913, 2005.

[30] S. V. Fedorov, N. N. Rozanov, and A. N. Shatsev, “Two-dimensional solitons in b-class lasers with saturable absorption,” *Optics and Spectroscopy*, vol. 102, no. 3, pp. 449–455, 2007.

[31] F. Prati, P. Caccia, G. Tissoni, L. Lugiato, K. Mahmoud Aghdami, and H. Tajalli, “Effects of carrier radiative recombination on a vcsel-based cavity soliton laser,” *Applied Physics B*, vol. 88, no. 3, pp. 405–410, 2007.

[32] T. Elsass, K. Gauthron, G. Beaudoin, I. Sagnes, R. Kuszelewicz, and S. Barbay, “Fast manipulation of laser localized structures in a monolithic vertical cavity with saturable absorber,” *Applied Physics B*, vol. 98, no. 2-3, pp. 327–331, 2010.

[33] Y. Tanguy, T. Ackemann, W. J. Firth, and R. Jäger, “Realization of a semiconductor-based cavity soliton laser,” *Phys. Rev. Lett.*, vol. 100, p. 013907, Jan 2008.

[34] N. Radwell and T. Ackemann, "Characteristics of laser cavity solitons in a vertical-cavity surface-emitting laser with feedback from a volume bragg grating," *IEEE Journ. Quant. Elec.*, vol. 45, no. 11, p. 1388, 2009.

[35] P. Genevet, S. Barland, M. Giudici, and J. R. Tredicce, "Cavity soliton laser based on mutually coupled semiconductor microresonators," *Phys. Rev. Lett.*, vol. 101, p. 123905, Sep 2008.

[36] S. Barbay, X. Hachair, T. Elsass, I. Sagnes, and R. Kuszelewicz, "Homoclinic snaking in a semiconductor-based optical system," *Phys. Rev. Lett.*, vol. 101, p. 253902, Dec 2008.

[37] F. Pedaci, S. Barland, E. Caboche, P. Genevet, M. Giudici, J. R. Tredicce, T. Ackemann, A. J. Scroggie, W. J. Firth, G. L. Oppo, G. Tissoni, and R. Jäger, "All-optical delay line using semiconductor cavity solitons," *Appl. Phys. Lett.*, vol. 92, no. 1, p. 011101, 2008.

[38] F. Pedaci, G. Tissoni, S. Barland, M. Giudici, and J. Tredicce, "Mapping local defects of extended media using localized structures," *Appl. Phys. Lett.*, vol. 93, no. 11, p. 111104, 2008.

[39] W. Lange, A. Aumann, T. Ackemann, and E. Büthe, "Polarization patterns in alkaline vapours," *Quantum and Semiclassical Optics: Journal of the European Optical Society Part B*, vol. 10, no. 1, p. R23, 1998.

[40] M. Hoyuelos, P. Colet, M. San Miguel, and D. Walgraef, "Polarization patterns in Kerr media," *Phys. Rev. E*, vol. 58, pp. 2992–3007, Sep 1998.

[41] V. J. Sánchez-Morcillo, I. Pérez-Arjona, F. Silva, G. J. de Valcárcel, and E. Roldán, "Vectorial Kerr-cavity solitons," *Opt. Lett.*, vol. 25, pp. 957–959, Jul 2000.

[42] M. San Miguel, Q. Feng, and J. V. Moloney, "Light-polarization dynamics in surface-emitting semiconductor lasers," *Phys. Rev. A*, vol. 52, pp. 1728–1739, Aug 1995.

[43] X. Hachair, G. Tissoni, H. Thienpont, and K. Panajotov, "Linearly polarized bistable localized structure in medium-size vertical-cavity surface-emitting lasers," *Phys. Rev. A*, vol. 79, p. 011801, Jan 2009.

[44] M. Haelterman and A. Sheppard, "Polarization instability, multistability and transverse localized structures in kerr media," *Chaos, Solitons & Fractals*, vol. 4, no. 8-9, pp. 1731 – 1743, 1994. Special Issue: Nonlinear Optical Structures, Patterns, Chaos.

[45] M. Haelterman and A. P. Sheppard, "Vector soliton associated with polarization modulational instability in the normal-dispersion regime," *Phys. Rev. E*, vol. 49, pp. 3389–3399, Apr 1994.

[46] B. C. Collings, S. T. Cundiff, N. N. Akhmediev, J. M. Soto-Crespo, K. Bergman, and W. H. Knox, "Polarization-locked temporal vector solitons in a fiber laser: experiment," *J. Opt. Soc. Am. B*, vol. 17, pp. 354–365, Mar 2000.

[47] J. M. Soto-Crespo, N. N. Akhmediev, B. C. Collings, S. T. Cundiff, K. Bergman, and W. H. Knox, "Polarization-locked temporal vector solitons in a fiber laser: theory," *J. Opt. Soc. Am. B*, vol. 17, pp. 366–372, Mar 2000.

[48] C. Mou, S. Sergeyev, A. Rozhin, and S. Turistyn, "All-fiber polarization locked vector soliton laser using carbon nanotubes," *Opt. Lett.*, vol. 36, pp. 3831–3833, Oct 2011.

[49] D. Y. Tang, H. Zhang, L. M. Zhao, and X. Wu, "Observation of high-order polarization-locked vector solitons in a fiber laser," *Phys. Rev. Lett.*, vol. 101, p. 153904, Oct 2008.

[50] G. Geelen, "Internship report," tech. rep., Vrije Universiteit Brussel and Telecom Saint Etienne, 2014.

[51] G. H. M. van Tartwijk and D. Lenstra, "Semiconductor lasers with optical injection and feedback," *Quantum and Semiclassical Optics: Journal of the European Optical Society Part B*, vol. 7, no. 2, p. 87, 1995.

[52] V. Odent, M. Taki, and E. Louvergneaux, "Experimental evidence of dissipative spatial solitons in an optical passive kerr cavity," *New Journal of Physics*, vol. 13, no. 11, p. 113026, 2011.

[53] B. Schäpers, M. Feldmann, T. Ackemann, and W. Lange, "Interaction of localized structures in an optical pattern-forming system," *Phys. Rev. Lett.*, vol. 85, p. 748, Jul 2000.

[54] P. L. Ramazza, E. Benkler, U. Bortolozzo, S. Boccaletti, S. Ducci, and F. T. Arecchi, "Tailoring the profile and interactions of optical localized structures," *Phys. Rev. E*, vol. 65, p. 066204, Jun 2002.

[55] M. Tlidi, M. Georgiou, and P. Mandel, "Transverse patterns in nascent optical bistability," *Phys. Rev. A*, vol. 48, pp. 4605–4609, Dec 1993.

[56] A. G. Vladimirov, R. Lefever, and M. Tlidi, "Relative stability of multipeak localized patterns of cavity solitons," *Phys. Rev. A*, vol. 84, p. 043848, Oct 2011.

[57] G. Kozyreff and M. Tlidi, "Optical patterns with different wavelengths," *Phys. Rev. E*, vol. 69, p. 066202, Jun 2004.

[58] G. Kozyreff and M. Tlidi, "Nonvariational real swift-hohenberg equation for biological, chemical, and optical systems," *Chaos: An Interdisciplinary Journal of Nonlinear Science*, vol. 17, no. 3, pp. –, 2007.

[59] J. Swift and P. C. Hohenberg, "Hydrodynamic fluctuations at the convective instability," *Phys. Rev. A*, vol. 15, pp. 319–328, Jan 1977.

[60] J. Lega, J. V. Moloney, and A. C. Newell, "Swift-hohenberg equation for lasers," *Phys. Rev. Lett.*, vol. 73, pp. 2978–2981, Nov 1994.

[61] Y. Pomeau, "Front motion, metastability and subcritical bifurcations in hydrodynamics," *Physica D: Nonlinear Phenomena*, vol. 23, pp. 3 – 11, 1986.

[62] M. Tlidi, E. Averlant, A. Vladimirov, and K. Panajotov, "Delay feedback induces a spontaneous motion of two-dimensional cavity solitons in driven semiconductor microcavities," *Phys. Rev. A*, vol. 86, p. 033822, Sep 2012.

[63] M. Born and E. Wolf, *Principles of optics: electromagnetic theory of propagation, interference and diffraction of light*. Cambridge, UK: Cambridge University Press, seventh ed., 2000.

[64] J. Martin-Regalado, F. Prati, M. San Miguel, and N. Abraham, "Polarization properties of vertical-cavity surface-emitting lasers," *Quantum Electronics, IEEE Journal of*, vol. 33, pp. 765–783, May 1997.

[65] T. Erneux, *Applied delay Differential Equations*, vol. 3 of *Surveys and tutorials in the applied mathematical sciences*. Springer Verlag New York, 2009.

[66] M. Tlidi, A. G. Vladimirov, D. Pieroux, and D. Turaev, "Spontaneous motion of cavity solitons induced by a delayed feedback," *Phys. Rev. Lett.*, vol. 103, p. 103904, Sep 2009.

[67] K. Panajotov and M. Tlidi, "Spontaneous motion of cavity solitons in vertical-cavity lasers subject to optical injection and to delayed feedback," *The European Physical Journal D*, vol. 59, no. 1, p. 67, 2010.

[68] S. V. Gurevich and R. Friedrich, "Instabilities of localized structures in dissipative systems with delayed feedback," *Phys. Rev. Lett.*, vol. 110, p. 014101, Jan 2013.

[69] A. Pimenov, A. G. Vladimirov, S. V. Gurevich, K. Panajotov, G. Huyet, and M. Tlidi, "Delayed feedback control of self-mobile cavity solitons," *Phys. Rev. A*, vol. 88, p. 053830, Nov 2013.

[70] S. Residori, A. Petrossian, T. Nagaya, and M. Clerc, “Localized structures and their dynamics in a liquid crystal light valve with optical feedback,” *Journal of Optics B: Quantum and Semiclassical Optics*, vol. 6, p. S169, 2004.

[71] N. N. Rozanov, “Kinetics of a solid-state laser with an additional moving mirror,” *Soviet Journal of Quantum Electronics*, vol. 4, pp. 1191–1193, 1975.

[72] R. Lang and K. Kobayashi, “External optical feedback effects on semiconductor injection laser properties,” *Quantum Electronics, IEEE Journal of*, vol. 16, pp. 347–355, 1980.

[73] M. Haelterman, S. Trillo, and S. Wabnitz, “Dissipative modulation instability in a nonlinear dispersive ring cavity,” *Optics Communications*, vol. 91, pp. 401 – 407, 1992.

[74] P. Kockaert, P. Tassin, G. Van der Sande, I. Veretennicoff, and M. Tlidi, “Negative diffraction pattern dynamics in nonlinear cavities with left-handed materials,” *Phys. Rev. A*, vol. 74, p. 033822, 2006.

[75] Y. K. Chembo and C. R. Menyuk, “Spatiotemporal lugiato-lefever formalism for kerr-comb generation in whispering-gallery-mode resonators,” *Phys. Rev. A*, vol. 87, p. 053852, May 2013.

[76] A. Coillet, J. Dudley, G. Genty, L. Larger, and Y. K. Chembo, “Optical rogue waves in whispering-gallery-mode resonators,” *Phys. Rev. A*, vol. 89, p. 013835, 2014.

[77] P. Russell, “Photonic crystal fibers,” *Science*, vol. 299, pp. 358–362, 2003.

[78] M. Tlidi, A. Mussot, E. Louvergneaux, G. Kozyreff, A. G. Vladimirov, and M. Taki, “Control and removal of modulational instabilities in low-dispersion photonic crystal fiber cavities,” *Opt. Lett.*, vol. 32, no. 6, pp. 662–664, 2007.

[79] S. V. Sergeyev, C. Mou, E. G. Turitsyna, A. Rozhin, S. K. Turitsyn, and K. Blow, “Spiral attractor created by vector solitons,” *Light Sci Appl*, vol. 3, p. e131, 2014.

[80] H. Zhang, D. Y. Tang, L. M. Zhao, X. Wu, and H. Tam, “Dissipative vector solitons in a dispersion-managed cavity fiber laser with net positive cavity dispersion,” *Opt. Express*, vol. 17, no. 2, pp. 455–460, 2009.

[81] L. Bahloul, L. Cherbi, A. Hariz, and M. Tlidi, “Temporal localized structures in photonic crystal fiber resonators and their spontaneous symmetry breaking instability,” *Philos. Trans. R. Soc. Lond. A*, vol. 372, no. 2027, p. 20, 2014.

[82] P. Manneville, *Dissipative Structures and weak turbulence*. Academic Press, 1990.

[83] M. Tlidi, R. Lefever, and P. Mandel, "Pattern selection in optical bistability," *Quantum and Semiclassical Optics: Journal of the European Optical Society Part B*, vol. 8, no. 4, p. 931, 1996.

[84] M. Tlidi and L. Gelens, "High-order dispersion stabilizes dark dissipative solitons in all-fiber cavities," *Opt. Lett.*, vol. 35, pp. 306–308, Feb 2010.